Investigation of Electro-Nuclear Backgrounds for LOHENGRIN

Laney Scarlett Klipphahn

Masterarbeit in Physik
angefertigt im Physikalischen Institut

vorgelegt der
Mathematisch-Naturwissenschaftlichen Fakultät
der
Rheinischen Friedrich-Wilhelms-Universität
Bonn

Juni 2025

I hereby declare that this thesis was formulated by myself and that no sources or tools other than those cited were used.

Bonn, ...
Date Signature

1. Gutachter: Prof. Dr. Klaus Desch
2. Gutachter: Prof. Dr. Matthias Schott

Table of Contents

CHAPTER 1

Introduction

One of the most fundamental questions in physics is the question of what constitutes matter, or in other words:

What are we and the universe around us made of?

To our current knowledge the Standard Model (SM) of Elementary Particle Physics is the best description of our world at a sub-atomic scale. It embodies the current understanding of the elementary building blocks of matter and interactions between them. However, the universe is made up of only 5 % of visible matter as we know it [1]. Dark Matter (DM) and Dark Energy constitute the rest of the universe's mass and they are not included in the theoretical framework of the SM [2, 3]. The term *dark matter* was introduced due to the invisible characteristics of this new form of matter, whose presence is inferred mainly from cosmological observations such as gravitational lensing [4]. The search for DM has long been of interest to scientists around the world and for many years the focus of DM searches were heavy particles in the GeV to TeV mass range. Though previous and ongoing searches for heavy dark matter at experiments in this mass range have so far been unsuccessful in finding such proposed DM particles. A promising and not as well explored family of DM models contain dark matter particles with masses below ≈ 1 GeV. These models introduce a new so-called *dark sector* with its own gauge boson - the *dark photon*. This dark photon can couple to the SM via a *portal interaction*, making the search at experiments possible. A promising strategy is the production of dark photons at fixed target experiments in a process similar to SM bremsstrahlung.

The LOHENGRIN experiment, planned to take place at the ELSA accelerator in Bonn is designed to explore exactly this mass range - from MeV to GeV - for light dark matter candidates by indirect measurement of the dark photon [5]. The experiment obtains an electron beam at an energy of 3.2 GeV from the accelerator that can undergo dark bremsstrahlung in a target and thus possibly produce dark photons. In such interactions the dark photon carries away a large fraction of the incident electrons energy, causing a significant amount of missing momentum in the final state. The characteristic signal is determined by a single incident electron, a recoiling electron with less than 75 MeV and no other significant energy deposits in the final state. [5]

Hadronic final states comprise a particularly challenging background to the dark photon search at LOHENGRIN, as single nucleons or mesons can be ejected from the target at large angles, evading the detectors that are placed in forward direction and thus mimicking the missing momentum signal. Hence the understanding and suppression of such backgrounds are essential. The main production mechanism of hadronic final states are electro-nuclear interactions of beam electrons in the target. This leads to a

critical question: Are the current veto strategies sufficient to reject hadronic backgrounds produced via electro-nuclear interactions in the target?

By studying electro-nuclear interactions and investigating the angular distributions of secondary particles, this thesis aims to answer this question regarding the existing veto strategy.

The structure of the thesis is as follows: Chapter 2 gives an introduction to the Standard Model and extensions beyond it, including theoretical motivations for dark photons and light dark matter. The LOHENGRIN experiment will be introduced in chapter 3, explaining the detector setup, the photon production at the experiment as well as possible backgrounds and the physics reach. In chapter 4 electro-nuclear interactions using the GEANT4 simulation framework will be investigated to study secondary particles from such processes. During this work it could be highlighted that GEANT4 is not applicable in the signal region of the LOHENGRIN experiment, as the simulation of electro-nuclear interactions does not reliably cover energy transfers of more than $\approx 94\,\%$ of the incident electron onto the target nucleus. This is the reason for the exploration of an alternative event generator in chapter 5, which is the simulation framework FLUKA. In this chapter secondary particles from electro-nuclear interactions are analysed to further strengthen the understanding of these processes. Additionally the impact of the target material on the electro-nuclear interactions is investigated, photo-nuclear interactions are studied and compared to the electro-nuclear process and an event selection is applied to the MC truth data to get an estimate of hadronic final states in the signal region. The last chapter of this thesis - chapter 6 - investigates the detector response and sensitivity to electro-nuclear interactions simulated in FLUKA. A stand-alone implementation of the detector geometry is implemented in GEANT4, to investigate the veto efficiency with the current detector setup of the LOHENGRIN experiment.

CHAPTER 2

The Standard Model and Beyond

As mentioned above, the Standard Model (SM) of Elementary Particle Physics is the current understanding and description of the fundamental building blocks of matter and interactions between them. This chapter begins with an introduction to the Standard Model of Elementary Particle Physics and its key components and principles in section 2.1. Despite its success, the SM also has limitations and not all observed phenomena today can be explained by it. The existing bounds of the current state of the SM will be discussed in section 2.2. One of the unexplained phenomena not included in the SM is Dark Matter (DM), which is an invisible form of matter, making up a large part of the universe's mass. Early efforts to explain DM with a minimal extension of the SM will be discussed in section 2.3. A more recent development in the search for dark matter is the addition of a so-called dark sector to the SM with its own gauge interaction. This dark sector allows for the search of light dark matter (LDM) and is made up of a mediator and a dark matter particle that can couple to SM particles under specific conditions. In section 2.4 the dark sector scenario will be introduced and a production process of a mediator particle - in particular the dark photon- will be discussed in section 2.5.

2.1 The Standard Model of Particle Physics

The Standard Model (SM) describes three of the four fundamental forces, namely the weak, strong and electromagnetic forces [6–8]. Even though gravity seems to dominate the universe at large scales, it is negligible at the sub-atomic scales of particle physics [9]. In the SM the fundamental forces are mediated by particles, which emerge from the fundamental requirement of local gauge invariance. The force carriers in the SM are spin-1 gauge bosons that mediate between the fermionic matter particles charged under the respective interaction. The force carriers in the SM are the massless photon, which mediates the electromagnetic force, the massive Z and $W^{\pm}$ bosons mediating the weak force, and eight gluons mediating the strong force. [10]

Other than the spin-1 bosons, the fermionic matter particles have spin-$\frac{1}{2}$. The fermions are comprised of six flavours of quarks, six flavours of leptons and their respective anti-particles. Quarks are categorized into three generations (families) based on their mass. The first generation of quarks is stable and is made up of the lightest quarks - the up and down quark. The second and third generations contain the charm, strange, top and bottom quarks, which are heavier and unstable. Quarks carry one of three different colour charges: red, blue or green. However, only particles that carry no net colour charge are observed

as free particles in nature - this is called confinement and leads to the phenomenon of hadronisation. If an individual quark is created in any interaction, it almost instantly hadronizes into a bound state consisting of two or three quarks. These states are so called hadrons. Two quarks form a meson and three quarks combine to create a baryon. [10]

Similarly, leptons are grouped into three generations, with the first generation consisting of the electron and electron neutrino. The second and third generations include the muon, muon neutrino, tau and tau neutrino. The charged leptons of generations two and three are unstable and decay into leptons from the lower generations. The electron, muon and tau are charged under electromagnetism and weak interactions, while the neutrinos are uncharged under electromagnetism and charged under the weak interaction. From electroweak unification, we learn that charged leptons exist in both left- and right-handed states, while neutrinos are only left-handed. Since neutrinos are massless in the SM, only left-handed neutrinos can exist, which is due to their weak hypercharge Y and how they couple to the weak interaction. Left- and right-handedness refers to the particle's helicity, whether its spin is aligned (right-handed) or anti-aligned (left-handed) with its direction of motion. This distinction is fundamental in the SM, where only left-handed particles participate in weak interactions. [10]

The last particle of the SM that was discovered is the Higgs boson. It is the only scalar (spin = 0) particle in the SM and couples to all fermions by means of a Yukawa coupling that is proportional to the mass of the fermion. Similarly, it couples to the massive gauge bosons in the SM [11]. A detailed overview of the particles of the SM is given in figure 2.1.

The theoretical framework to describe the SM is the gauge invariant quantum field theory (QFT), based on the symmetry group $SU(3) \times SU(2) \times U(1)$, where $SU(3)$ corresponds to the colour group for the strong interaction and $SU(2) \times U(1)$ corresponds to the electroweak interaction, spontaneously broken by the Higgs mechanism. Particles are thus described by excited states of their underlying quantum fields. To describe systems and how they behave with time, the so-called Lagrangian $\mathcal{L}$ is used in theoretical physics. It is given by the difference between kinetic and potential energy in a certain system [13]. For example the classical harmonic oscillator for a mass m sliding across a surface connected to a spring with spring constant k has the following Lagrangian [14]:

$$\mathcal{L} = \frac{1}{2}m\dot{x}^2 - \frac{1}{2}kx^2 \quad , \tag{2.1}$$

where the first term corresponds to the kinetic energy and the second term is the potential energy of the spring. In particle physics - so in quantum field theory - the kinetic and potential energies are replaced by kinetic terms and their interactions. While kinetic terms inform about the free behaviour of the system, the interaction terms give information on the interactions of the particles. Since in quantum field theory fields are the fundamental quantities, the Lagrange function used in classical physics is replaced by a Lagrange density, which describes the dynamics of these fields at every point in space and time. [13] The SM Lagrangian is comprised of several partially independent terms: the kinetic terms for all particles and the interaction terms, one for each fundamental interaction, as well as the Higgs potential term and the Yukawa interactions. For particular physics processes, some of these terms can be neglected and it is thus sufficient for this thesis to study the electromagnetic term. [13]

The quantum field theory of electrodynamics is so-called quantum electrodynamics (QED) and is part of the $U(1)$ gauge group [10]. The QED Lagrangian needs to be invariant under local gauge

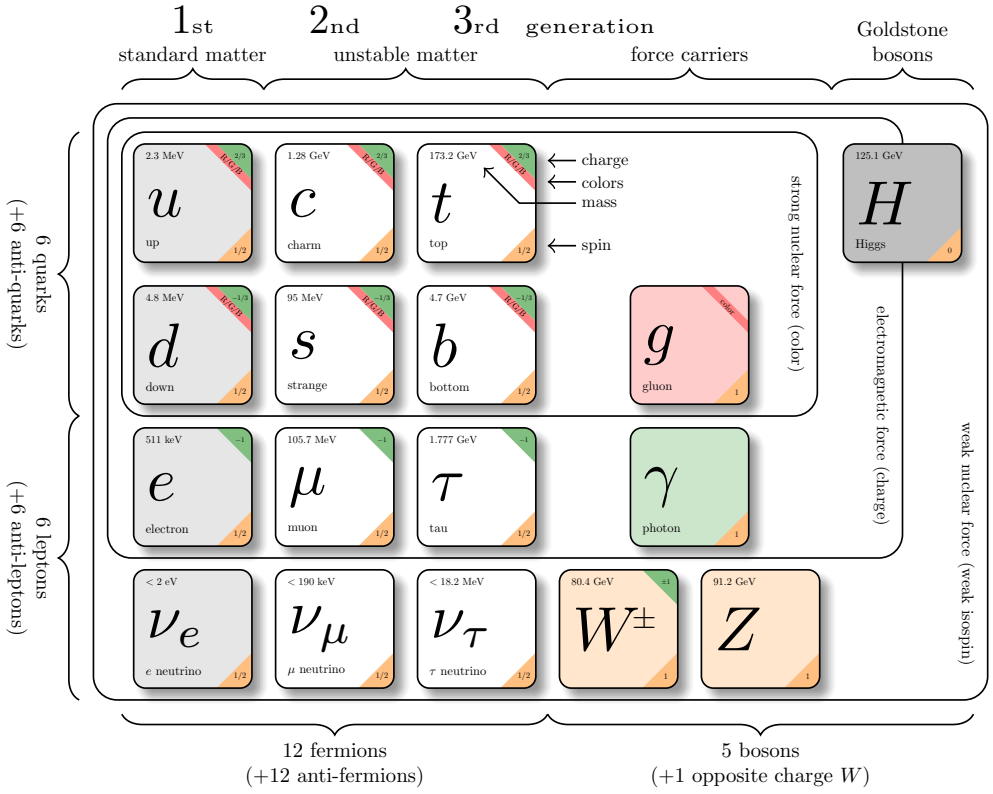

Figure 2.1: Overview of the known particles of the Standard Model of Particle Physics, adapted from [12].

transformations and is given by

$$\mathcal{L}_{\text{QED}} = -\frac{1}{4}F_{\mu\nu}F^{\mu\nu} + i\bar{\psi}\not{D}\psi - m\bar{\psi}\psi \quad , \tag{2.2}$$

where $F_{\mu\nu} = \partial_\mu A_\nu - \partial_\nu A_\mu$ is the Maxwell tensor with vector A_μ. To obtain the required local gauge invariance, the derivative ∂_μ is replaced by the covariant derivative $D_\mu = \partial_\mu + ieA_\mu$ and written in slash notation $\not{D}_\mu = \gamma^\mu(\partial_\mu + ieA_\mu)$. The field A_μ arises from the need of local gauge invariance, and must transform as $A_\mu \rightarrow A'_\mu = A_\mu - \partial_\mu\chi$. This field corresponds to the photon and thus the QED Lagrangian describes the electromagnetic interactions between charged fermions and the massless photon. [10, 13]

2.2 Bounds of the SM

Up to now the SM has successfully predicted and explained the existence and interactions of particles. Two famous examples are the discovery of the top quark in 1995 and the Higgs boson experimentally found in 2012 by the ATLAS [15] and CMS [16] experiments at the LHC. Though the SM was able to predict the existence of particles that would later be experimentally verified, the SM is no "*Theory*

of Everything" and cannot explain all phenomena observed in physics today. One obvious example is the missing explanation and inclusion of gravity in the SM, which can be seen by the incompatibility of General Relativity and the Standard Model. It is not possible to describe the two with the same theoretical framework, namely quantum field theory [17, 18]. There are additional observations that cannot be explained by the current state of the SM, like neutrino oscillations observed by, e.g. solar neutrino experiments like the Super-Kamiokande [19]. They prove that at least two of the three known neutrinos must have a non-zero mass, which is in contradiction to the SM massless neutrinos.

Another part of physics not explained by the SM is dark matter (DM) and dark energy. For this thesis especially the former is of interest. The universe as we know it today only consists partly of luminous - so electromagnetically interacting - matter [2, 20]. According to the cosmological SM, the rest is made up of dark matter and dark energy [2, 3]. While black holes and other MACHOs (massive compact halo objects) are not explained by the Standard Model, they can be understood within the framework of general relativity and stellar astrophysics, without the need of physics beyond the SM [21, 22]. There are however observations from cosmology that are not understood yet. One such example is the formation and evolution of galaxies, especially disk galaxies. Disk galaxies consist - as the name suggests - of a thin rotating disk with spiral arms. The stars and gas within the galaxy move on roughly circular orbits in the disk plane and thus the kinematics of the disk are determined by its rotation curve $V_{\text{rot}}(R)$. The rotation curve expresses the rotation velocity as a function of galactocentric[1] distance. From the understanding of gravity on a macroscopic scale, the expected rotational velocity of stars should decrease for larger radii. Such rotation curves can be measured and for massive galaxies these typically rise rapidly at small radii and are almost constant over the rest of the disk. Though variations between different systems are to be expected. In figure 2.2 the measurement of the rotation curve of two galaxies can be viewed. The left figure shows the typical behaviour for massive galaxies, while on the right the slower rise behaviour for low-surface brightness galaxies is given. Most interesting in this observation is the constancy of the rotation velocity at large radii, as it contradicts the expectation. Thus this is evidence that spiral galaxies must have massive halos of unseen - dark - matter that interacts gravitationally. [23]

Other observations in cosmology that hint at the existence of dark matter are the effects of gravitational lensing [24, 25] and the Cosmic Microwave Background (CMB), such as data from the Planck satellite [26, 27] or COBE [28] and WMAP data [29]. Gravitational lensing is a geometrical effect present in all instances of observing light from a source that travels through some form of inhomogeneities in space. The most commonly known form of gravitational lensing is weak gravitational lensing, which can be observed in any line of sight in the universe, as photons travelling along that line are affected by matter inhomogeneities. The angular size and apparent brightness of an object are affected by weak gravitational lensing and thus objects appear with different shape and brightness for two separate recordings. [4] This gravitational lensing effect is much larger than could be accounted for by visible matter alone.

The Cosmic Microwave Background (CMB) is another crucial observational tool in cosmology to study the universe. From its measurements, the existence of dark energy and dark matter can be deduced and key features like the non-baryonic structure of dark matter were found by acoustic peaks in the CMB power spectrum. [26, 29]

[1] galactocentric: meaning relative to the centre of the galaxy

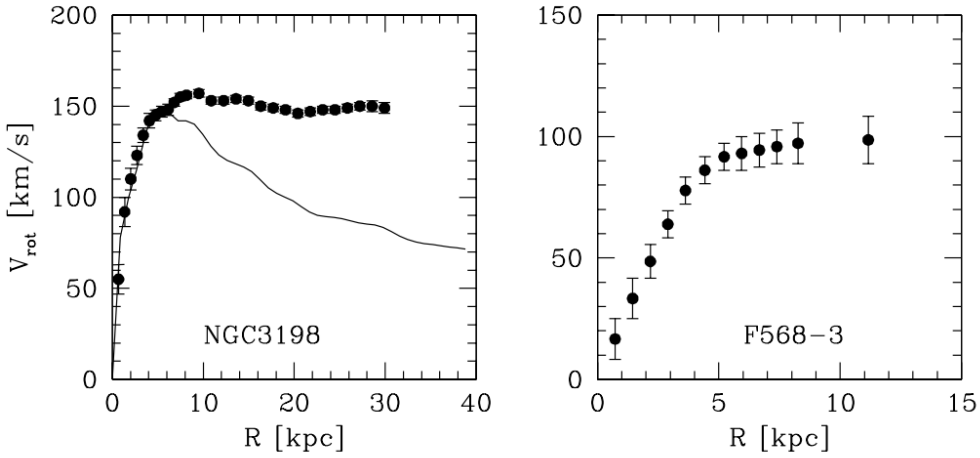

Figure 2.2: Rotation curves of the Sc galaxy NGC 3198 (left) and the F568-3 galaxy (right). Taken from [23].

2.3 Early DM searches

The search for dark matter in the universe has been an ongoing field of research in physics for several decades and many theoretical models and experimental efforts have been proposed and pursued. Of particular interest are models, which require only a minimal extension of the SM, consisting of a single particle that interacts weakly with the SM.

One of the earliest proposals was introduced by Lee and Weinberg, suggesting heavy neutrinos to account for the dark matter abundance [30]. At the time it was known that neutrinos could not exceed masses of 40 eV, due to constraints on the present number density of neutrinos. Heavier neutrino masses far above 1 MeV were not seriously considered as viable dark matter candidates.

By introducing a hypothetical heavy, stable, neutral lepton L^0, they showed that such a particle could be consistent with cosmological observations, if it annihilated efficiently with its antiparticle $\bar{L}^0$ in the early universe. The possible annihilation channels include:

$$L^0\bar{L}^0 \rightarrow \nu\bar{\nu}, e^-e^+, \mu^-\mu^+, \pi^-\pi^+, \text{etc.} \tag{2.3}$$

These heavy leptons go out of chemical equilibrium[2] at a "freeze-out" temperature T_f, much larger than 1 MeV, caused by their annihilation rate being far less than the cosmic expansion rate at temperatures below 10^{10} K. From this analysis a new lower bound - the so-called Lee-Weinberg bound - on the L^0 mass was derived:

$$m_L(N_A/\sqrt{N_F})^{0.51} \geq 5.2\,\text{GeV} \quad , \tag{2.4}$$

where N_A corresponds to a dimensionless fudge factor depending on the number of annihilation channels open and on the details of the weak $L^0\bar{L}^0$ annihilation interaction and N_F is the effective number of degrees of freedom. N_F effectively counts the available annihilation channels, so the number of lighter quarks and leptons than the heavy lepton and that can be produced in weak interactions. For $N_A = 14$ and $N_F = 4.5$ the lower bound of the lepton mass is given by $m_L \geq 2\,\text{GeV}$. Though if taking an uncertainty

[2] Meaning the number density exceeds its equilibrium value.

factor of 4 on the annihilation rate, the lower bound of the mass m_L may range from 1 to 4 GeV. [30] The idea of weakly interacting heavy neutrinos established a new path for the explanation of dark matter, as particles with weak-scale masses and weak interactions, naturally yield the correct relic abundance. [31]

Based on this approach the so-called WIMPs (Weakly Interacting Massive Particles) are introduced a few years later by Steigman and Turner [32]. In the previous years various types of experiments pursued the detection of WIMPs, some of which are direct detection experiments like the XENONNT experiment [33], the LUX-ZEPELIN experiment or the PandaX experiment [34]. Collider experiments like the CMS [35] probe for WIMPs and also possible dark sectors at their facilities and indirect detection is probed with experiments like the Fermi Gamma-ray Space Telescope [36] or the IceCube neutrino observatory [37]. Up to now, no search at experiments has yielded any promising results on the existence of WIMPs. Therefore the search for light dark matter (LDM) has gained momentum in the recent years, which will be discussed in the next section.

2.4 Dark Sector Scenario

As explained in the previous section, it was obvious to search for dark matter with minimal extensions of the SM and thus look for single possible dark matter particles such as the WIMPs. Though since no positive results have been found by many experiments regarding the existence of these heavy dark matter particles, other extensions featuring light dark matter particles have been explored. In addition to the DM particle itself, these models require the introduction of a new gauge interaction between the dark matter particles, in order to explain the apparent relic density throughout the thermal freezeout mechanism. This new gauge interaction must couples to the SM sector to explain the relic abundance today, which is realised via kinetic mixing. The dark matter particle χ and the gauge boson associated with the new gauge interaction form a dark sector with minimal content.

There are several possibilities for a dark sector, depending on the mediator particle that couples to the SM via a portal. The nature of the portal interaction between the SM and the dark sector is dictated by the mediator's spin and parity. The mediator can be a scalar, a pseudoscalar, a fermion or a vector. Though the gauge and Lorentz symmetries of the SM impose constraints on how the mediator interacts with the SM. The simplest variant of the new gauge interaction is a $U(1)_D$ symmetry with a vector mediator A', which is often called dark photon. Considering first a minimal kinetically mixed dark photon with vector field $A_{D\mu}$, the SM Lagrangian can be extended by its own Lagrangian of the form [5, 38]:

$$\mathcal{L}_{A_D} = -\frac{1}{4}F_{D\mu\nu}F_D^{\mu\nu} - \frac{\epsilon}{2\cos\theta_W}F_D^{\mu\nu}B_{\mu\nu} + \frac{1}{2}m_{A_D}^2 A_D^\mu A_{D\mu} - g_D A_{D\mu}J_D^\mu \quad . \tag{2.5}$$

Here $F_{D\mu\nu} = \partial_\mu A_{D\nu} - \partial_\nu A_{D\mu}$ represents the dark photon field strength, $B_{\mu\nu} = \partial_\mu B_\nu - \partial_\nu B_\mu$ denotes the SM hypercharge field strength, J_D^μ is the current, m_{A_D} is the acquired dark photon mass, ϵ is the kinetic mixing parameter, θ_W corresponds to the weak mixing angle and g_D is the dark sector coupling. The dark photon therefore couples to the SM through a portal, which is realized by the kinetic mixing operator $\propto F_D^{\mu\nu}B_{\mu\nu}$. SM fermions can couple to the dark photon mass eigenstate A'_μ with mass $m_{A'} \approx m_{A_D}$. This is one of the simplest dark sector scenarios itself, but could also be a small part in a more complex dark sector.

Considering a mass range of MeV-GeV for the dark photon, the dominant effect of the kinetic mixing after electroweak symmetry breaking, results in an analogous mixing term $\frac{1}{2}\epsilon F_D^{\mu\nu}F_{\mu\nu}$ with the SM electromagnetic field strength $F^{\mu\nu}$. In this framework the dark photon couples with strength $e\epsilon$ to the

electromagnetic current, assuming a basis with diagonal and canonically normalized kinetic terms. [5, 38]

To incorporate DM in the model, the minimal dark photon scenario can be extended. This DM candidate can be a fermion χ or a scalar boson ϕ coupling to the dark photon through dark sector gauge interactions, as described by the following Lagrangian:

$$\mathcal{L}_{DM(f)} = \bar{\chi}(i\not{D} - m_\chi)\chi \quad , \quad \mathcal{L}_{DM(s)} = (D^\mu\phi)^*(D_\mu\phi) - m_\phi^2|\phi|^2 \quad , \tag{2.6}$$

where $D_\mu = (\partial_\mu - ig_D A_\mu)$ and g_D is the dark sector coupling. Since the dark photon mediates interactions between the DM and the SM electromagnetic current, detection of DM in laboratory experiments could be possible. [38]

There are several possibilities of dark matter particles such as scalar elastic, scalar inelastic, Majorana or pseudo Dirac DM [39]. The scalar elastic scenario assumes χ to be a complex scalar particle with $U(1)_D$ preserving mass terms and the current

$$J_D^\mu = i(\chi^*\partial^\mu\chi - \chi\partial^\mu\chi^*) \quad . \tag{2.7}$$

In the inelastic scalar scenario the χ is also a complex scalar particle with $U(1)_D$, but symmetry breaking mass terms. The corresponding current

$$J_D^\mu = i(\chi_1^*\partial^\mu\chi_2 - \chi_2^*\partial^\mu\chi_1) \quad , \tag{2.8}$$

is only possible if the χ couples to the dark photon inelastically and transitions into a heavier state. However direct detection even for small mass differences of $\chi_{1,2}$ is not possible due to the suppression of direct detection signals. The χ can also be a Majorana fermion, coupling through an axial-vector current

$$J_D^\mu = \frac{1}{2}\bar{\chi}\gamma^\mu\gamma^5\chi \quad . \tag{2.9}$$

The pseudo Dirac scenario assumes the DM χ to be a pseudo Dirac fermion. Dependent on the χ mass term and whether it is $U(1)_D$ preserving, it is already constrained by the cosmic microwave background (CMB) data. [40] If there is a particle-antiparticle asymmetry this constraint might be lifted. However if the mass terms break the $U(1)_D$ symmetry, then the χ is split into two Majorana fermions. They couple off-diagonally to the A' through the current

$$J_D^\mu = i\bar{\chi}_1\gamma^\mu\chi_2 \quad . \tag{2.10}$$

An additional axial current couples to the A'. [39]

The thermal relic targets for each DM candidate can be viewed in figure 2.3 together with some experimental projections. The missing momentum approach drawn with the red, dashed line, shows the possibility to probe this sector via missing momentum experiments. In this context the thermal relic target corresponds to a specific target in the parameter space of the dark sector scenario, namely the thermal DM freeze-out. The thermal DM freeze-out predicts a thermally-averaged DM cross section of $\approx 3 \times 10^{-26}\,\mathrm{cm}^3\,\mathrm{s}^{-1}$ with small dependence on the DM mass and is one explanation of the abundance of DM today. [38]

Some experiments that aim to probe the light dark matter sector are the LDMX [39], DARKSHINE [41], SHIP [42], NA64 [43] experiments and the LOHENGRIN experiment introduced in the next chapter 3.

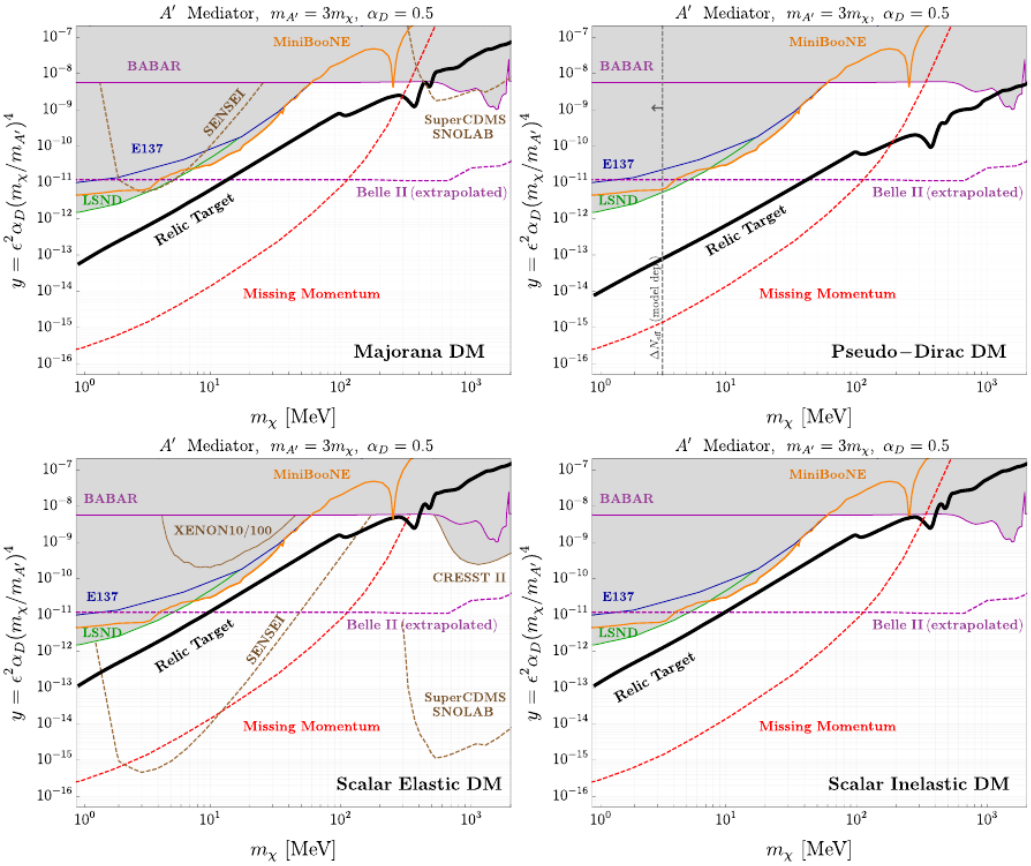

Figure 2.3: Thermal relic targets for DM candidates coupling to the dark photon A' for the parameter space of LDM in the y vs. m_χ plane, together with future experimental projections. Taken from [39].

Depending on the masses of the dark photon A' and dark matter candidate χ there are two possible annihilation scenarios: secluded and direct annihilation or more directly: visible and invisible dark photons. From the Feynman diagram of the direct annihilation, the direct detection of DM can be deduced and motivated.

Secluded annihilation

If the mass of the dark photon is less than the mass of the dark matter candidate: $m_{A'} < m_\chi$, then the DM annihilates dominantly into pairs of A'. The corresponding Feynman diagram can be viewed on the left in figure 2.4. The annihilation rate is independent of the SM-A' coupling ϵ. If considering only a simple model then this scenario is constrained by CMB data, ruling out DM masses below $O(\text{GeV})$ for simple secluded annihilation. More complex models are viable, though they do not provide a sharp parameter space target. [38]

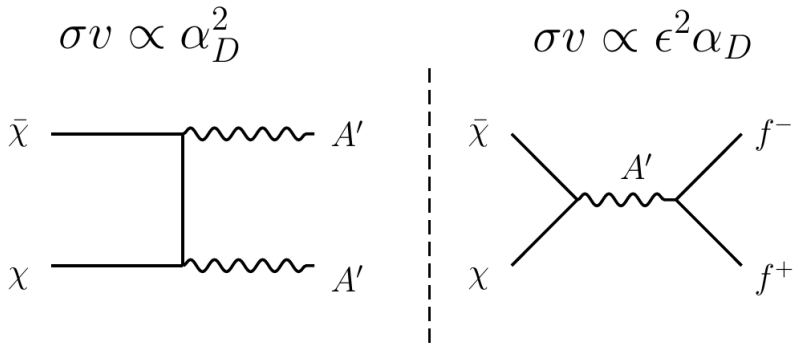

Figure 2.4: Feynman diagrams for secluded annihilation (left) and direct annihilation (right) for LDM. Taken from [39].

Direct annihilation

In direct annihilation the mass of the dark photon must succeed that of the dark matter candidate: $m_{A'} > 2m_{\chi}$. Then the DM annihilates via $\chi\bar{\chi} \rightarrow A' \rightarrow ff$ to SM fermions through a virtual mediator, the dark photon. Here the CMB data does not provide constraints on the model. A minimum DM production rate at accelerators is implied from the observed abundance of DM, though the detailed phenomenology depends on the ratio of the masses of the mediator and dark matter particles. The Feynman diagram of the direct annihilation can be seen on the right in figure 2.4. If the Feynman diagram is rotated, scattering off SM fermions is depicted and can be probed by accelerator experiments. [38]

2.5 Dark Bremsstrahlung

One of the main production channels of the dark photon is dark bremsstrahlung. It works analogously to QED bremsstrahlung, where an incoming electron e^- interacts with a hadronic system $\mathcal{H}$ and triggers the following process

$$e^- + \mathcal{H} \rightarrow e^- + \mathcal{H} + A' \quad , \tag{2.11}$$

instead of a SM photon a dark photon emerges from the reaction. In figure 2.5 the lowest-order amplitude of dark photon production is given. The Feynman diagram on the left shows an electron undergoing dark bremsstrahlung in the field of a nucleus with the exchange of a virtual photon. This process can be probed by fixed-target experiments, where the dark photon A' is produced in forward direction. The dark photon will carry most of the beam energy after the reaction and the electron obtains a large angle. Depending on the mass of possible DM candidates and the dark photon itself, the dark photon can decay into a pair of DM and anti-DM particles. [38] One experiment to detect dark bremsstrahlung is the LOHENGRIN experiment planned at the ELSA accelerator at the University of Bonn, which will be discussed in more detail in chapter 3.

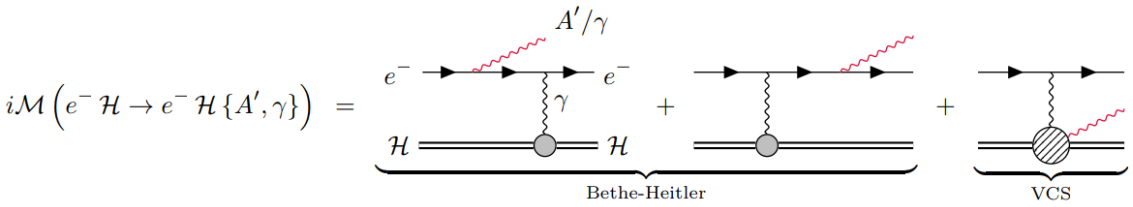

Figure 2.5: Feynman diagrams contributing to the lowest-order amplitude of (dark) photon production in collision of an electron with a hadronic system. The grey circle represents form factor evaluations and the dashed circle represents the VCS amplitude. Taken from [5].

CHAPTER 3

The LOHENGRIN Experiment

The LOHENGRIN[1] experiment is a search for light dark matter experiment planned to take place at the University of Bonn. It is a fixed target experiment supplied with a 3.2 GeV electron beam from the ELSA accelerator and aims to detect dark photons via dark bremsstrahlung of the beam electron in a target. In section 3.1 an overview of the accelerator will be provided, followed by an introduction of the dark photon production at LOHENGRIN in section 3.2. Background processes relevant to the experiment are covered in section 3.3 and the detector components are described in section 3.4. The signal region of the experiment is detailed in section 3.5, while section 3.6 explains the modelling of electro-nuclear backgrounds. The chapter concludes with an outline of the physics reach of the LOHENGRIN experiment in section 3.7.

3.1 The ELSA accelerator

The Electron Stretcher Accelerator ELSA is located at the physics institute at the University of Bonn. It is an electron accelerator planned to provide the beam for the LOHENGRIN experiment, as mentioned above. The accelerator is able to deliver a high-rate electron beam with variable energy up to 3.5 GeV. The electrons are accelerated in three stages to reach the 3.2 GeV necessary for LOHENGRIN. First 50 keV electrons from a source are accelerated in a linear accelerator to 26 MeV and then injected into the booster synchrotron. In the booster synchrotron the electrons are accelerated further to an energy of 1.6 GeV. To obtain even more energy, the electrons are then transferred to the stretcher ring. There are three different operation modes of the stretcher ring. For a beam energy of 3.2 GeV the booster mode is used. In figure 3.1 the facility map of the ELSA accelerator can be viewed, with its linear accelerator, booster synchrotron, stretcher ring and its hadron physics experiments BGOOD and CB-ELSA. [44, 45]

From each filled bucket, electrons can be extracted with an expectation value of one electron per revolution or less, which provides the experiment with a clean initial state. This is an advantage of the experiment, as the initial state can be precisely determined with basic tagging detectors. The planned extraction rate for LOHENGRIN is a bunch spacing of 2 ns, extracting 0.2 electrons from each bunch per revolution. Thus it is also possible to have events with no electron or with more than one electron on target. With this configuration an extraction rate of 100 MHz can be reached and the probability to extract more than one electron in a single event is reduced to less than 1.8 %. [5]

[1] The meaning of which, no one may ever know.

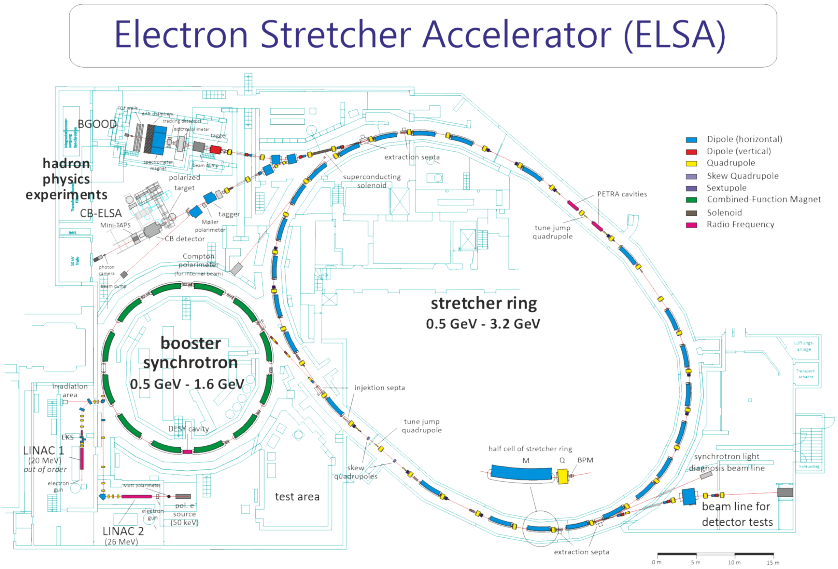

Figure 3.1: Schematic facility setup of the Electron Stretcher Accelerator (ELSA) at the University of Bonn. Taken from [46].

3.2 Dark photon production

As mentioned in section 2.5, dark photons can be produced at accelerator experiments via dark bremsstrahlung. This is also the underlying process of the dark photon production at the LOHENGRIN experiment. The reaction given in equation 2.11 is made possible through the interaction term

$$\mathcal{L} \supset \sum_f i Q_f \epsilon \bar{F} \gamma^\mu f A'_\mu \quad , \tag{3.1}$$

of the Lagrangian. Where f is the fermion with electric charge Q_f and ϵ is the reduced kinetic mixing parameter. From this model the effective portal coupling $g^f_{\mathrm{SM}} = Q_f \epsilon$ arises. The value of ϵ can range between several orders of magnitude $\epsilon \sim 10^{-1} - 10^{-12}$ and it is thus sufficient to choose it as a free parameter. [5]

The lowest order Feynman diagram is given in figure 2.5, which has the most dominant contributions from Bethe-Heitler (BH) scattering between the incoming electron and the nucleus. The incoming electron exchanges a photon with the nucleus during this process. The nucleus can be treated as a scalar, since contributions arising from its magnetic moment are suppressed by its inverse mass. Additionally the target material at LOHENGRIN is tungsten, which is naturally mostly made up of three scalar isotopes with $J^P = 0^+ ({}^{182}_{74}\mathrm{W}(27\,\%), {}^{184}_{74}\mathrm{W}(31\,\%), {}^{186}_{74}\mathrm{W}(28\,\%))$. Only a small fraction of 14 % of a non-scalar isotope $J^P = \frac{1}{2}^- ({}^{183}_{74}\mathrm{W})$ can be found in the naturally occurring tungsten [5]. This fermionic component of the material contributes to the cross section with its inverse mass squared and thus for simplicity the target can be assumed to be scalar for modelling these backgrounds. [5] In figure 2.5 additional contributions from virtual Compton scattering (VCS) to the dark bremsstrahlung process are drawn. For VCS the radiation is emitted from the hadronic system rather than the electron. Since the dark photon fundamentally also couples to quarks, this reaction is also possible. Other contributions to be considered

are impacts from the hadronic system, for example the nuclear charge distribution of the target nucleus or contributions from the nucleons of the target nucleus, which contribute with their charge and magnetic moments. From a simulation done in a dedicated Monte Carlo framework called `Lohengrin++`, no significant contribution to the missing momentum search from VCS or from individual nucleons could be found. [5]

Since the Lohengrin experiment aims to detect dark photons, that do not interact with any kind of detector material, it relies on the precise measurement of the electron after the dark bremsstrahlung process. In such interactions the electron will receive a sizeable transverse kick, dependent on the mass of the dark photon. The signal signature of the Lohengrin experiment is therefore the recoiling electron with its transverse kick and no other detectable signal, causing the missing-momentum. In figure 3.2 the double differential cross section with respect to the energy fraction ξ and the solid angle Ω of the recoiling electron is given together with its angle θ_e. Four different benchmark masses for the dark photon are presented: 1 MeV, 10 MeV, 100 MeV and 1 000 MeV. For a fixed target experiment this mass range follows from the available energy in the center of mass frame, given by:

$$s = (P_t + P_{e^-})^2 \quad , \tag{3.2}$$

where $P_t = (m_t, \vec{0})$ is the 4-momentum of the target nucleus and $P_{e^-} = (E_{e^-}, \vec{p})$ is 4-momentum of the incoming electron. Then follows

$$s = m_t^2 + 2E_{e^-}m_t + E_e^2 - \vec{p}^2 \quad \rightarrow \quad \sqrt{s} \approx \sqrt{m_t^2 + 2E_{e^-}m_t + m_e^2} \quad . \tag{3.3}$$

Using a tungsten nucleus with mass 183.84 amu [47], an electron mass of 0.511 MeV [48] and an energy of 3 200 MeV, the center of mass energy is approximately

$$\sqrt{s} \approx 175.32\,\text{GeV} \quad . \tag{3.4}$$

Subtracting the tungsten rest mass, the maximum available energy for producing new particles - such as the dark photon - is roughly 3.17 GeV. This value presents an upper limit, as the dark photon will obtain momentum from the interaction and the recoiling electron also carries away part of this energy. Additionally the production cross section is decreasing for increasing masses due to the smaller available phase space. Therefore the mass range of 1 to 1 000 MeV for the dark photon is reasonable.

One can see in figure 3.2, that for increasing dark photon masses the electron kinematics shift towards lower energies and wider angles. The wider angles of the recoiling electron prove the transverse kick obtained in the interaction. There is an upper and lower bound for kinematically allowed final state electrons. The phase space window is enclosed by a low-energy boundary of $\xi \geq m_e/E$ and a high-energy boundary dependent on the dark photon mass. The number of signal events produced by forward electrons possibly observed at Lohengrin depend on the target thickness, which is assumed to be $0.1X_0 \approx 0.35$ mm, and the dark photon mass. In figure 3.3 the number of signal events in dependence of the dark photon mass for different amounts of electrons on target is presented. For dark photon masses between 10 to 100 MeV, between 1 and 100 events are expected for $4 \cdot 10^{14}$ electrons on target (e.o.t.), which is the order of magnitude of signal events assumed for the rest of this thesis. [5]

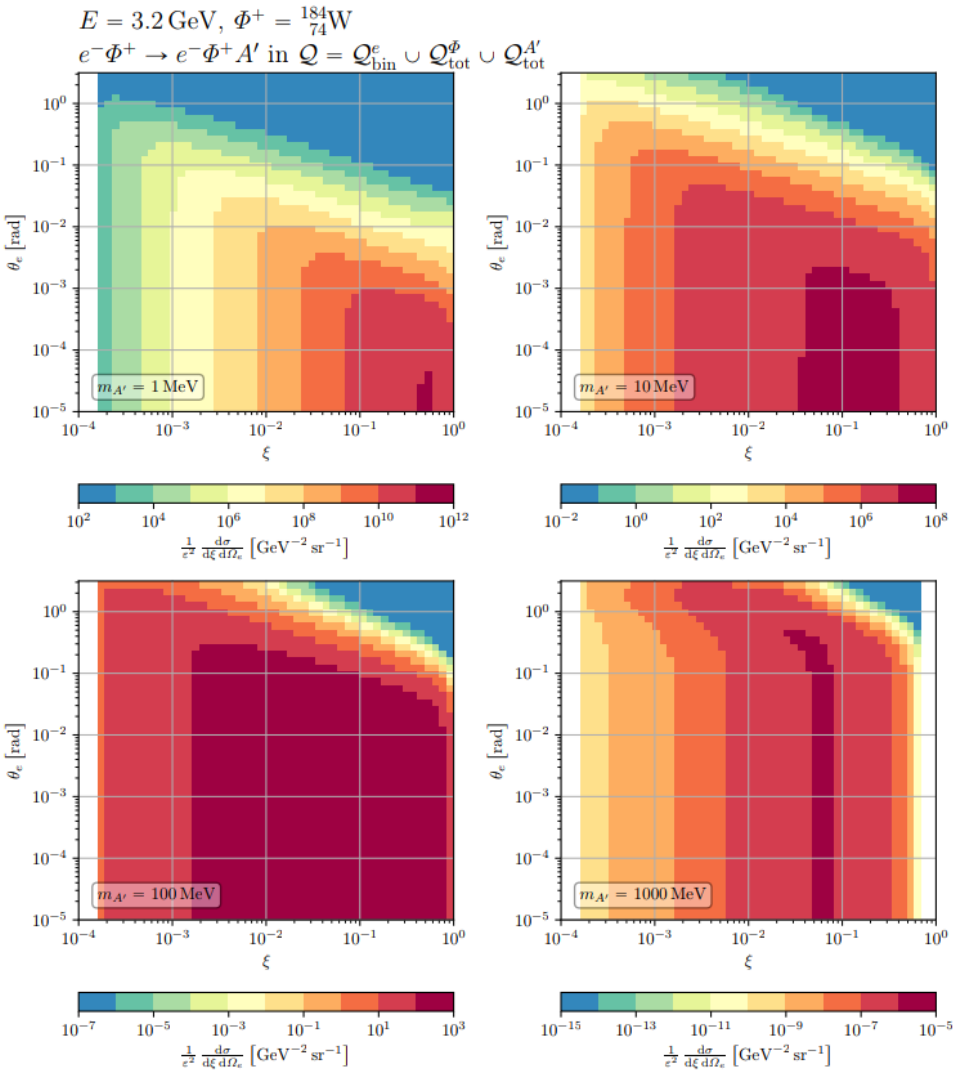

Figure 3.2: Double differential cross section of the dark photon production in dependence of the energy fraction ξ and solid angle Ω of the recoiling electron against its angle θ_e for four different benchmark masses and normalized by ϵ^2. Taken from [5].

3.3 Background Processes

To be able to find evidence for the existence of dark photons, the necessary detector set up has to be designed. It is obvious from the previous sections that the dark photon is only indirectly measured via missing momentum. All SM interactions with a signal-like signature, imitate the kinematics of a dark photon signal event and it is therefore of utmost importance to effectively reject backgrounds. A short overview of the main background contributions at the LOHENGRIN experiment will be given in the following.

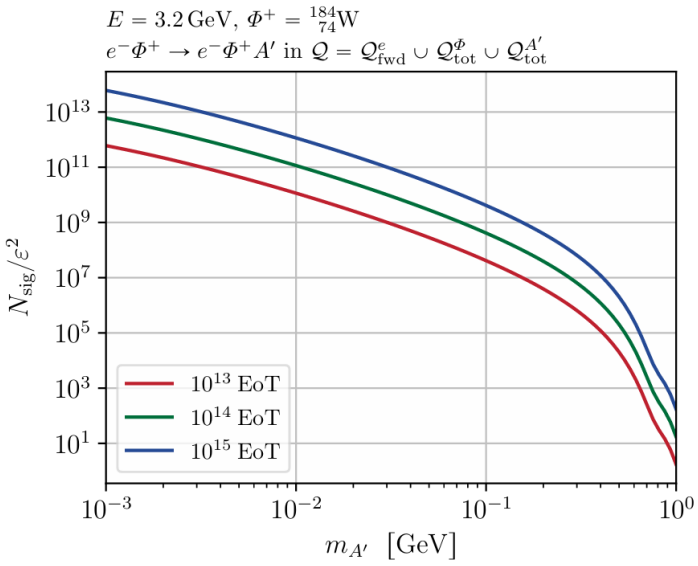

Figure 3.3: Number of signal events in dependence of the dark photon mass for different numbers of electrons on target for recoiling electrons in forward direction. The number of events is normalised by the suppressing parameter ϵ^2. Taken from [5].

3.3.1 Elastic QED Backgrounds

The lowest order elastic QED background process at $O(\alpha^2)$ is the process

$$e^- + \mathcal{H} \to e^- + \mathcal{H} \quad ,$$

where $\mathcal{H}$ denotes the nucleus of the target material. In this process however the electron does not transfer much of its energy onto the nucleus and is therefore not relevant for the missing momentum search at hand. [5] The dominant QED background source is SM bremsstrahlung with the radiation of a high-energy photon from the target that goes undetected:

$$e^- + \mathcal{H} \to e^- + \gamma + \mathcal{H} \quad .$$

Photons from SM Bremsstrahlung are emitted in forward direction in most cases and can be vetoed by a forward electromagnetic calorimeter (ECal), see section 3.4. Since the angular coverage of the ECal is limited, there are cases where the photon misses the calorimeter. These events cannot be vetoed and create an irreducible background. In figure 3.4 the cross section of SM Bremsstrahlung in dependence of the maximum veto-able photon angle is given. It is clearly visible that the cross section peaks for forward photons and decreases with increasing angle. The design of the ECal therefore has a large impact on the sensitivity of the experiment. [5]

Another component of the QED backgrounds is virtual Compton scattering (VCS), which has a more isotropic emission of photons and could lead to irreducible background. From calculations this is not expected, but needs to be measured properly in the early stages of the experiment. [5]

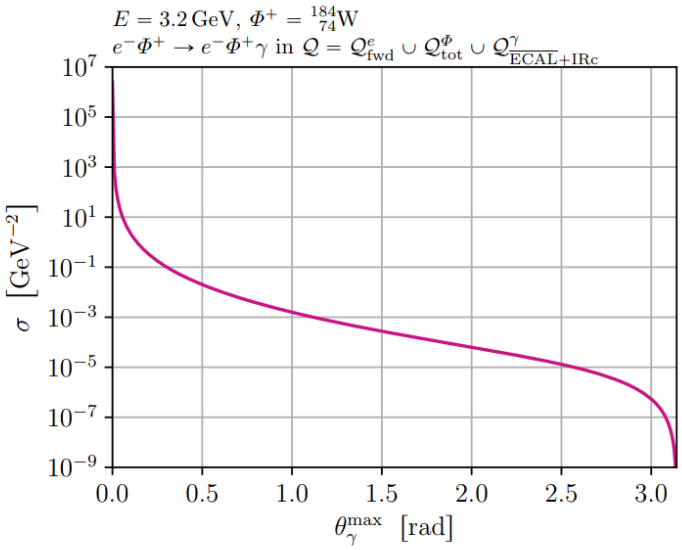

Figure 3.4: Cross section of the QED Bremsstrahlung process dependent on the maximum veto-able photon angle. Taken from [5].

3.3.2 Inelastic electro-nuclear Background

Another crucial background is the creation of undetected photons and hadrons during inelastic electro-nuclear interactions of the electron with the target nuclei. The beam electron can transfer a large amount of energy onto the target nucleus via the exchange of a virtual photon, breaking it up in the process. The low-momentum recoiling electron can be signal-like. During this interaction, various charged and neutral hadrons as well as photons emerge from the target. This can be seen on the left in figure 3.5. The number and type of particles produced during electro-nuclear interactions can vary largely. Some example processes from simulations[2] are given in the following:

- $e^- + \mathcal{H} \to e^- + \mathcal{H}' + \pi^0 + 3n + 5\gamma$,
- $e^- + \mathcal{H} \to e^- + \mathcal{H}' + \gamma + 8n + 2p + 7\gamma$,
- $e^- + \mathcal{H} \to e^- + \mathcal{H}' + \pi^- + 3p + 4n + 6\gamma$,
- $e^- + \mathcal{H} \to e^- + \mathcal{H}' + 2\pi^0 + \pi^+ + K^0 + \Lambda + 31n + 9p + 5\gamma$.

The $\mathcal{H}'$ corresponds to the nucleus after the interaction, which might differ from $\mathcal{H}$. All of these processes have in common that only a few $O(1)$ of the secondary particles obtain a large amount $O(\mathrm{GeV})$ energy and the rest of the particles have energies of 1 to 100 MeV. In all examples the incoming electron has an energy of 3.2 GeV and the recoiling electron has less than 100 MeV. Secondary particles from electro-nuclear interactions can thus obtain a large amount of energy and large angles and might not be detected by a forward placed calorimeter. It is therefore important that the veto strategy for these particles is investigated and potentially improved, to reduce the background caused by electro-nuclear

[2] The example events are simulated with the FLUKA simulation framework.

interactions. These backgrounds at Lohengrin are not yet well understood and are thus subject to the studies of this thesis. In section 3.6 a modelling approach for electro-nuclear interactions is presented and simulations regarding electro-nuclear interactions are investigated in the following chapters.

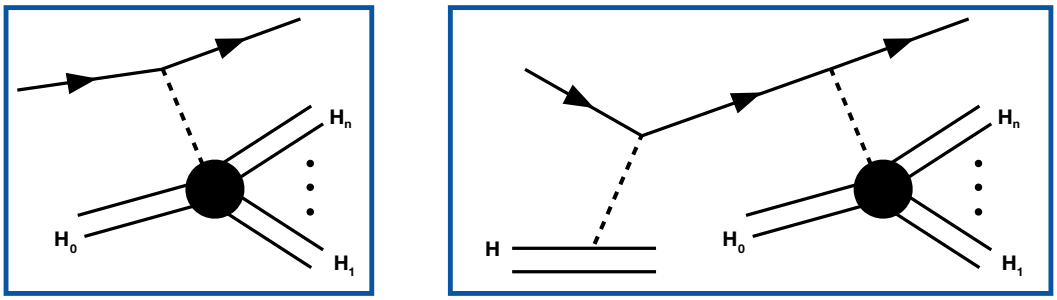

Figure 3.5: Schematic of an electro-nuclear interaction (left) and a photo-nuclear interaction of a secondary photon from bremsstrahlung (right). The hadronic systems are denoted by two lines and photons by dashed lines.

3.3.3 Inelastic photo-nuclear Background

Another background are photo-nuclear interactions. A photon created via hard bremsstrahlung of the initial electron can undergo a photo-nuclear interaction in the target or any other material in the detector setup. In figure 3.5 on the right, the Feynman diagram of this process can be seen. The process is similar to electro-nuclear interactions at Lohengrin, except a real photon interacts with the nucleus instead of a virtual photon and there is an additional vertex from the hard bremsstrahlung. If the secondary particles from this interaction are not detected, they contribute to the irreducible background. [5]

3.3.4 Neutrino Background

Neutrinos are produced mainly through the decay of secondary muons or pions or interactions with the Z boson. Since neutrinos cannot be detected by the detectors presented in this thesis (see section 3.4), they contribute to the irreducible backgrounds for the Lohengrin experiment. However, events where a high-energy neutrino carries a large part of the momentum and no other particle is detected, are extremely rare. [5]

3.4 Detector Setup

In the context of the detector setup, the coordinate system is important and will be introduced shortly. In the course of the thesis the z axis is always defined as the axis along the beam line and going through the center of each detector component. The incoming electron beam is directed in the direction of the positive z axis. The x and y axis make up the plane perpendicular to the beam axis, with the positive y axis pointing upwards. The origin of the coordinate system is placed in the center of the target, and the point $(x, y) = (0, 0)$ lays in the center of the detector components at varying z. Important are also the angles in this discussion, with the spherical angles θ and ϕ defined as follows:

$$\theta = \arccos p_z/r \quad , \quad \phi = \arccos \frac{p_x}{\sqrt{p_x + p_y}} \quad , \tag{3.5}$$

where the radius r is defined as,

$$r = \sqrt{p_x^2 + p_y^2 + p_z^2} \quad . \tag{3.6}$$

The components p_x, p_y and p_z correspond to the momentum components of a particle traversing the detector setup. The angle θ is therefore the angle between particle track and beam axis and angle ϕ corresponds to the angle between the x axis and the projection of the particle track in the xy-plane. [49]

A schematic overview of the detector set up can be viewed in figure 3.6. The setup consists of a tungsten target, tracking layers up- and downstream of the target, a magnet and corresponding magnetic field and a hadronic (HCal) and electromagnetic calorimeter (ECal). Signatures of different particles are drawn to schematically show the detection strategies. On the top an exemplary signal event is drawn with the recoiling electron and the dark photon, which passes the detectors unnoticed. Additionally in the center of the figure a background event with secondary neutral hadrons and photons is drawn. The neutral hadrons and photons are detected via the creation of hadronic or electromagnetic showers in the HCal and ECal. On the bottom of the figure a background event with a signal-like signature is provided. In this case the created neutral hadrons and photons are not detected in the current setup. Charged hadrons leave additional tracks in the tracking detectors downstream of the target and events can thus be rejected if there is more than one charged track in the final state. It is important to investigate what percentage of electro-nuclear events go undetected and thus leave a signal-like signature in the detector setup.

In addition a CAD rendering of the current detector setup is supplied in figure 3.7. A short overview of the components of the setup will be given in the following. For a detailed description and discussion of the detector setup see [5].

Target

The target proposed for the Lohengrin experiment is made up of tungsten and has a thickness of $0.1 \cdot X_0 \approx 0.035\,\text{cm}$ [50]. In the xy-plane it extends from $-7.5\,\text{cm}$ to $7.5\,\text{cm}$ making it $13\,\text{cm} \times 13\,\text{cm}$ large. The material tungsten was chosen mainly due to its small radiation length, which allows for a thin target and thus reasonably thin material budget. Additionally the main isotope of tungsten is a scalar nucleus, simplifying signal modelling and simulations. [5]

Tracking Layers

Up- and downstream of the target ultra-thin silicon pixel detectors measure the tracks of incoming beam particles and outgoing electrons behind the target, as well as any charged final state particles. In the current design of the experiment three tracking layers are placed upstream of the target and a number of tracking layers are placed downstream of the target. This is used to measure the presence of a beam electron in the initial state, as well as tracking of recoiling electrons in the final state. A preliminary design for the tracking detectors is based on the TJ-Monopix2 ASIC, which consists of a matrix of 512×512 square pixels with a pitch of $33.04\,\mu\text{m}$ in both directions. Each tracking plane has 4 such ASICs placed around the center of the xy-plane. However this is not yet the final design and optimisation studies are still ongoing.

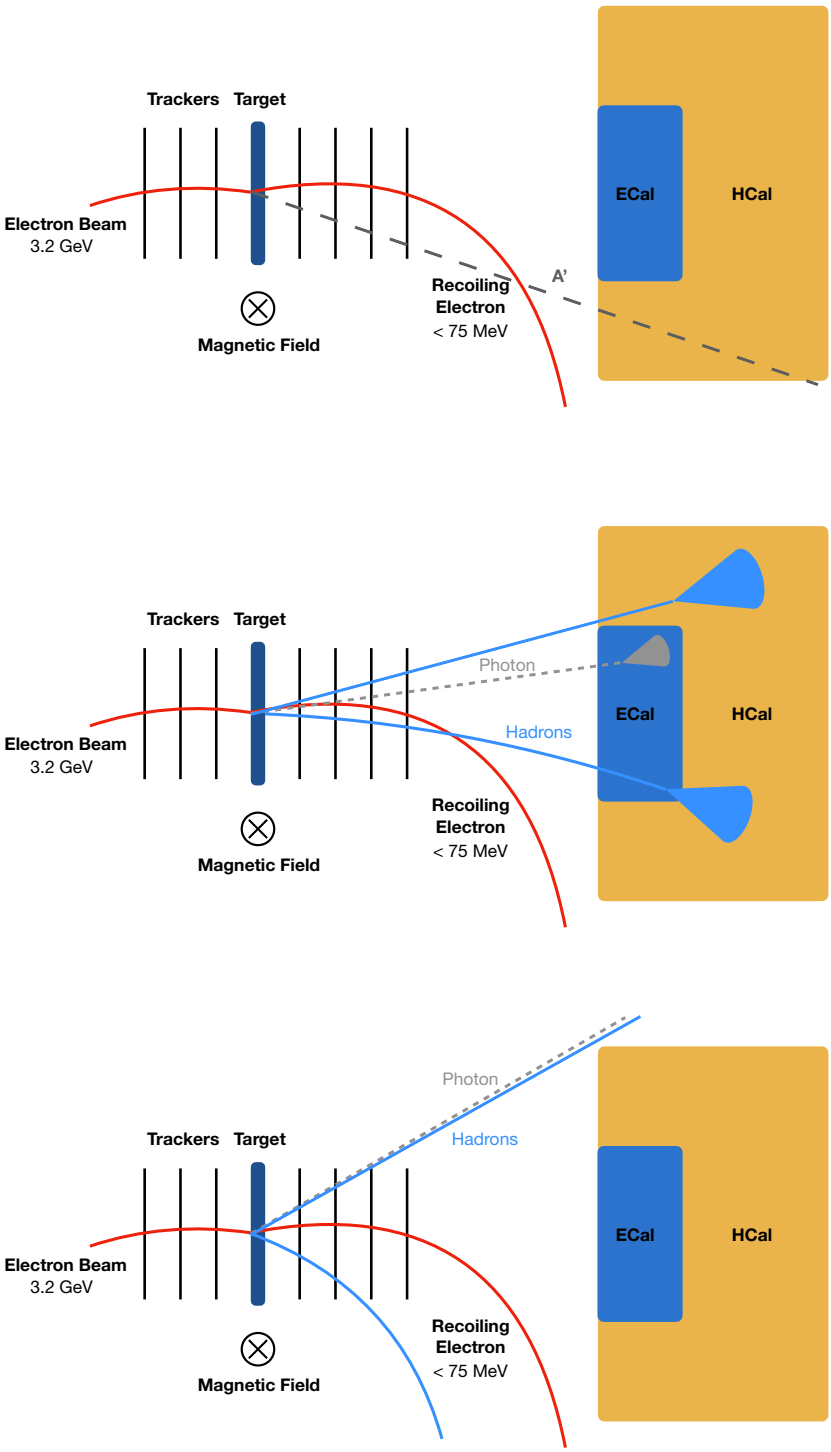

Figure 3.6: Schematic detector set up for the LOHENGRIN experiment consisting of the target, the tracking layers up- and downstream of the target, a magnetic field and magnet, an electromagnetic calorimeter and a hadronic calorimeter. Drawn are the signal process (top), neutral hadron and photon backgrounds (middle) and signal-like backgrounds (bottom). Adapted from [5].

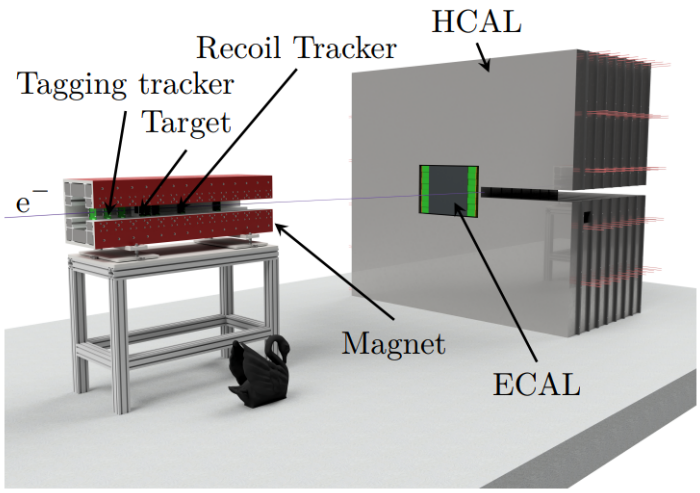

Figure 3.7: A CAD rendering of the detector setup for LOHENGRIN including the magnet, tracking layers, target, the electromagnetic calorimeter and hadronic calorimeter. The path of the non-interacting electron beam is indicated in purple. Taken from [5].

Magnet

The proposed design of the magnet surrounding the target and the tracking layers is an iron-dominated magnet built in a rectangular "C"-shape. The opening along the side is to avoid pollution of the tracking region by backscattered electrons or particles produced during interactions with the magnet material. With a magnetic flux of $B = 0.9\,\mathrm{T}$ in the positive y-direction, it deflects the beam electrons away from the ECal placed approximately 3.5 m behind the target. Additionally momentum measurements of the recoiling electron can be obtained from the curvature of the track and the measurements in the tracking detectors. The magnet shape can be viewed in figure 3.7 in red. The exact realisation of the magnet is not finalised, and still under investigation.

Calorimeters

To veto both photons and charged and neutral hadrons an electromagnetic and hadronic calorimeter are needed in the detector setup. Due to the high rate of SM photons the ECal needs to be able to process high rates and must be radiation hard. Thus the electromagnetic calorimeter is a sampling calorimeter made up of alternating layers of tungsten absorbers and active silicon layers. The design is oriented at the CALICE ECal, see figure 3.8. It has the dimensions $48\,\mathrm{cm} \times 48\,\mathrm{cm}$ in the xy-plane and is in total $(0.42\,\mathrm{cm} + 0.01\,\mathrm{cm} + 0.065\,\mathrm{cm} + 0.54\,\mathrm{cm}) \cdot 15 = 15.525\,\mathrm{cm}$ long. The thicknesses of the individual components are $d_{\mathrm{abs.}} = 0.42\,\mathrm{cm}$ for the absorber, $d_{\mathrm{si.}} = 0.065\,\mathrm{cm}$ is the thickness of the active silicon layers and $d_{\mathrm{sep.}} = 0.01\,\mathrm{cm}$ is the thickness of the air between the two materials to account for glueing. Each tungsten-silicon layer is separated by $d_{\mathrm{dist.layer}} = 0.54\,\mathrm{cm}$. The active silicon layers contain 96×96 segmented silicon sensors with pixel sizes of $5\,\mathrm{mm} \times 5\,\mathrm{mm}$. The ECal is designed in a way such that the whole particle shower is contained in the depth of the detector, meaning a photon that will hit the ECal at its center, will produce an electromagnetic shower that is contained in the ECal. However, leakages of

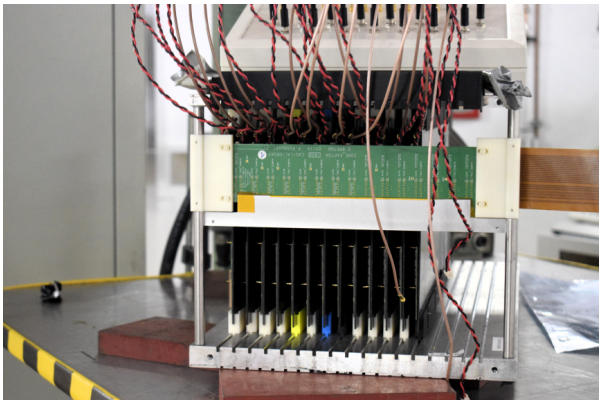

Figure 3.8: Photograph of the CALICE ECal prototype from 2021, taken from [5]

.

particles in the HCal in the xy plane are possible, for example if the photon hits the ECal at its edge or with a transverse angle.

The ECal is embedded into a hadronic calorimeter to provide an additional veto for hadrons. The HCal is also a sampling calorimeter and has the dimensions of 270 cm × 250 cm in the xy-plane. For the purpose of this thesis it consists of 71 layers of iron absorber material and active silicon material, which will make it in total $(1.72\,\text{cm} + 0.3\,\text{cm}) \cdot 71 = 143.42\,\text{cm}$ long. Where the thickness of the absorber is $d_{\text{abs.}} = 1.72\,\text{cm}$ and of the active silicon layers $d_{\text{sens.}} = 0.3\,\text{cm}$. The exact dimensions and realisation of the HCal are not fixed and are still under study. Additionally the HCal has a slit along the positive x axis, extending through the whole depth of the calorimeter in z direction, as can be seen in figure 3.7. The deflected beam electrons are directed through the slit and signal rates produced by beam electrons are thus reduced in the HCal. [5]
With this geometric setup the calorimeters have an angular coverage of 0.1 rad for the ECal and 0.6 rad for the HCal, which will become important throughout this thesis.

3.5 Signal region

The general idea of this thesis is understanding hadronic backgrounds of the LOHENGRIN experiment, regarding the current detector setup. Especially interesting are backgrounds that mimic signal-like signatures. A signal event at the LOHENGRIN experiment has the following properties:

- a single electron present in the initial state,
- exactly one signal electron with less than 75 MeV,
- no significant energy deposition in the ECal that is consistent with a high-energy photon,
- no hadronic activity in the final state, meaning no significant energy deposits in the HCal and
- the absence of any charged track other than the signal electron in the final state. [5]

If an electron leaves a signal-like signature in the detectors, all other outgoing final state particles need to be detected, otherwise a fake signal-event would be produced. The detector setup is designed

to account for backgrounds, as given in [5]. The focus of this thesis is on potential backgrounds and veto strategies for electro-nuclear interactions not tackled by the strategies given above. The tracking of the initial and final state electron plays a large role in the sensitivity of the experiment, but a detailed summary of the tracking algorithm is beyond the scope of this work and can be found in [51]. The main focus are electro-nuclear interactions and hadronic backgrounds produced from electrons in the target.

3.6 Modelling of electro-nuclear backgrounds

Hadronic backgrounds are produced by electro-nuclear interactions of the initial beam electron with the nuclei of the target or any other sensitive material in the detector setup. To model electro-nuclear backgrounds often the so-called Equivalent Photon Approximation (EPA) is used. Previously electro-nuclear interactions have been introduced as an electron interacting with a nucleus via virtual photon exchange. This concept is the underlying idea of the EPA and will be explained in the following. The EPA approach starts with observations from electrons and photons traversing a gas volume: in both cases gas atoms are either excited or ionised depending on the electrons or photons velocity. The underlying interaction of an electrically charged particle with a gas atom is thus similar to that of a photon of a specific frequency. If - for example an electron - traverses a point in space, a variable electrical field arises at that point and if one decomposes that field via a Fourier Integral into only harmonic components, then that field corresponds to the field produced by light of a specific continuos frequency distribution. Placing an atom at that point and using the above considerations, it is obvious that the electric field of the electron excites and ionises the atom in the same manner as the equivalent electric field of the photon. Thus the interaction of an electron with an atom can be approximated as the interaction with an equivalent photon. [52]

To obtain the cross section for the electro-nuclear interaction in dependence of the cross section of the photo-production, the Feynman diagram in figure 3.9 is considered, which depicts the following reaction:

$$a + \mathcal{H} \rightarrow \mathcal{H} + A \quad , \tag{3.7}$$

where the incoming particle a corresponds to a very fast electron with momentum p, the nucleus $\mathcal{H}$ has momentum P_1 before and P_2 after the interaction and A denotes possible particles created. The virtual photon exchanged between the electron and nucleus has the momentum $q = P_1 - P_2$. At sufficiently small $q^2 \ll m_e^2$ the right part of the graph in figure 3.9 corresponds to the interaction of a photon with the incoming particle a of the form

$$\gamma + a \rightarrow A \quad , \tag{3.8}$$

producing a number of particles A. Thus the cross section σ_e of the electro-nuclear process can be expressed using the cross section of the photo-process and is given by

$$\mathrm{d}\sigma_e = \frac{Z^2\alpha}{\pi} \frac{\mathrm{d}\omega^2}{\omega^2 - m^2} \frac{\mathrm{d}q^2}{(q^2)^2} \left[q^2 - \left(\frac{\omega^2 - m^2}{2E_L} \right)^2 \right] \mathrm{d}\sigma_p(\omega) \quad , \tag{3.9}$$

with Z corresponding to the atomic number of the atomic nucleus, E_L is the energy of the incoming particle in the lab system, and m its mass. In this instance an integration over the angle ϕ has been done already. The differential cross section of the photo-process is $\mathrm{d}\sigma_p(\omega)$ and it is averaged over

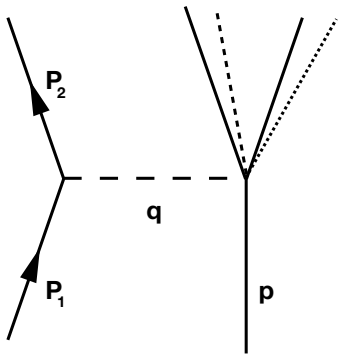

Figure 3.9: Feynman diagram of an electro-nuclear interaction of particle with momentum p on a nucleus with momentum P_1 and a virtual photon with momentum $q = P_1 - P_2$. Adapted from [53].

polarizations. It can be expressed by

$$\mathrm{d}\sigma_p(\omega) = \frac{(2\pi)^4}{2q_0 m} g_a f |e_\mu R_\mu|^2 \delta(q + p - Q)\mathrm{d}\Gamma \quad . \tag{3.10}$$

Here $\mathrm{d}\Gamma = \Pi_{(A)}(\mathrm{d}^3 p_i/(2\pi)^3$, q_0 corresponds to the momentum of the photon in the system where $p = 0$, $f = \Pi_{(A)} f_i$, with $f_i = m_i/E_i$ for fermions and $f_i = \frac{1}{2}E_i^- 1$ for bosons. The factor g_a is equal to m for fermions and equal to $\frac{1}{2}$ is the particle a is a boson. The momentum of the particles combined in A is given by Q. [53] With this approximation the electro-nuclear interactions are calculated and thus hadronic backgrounds can be modelled. Many simulation frameworks use this underlying model to handle electro-nuclear interactions.

3.7 Physics reach

It has become apparent throughout the previous sections that the Lohengrin experiment aims to detect dark matter via a missing momentum approach. To estimate the physics reach and feasibility of experiments their sensitivity is estimated. Since the experiment is still in development, the sensitivity of the experiment can be estimated using various factors. The baseline scenario will be introduced here and a more aggressive signal region and thus physics reach can be found in [5]. In the baseline scenario the signal region is determined by:

- a single electron present in the initial state,
- a single electron present in the final state with an energy between 25 to 75 MeV,
- energy depositions below ≈20 MeV in the ECal and
- no significant energy deposition in the HCal.

The minimum cut on the energy of the recoiling electron is mainly motivated by the significantly decreasing ability to track the electron at energies below 25 MeV.

For the planned $4 \cdot 10^{14}$ e.o.t. the Lohengrin experiment will cover the dark sector parameter space up to the expected properties of scalar dark matter in the mass range $2\,\text{MeV} \leq m_\chi \leq 30\,\text{MeV}$. Here a fraction of the dark photon mass to dark matter mass of roughly $m_{A'}/m_\chi = 3$ is assumed. A total of $1 - 100$ signal events are expected for this amount of electrons on target. [5]

The estimated sensitivity of the Lohengrin experiment can be seen in figure 3.10 in comparison to existing bounds. Tuning some of the variables, such as removing the minimum energy cut on the recoiling electron, reducing backgrounds further by extending the ECal and extending the beam time, the Lohengrin experiment would be able to probe the dark sector up to Marjorana dark matter in the same mass range or even Pseudo-Dirac dark matter. [5]

The above explained scenario assumes a highly idealized HCal with immaculate veto efficiency and a total of 10 hadronic background events in the final state. Depending on the electro-nuclear kinematics and angular coverage of the hadronic calorimeter, more undetected hadronic signal signatures are expected. The impact of hadronic background events on the sensitivity of the experiment can be seen in figure 3.11. In the presented figure a different scenario for the Lohengrin experiment is used with 10^{15} e.o.t. and an extended ECal coverage $\phi > \pi/4\,\text{rad}$. [5] Throughout this thesis the first - so the baseline - scenario will be used as reference and comparison, though the presented figures in 3.11 emphasize the importance of hadronic events in the signal region for the sensitivity of the experiment. As an illustration, five different number of hadronic background events $\mathrm{n_{had}}$ in the signal region are presented. It is obvious from previous discussions and the figure, that the hadronic backgrounds have a massive impact on the sensitivity of the experiment. For $0 < n_{\text{had}} < 100$, searches for scalar LDM are possible and at higher magnitudes $O(10^3 - 10^4)$ the search for LDM gets increasingly difficult to impossible. Hence the background suppression of the HCal and ECal must be highly efficient. In this context primarily the understanding of electro-nuclear backgrounds and their impact on the sensitivity of the experiment are of tremendous importance.

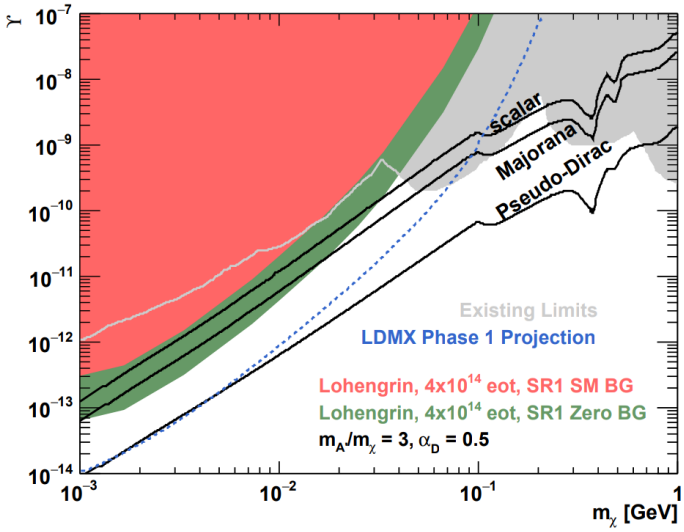

Figure 3.10: Estimated sensitivity of the LOHENGRIN experiment for the baseline scenario. The red area shows the expected sensitivity including the estimated backgrounds, the green area indicates the statistical limits assuming a background free search and the gray area shows existing limits from various experiments. In blue the LDMX phase 1 projection is given. Taken from [5].

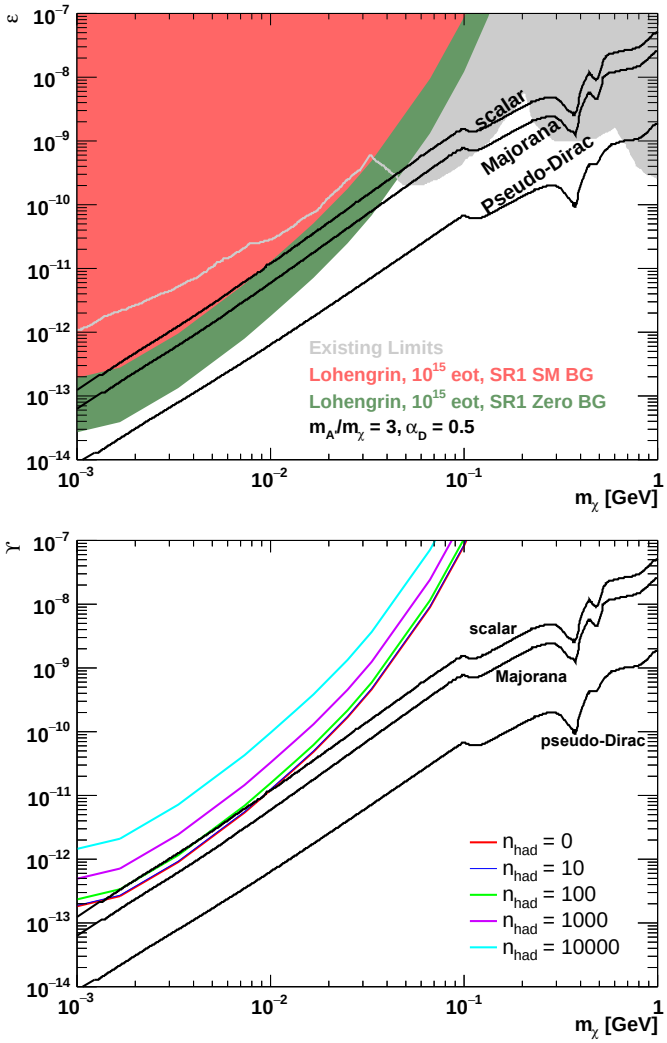

Figure 3.11: Estimated sensitivity of the LOHENGRIN experiment for 10^{15} e.o.t. and an extended ECal coverage (top) and with different number of hadronic background events in the signal region (bottom). Taken from [5, 54].

CHAPTER 4

GEANT4 event generator for LOHENGRIN

To comprehend hadronic backgrounds at LOHENGRIN, a stand-alone simulation in GEANT4 (GEometry AND tracking) is implemented. Although GEANT4 specialises in detector response simulations, the simulation framework is used as a tool to investigate electro-nuclear interactions [55, 56]. This approach is inspired by the LDMX experiment, which used GEANT4 to demonstrate the minimal impact of electro-nuclear interactions on its signal region [39]. Thus the stand-alone simulation in GEANT4 serves as an event generator to get a first understanding of the types of particles created and their angular and energy distributions. GEANT4 is a Monte Carlo toolkit for the simulation of the passage of particles through matter and is widely used in high-energy, nuclear, accelerator and medical physics. One principal purpose of GEANT4 is the simulation of particle detectors and their responses, which requires the modelling of the interactions of various particle types with matter. Given its focus on detector response simulations, not all physics processes are implemented with the highest level of precision, and some features may contain bugs - particularly in areas outside the toolkit's most common or standard use cases. GEANT4 covers an energy range of meV for thermal neutrons up to hundreds of GeV and includes a complete set of physics processes for electromagnetic, strong and weak interactions of particles in matter. Physics model implementations for each type of interaction are provided and some modelling approaches are available in so-called *physics lists*. [55, 57]

To isolate electro-nuclear interactions and to get a better understanding of the process, GEANT4 is used as an event-generator in the following. The simulation of the detailed detector setup is not necessary to study the electro-nuclear process on a fundamental level and it is sufficient to simulate the interaction of the incoming electron with the target. The geometry of the setup and the physics list used for the study of the electro-nuclear interactions in GEANT4 will be discussed in section 4.1. During the simulation of the electro-nuclear processes several issues in the kinematics of the interactions arose, which will be explained in section 4.2. Results of the electro-nuclear interactions in GEANT4 will be presented in section 4.3 and at the end of the chapter a short discussion of photo-nuclear interactions in GEANT4 will be done, see section 4.4.

It is important to emphasize that all discussed values throughout this thesis represent expectation values and therefore inherently carry statistical uncertainties. Systematic uncertainties arising from the simulation, e.g. errors on cross sections, are disregarded at this point, as this is a rather qualitative than quantitative discussion. For future work - particularly in technical studies of the detector setup - such systematic effects need to be taken into account.

4.1 Geometry setup and physics list

Since GEANT4 is used as an event generator to study isolated electro-nuclear processes, only the necessary components of the experiment are added to the simulation. Therefore only the target and the beam are simulated and the outgoing particles are analysed.

In GEANT4 all detector components are placed in a large world volume. Particles inside that volume are propagated and interact with matter placed within the volume according to the physics list chosen. All particle tracks are not further propagated outside of the world volume. Hence the world volume needs to be chosen sufficiently large, such that all necessary components fit inside it. For the purpose of using GEANT4 as an event generator, a world volume of $(x, y, z) = (1\,\text{m}, 1\,\text{m}, 1\,\text{m})$ is chosen. The coordinate system is the same as explained in section 3.4, with the origin of the coordinate system in the center of the world volume and the beam is directed along the positive z axis. The implemented target consists of tungsten, specifically ^{184}W, as motivated in the previous chapter 3. A study on the impact of the fermionic tungsten isotope is conducted in section 5.4 in the next chapter.

The target extends from $-7.5\,\text{cm}$ to $7.5\,\text{cm}$ in both the x and y directions and is $0.1 \cdot X_0 = 0.03504\,\text{cm}$ long. The target is placed at $(0, 0, 0)$ in the world volume, which is filled with vacuum. The beam is positioned at $z = -50\,\text{cm}$ and centered in the xy plane. This position is arbitrary, as long as it is centered in xy and in front of the target, as the beam will interact only there. The beam energy is set to $3.2\,\text{GeV}$ as explained in section 3.4.

One so-called *event* in GEANT4 corresponds to a single beam electron propagating through the world volume, its interaction with the target nuclei and all secondary particles from the interaction. The secondary particles are simulated and can be recorded. It is important to emphasise that in the context of the simulation framework a single event corresponds to a single electron and its interaction in the target. However, at the LOHENGRIN experiment a single event may contain more than one electron on target. All events are part of a collective *run* with a number of electrons on target (e.o.t.) that can be specified individually.

The physics list used during simulations with GEANT4 throughout this thesis is the `FTFP_BERT` list, which is the current default in GEANT4. From 0 to 5 GeV incident hadron energy, it uses the GEANT4 Bertini cascade for hadron-nucleus interactions and the `FTF` parton string model for hadron-nucleus interactions from 4 GeV onwards. After high energy `FTF` interactions have been completed, it uses the GEANT4 pre-compound mode (hence the letter "P") to de-excite nuclei. [58] The "`BERT`" part of the physics list stands for the intranuclear cascade model in use, which in this case is the Bertini cascade. An intranuclear cascade is a cascade of hadrons and nucleons produced through a series of interactions within the nucleus, initiated by a particle. If there are only few collisions and the effective nucleon size is small, the nuclear medium can be considered a "gas". Thus making the intranuclear cascade a classical model, solving the Boltzmann equation for the transport of a particle through a "gas" of nucleons. However, this is only valid for incident particle energies up to 3 GeV. Above this energy the classical model fails, as for example the Lorentz contraction of the target nucleus, causes the nucleons to come too close together to be considered a gas. The newer, extended Bertini cascade includes incident particle energies between 0 to 15 GeV. Some of the extensions include adding strange particles and states with higher multiplicities to the model and also photo-nuclear interactions and muon capture. [59]

The most important update of the Bertini cascade for this thesis is the inclusion of photo-nuclear and therefore electro-nuclear interactions, which are based on the EPA approach explained in section 3.6 [60]. The lepto-nuclear interactions are simulated as a virtual photon exchange between the lepton

and a nucleon in the target. The virtual photon is created at an electromagnetic vertex generated by the electron in `G4ElectroVDNuclearModel` and then a real photon is produced from the virtual photon spectrum. At low energies (below 10 GeV) the photon is treated as a hadron interacting with a nucleon, thus initiating the intranuclear Bertini cascade for the electro-nuclear interaction. For electro-nuclear interactions the process is divided into a electromagnetic vertex, where the virtual particle is created, and a hadronic vertex, where the virtual particle interacts with the target nucleus. At high energies the photon is treated as a π^0 and handed to the FTF high energy model. [58] Particles of the cascade can either leave or be trapped in the nucleus depending on their energy. If the secondary particle has a kinetic energy below the nuclear potential, it is trapped in the nucleus and later decayed or recombined with the nucleus. Only particles with an energy above the nuclear potential will be propagated outside of the nucleus and are part of the final state particles of that cascade. [59] [61]

With this simple geometry setup and the standard physics list, the electro-nuclear interactions can be simulated in GEANT4 and secondary particles can be analysed regarding their energy and angular distributions.

4.2 Momentum Conservation in GEANT4

When analysing the kinematics of electro-nuclear interactions in GEANT4, some odd behaviour of the final state particles was observed. A simple sanity check of 4-momentum conservation was implemented prior to any further analysis and it became apparent that momentum conservation was not fulfilled by many of the electro-nuclear events. This can be seen in figure 4.1, where the momentum components p_x, p_y and p_z of the recoiling electron that has undergone an electro-nuclear interaction are plotted against the final missing momentum. The missing momentum corresponds to $p_x^{\text{miss}} = -\sum_i p_{x,i}$, where $p_{x,i}$ is the momentum of final state particle i. In particular for the components p_x and p_y, the recoiling electron obtains exactly the amount of missing momentum of that event. This hints at an issue with the frame of reference.

The momentum component p_z however, does not show this correlation between the recoiling electron and final missing momentum. Therefore another issue must be present during the simulation of electro-nuclear interactions. When investigating the electro-nuclear events in more detail, the second reason for the momentum conservation violation can be found. Since electro-nuclear interactions in GEANT4 are calculated with the EPA approach, the electron interacts with the nucleus via virtual photon exchange. This virtual photon can have values of $q^2 \neq 0$. When the virtual photon is converted into a real photon, its momentum is cut-off to maintain $q^2 = 0$ for the real photon. To ensure $q^2 = 0$ for the real photon, either momentum or energy conservation must be violated and in the case of GEANT4 the photon momentum is cut-off. This can be highlighted by a simple example: in the case of an incoming electron with momentum $\vec{p} = p \cdot \vec{e}_z$, its momentum would be divided onto the recoiling electron and the photon in the following sense:

- Recoiling electron: $\vec{p}_e = p' \cdot \vec{e}_z + \vec{p}_x + \vec{p}_y$
- Transferred photon: $\vec{p}_\gamma = p'' \cdot \vec{e}_z - \vec{p}_x - \vec{p}_y$

Here the obtained transverse momentum of the recoiling electron and photon must add up to exactly zero. However, in GEANT4 the following 4-momenta of the recoiling electron and the transferred photon are obtained for an exemplary electro-nuclear interaction [54]:

- Recoiling electron: $\vec{p}_e = 2967.3046 \cdot \vec{e}_z + 57.01363 \cdot \vec{e}_x - 214.62580 \cdot \vec{e}_y$
- Transferred photon: $\vec{p}_\gamma = 162.33604 \cdot \vec{e}_z - 39.77461 \cdot \vec{e}_x + 149.73013 \cdot \vec{e}_y$

Though the signs are correct for the components p_x and p_y, the values for the transferred photon are smaller because they have been cut-off. This can be observed for many of the electro-nuclear events and if this cut-off momentum is introduced to the system again, then the missing momentum in the z component improves, see figure 4.2.

Since already it was suspected that there is an additional issue regarding the frame of reference, the kinematics of the electro-nuclear interactions were investigated further. The electro-nuclear vertex is created in `G4ElectroVDNuclearModel` and the kinematics are also handled there. In the source code the particles are created in the frame of reference, in which the transferred photon travels along the positive z axis. The secondary particles from electro-nuclear interactions are created in this reference frame and then not rotated back into the lab frame. Of course this causes issues in the momentum conservation, since the momenta are compared to the lab frame momentum of the electron. This can be fixed by adding the corresponding rotation of all secondary particles back into the lab frame to the source code. In figure 4.3 the improved momentum plots are given with the added missing momentum to the system and the rotation back into the lab frame of all secondary particles. It is clear that there is no more missing momentum in all momentum components. In the following the version of GEANT4 is used that has implemented the rotation of secondary particles into the lab frame. [54]

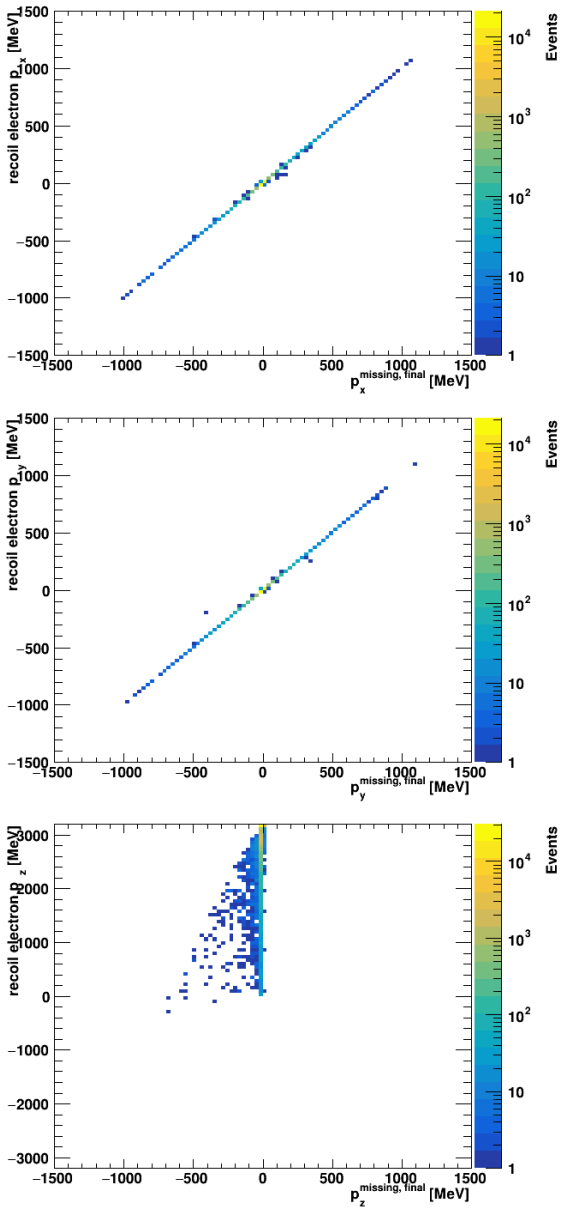

Figure 4.1: Momentum component p_i of the recoiling electron against the final missing momentum per event for momentum component p_i from a simulation of electro-nuclear interactions with the standard version of GEANT4. Taken from [54].

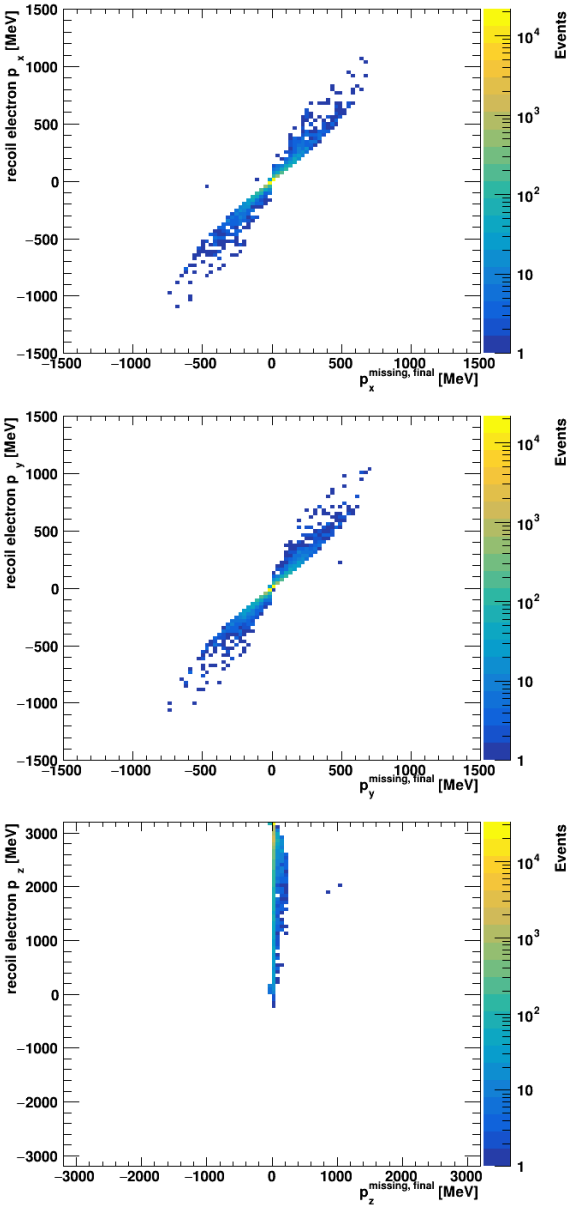

Figure 4.2: Momentum component p_i of the recoiling electron against the final missing momentum per event for momentum component p_i from a simulation of electro-nuclear interactions with the standard version of GEANT4, with the added missing momentum to the system. Taken from [54].

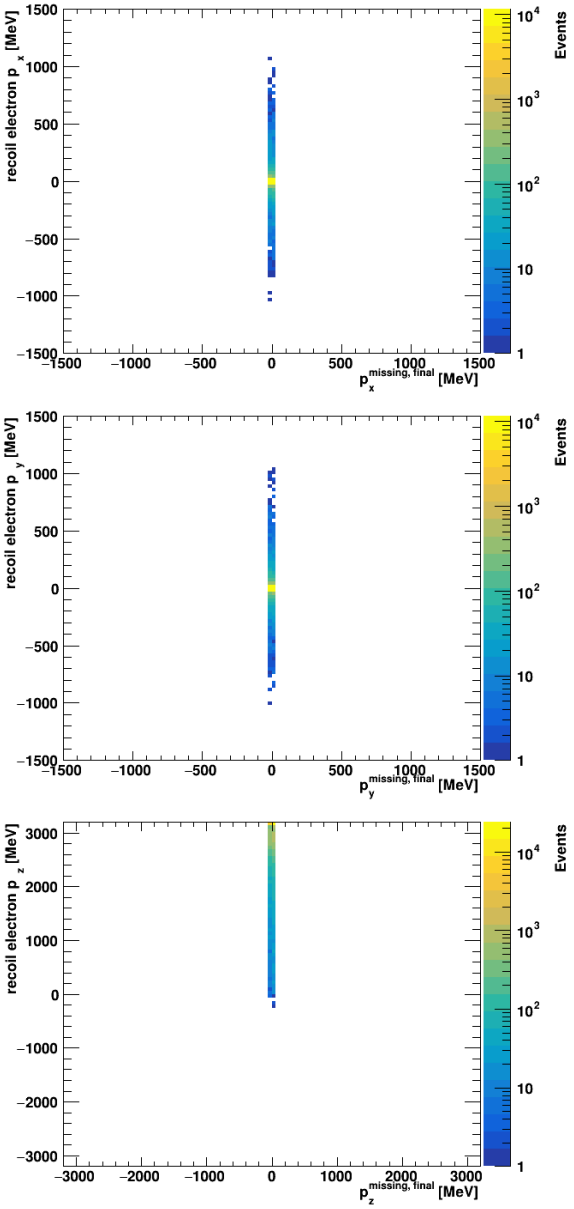

Figure 4.3: Momentum component p_i of the recoiling electron against the final missing momentum per event for momentum component p_i from a simulation of electro-nuclear interactions with the standard version of GEANT4 with the added missing momentum to the system and rotation corrected version of GEANT4. Taken from [54].

4.3 GEANT4 output

To get a first understanding of electro-nuclear interactions, $2.5 \cdot 10^9$ e.o.t. are simulated in GEANT4 and the results will be discussed in the following. Secondary particles of the electro-nuclear interactions are analysed at their first step in the simulation, so directly after creation.

In figure 4.4 the kinetic energy and angle θ of the recoiling electron are given. One can clearly see that in most cases the electron does not loose a significant amount of energy, which corresponds to the expectations and also shows that the majority of events lie outside the signal region. There are however cases, where the electron looses a substantial amount of energy and in combination with the distributions of the outgoing secondary particles, this will become crucial to the analysis. The angle θ of the recoiling electron is less than $\theta \leq 0.3\,\text{rad}$ for most of the events and only in a few $O(10)$ events the electron obtains angles larger than that. Events with a recoiling electron of $\theta > 0.2\,\text{rad}$ are vetoed due to the missing electron track in the final state and thus do not fall into the signal region at LOHENGRIN. When investigating the signal region of the recoiling electron in more detail, an interesting observation was made: In all cases, where the the momentum transfer to the virtual photon is larger than 3.125 MeV, so for recoiling electron energies below 75 MeV, the recoiling electron is scattered in forward direction with an exact value of $\theta = 0\,\text{rad}$. To understand, why the angle θ is always set to zero for these recoil energies, the source code was analysed. In the source code, where the electro-nuclear vertex is calculated, a cut-off value for the maximum transferred energy of the electron to the virtual photon is set, with the comment *"The region where the method does not work"*, see `G4ElectroNuclearCrossSection::GetEquivalentPhotonQ2()` in GEANT4 version 11.2.1 [62]. If the energy transfer exceeds a value of $\approx 3\,017\,\text{MeV}$, so the recoil electron would have an energy below $\approx 183\,\text{MeV}$, the q^2 of the virtual photon is set to zero. When calculating the kinematics of the recoiling electron, this $q^2 = 0$ value forces the angle $\theta = 0\,\text{rad}$. Since the signal region of the LOHENGRIN experiment lies in this energy range of the recoiling electron, no reliable results for the experiment can be obtained using GEANT4. In the following the data from GEANT4 are analysed further, after which an alternative event generator will be introduced in the next chapter.

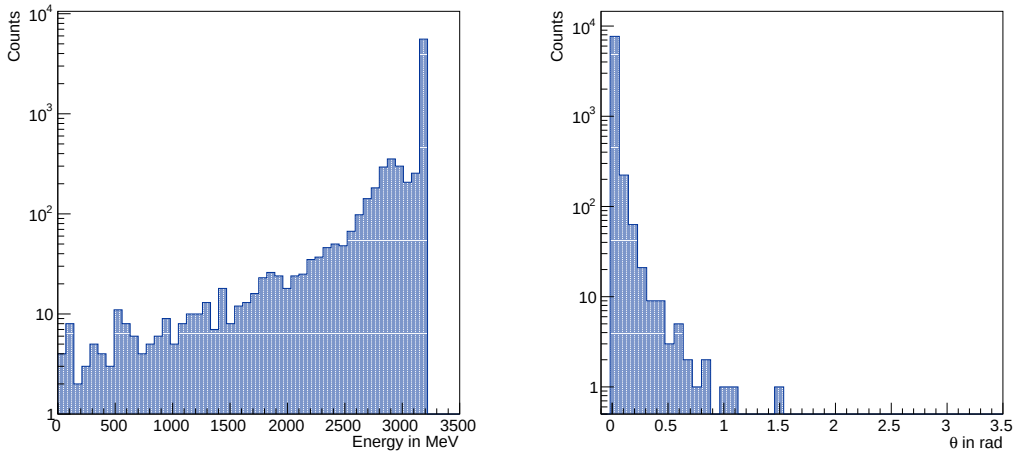

Figure 4.4: Kinetic energy (left) and θ of recoiling electrons (right) for a Geant4 simulation of $2.5 \cdot 10^9$ e.o.t..

In figure 4.5 the energy of the recoiling electron (as also given in figure 4.4) is plotted against the number of encountered hadrons per event. Additionally the number of hadrons with more than 500 MeV per event is provided in figure 4.5 on the right. The number of hadrons encountered in the final state per electro-nuclear event can vary largely. Most likely are events where the electron has lost no significant amount of energy and 0 to 3 hadrons are present in the final state. The overall distribution is reasonable, however events with zero hadrons are untypical for electro-nuclear interactions [63, 64]. Since separation energies of a few MeV are enough to separate nucleons from the target nuclei, at least $O(1)$ hadron should be emitted from the electro-nuclear interaction [9]. Whether the amount of events with zero hadrons is due to the model used in GEANT4 or there is another cut in the source code undiscovered, is unclear.

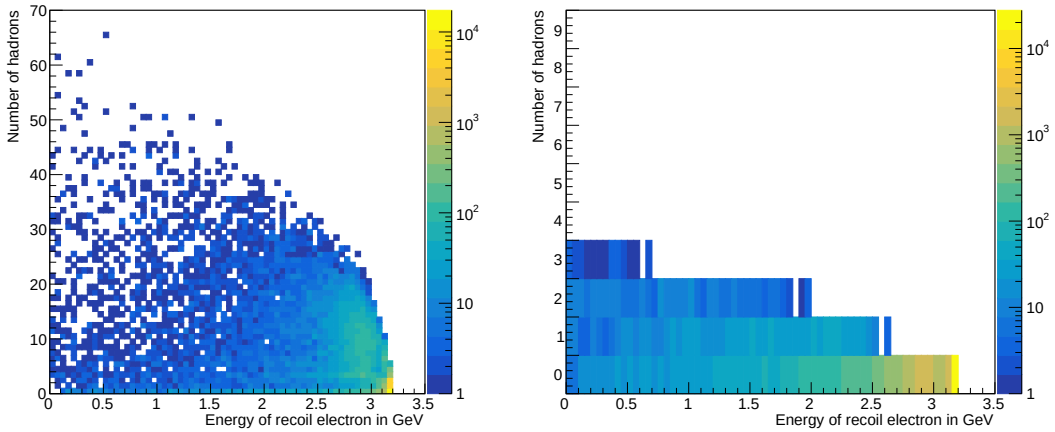

Figure 4.5: Number of encountered hadrons (left) and number of encountered hadrons with more than 500 MeV energy (right) per event against energy of the recoil electron for a GEANT4 simulation of $2.5 \cdot 10^9$ e.o.t.

One important aspect of this study is to understand which particles are encountered and might go undetected in the current detector design. In figure 4.6 the Particle Data Group (PDG) particle numbers for all encountered secondary hadrons of electro-nuclear interactions in the target are given. See table 5.1 for an overview of particles and their identification numbers. The most encountered particles are neutrons (2112) and protons (2212) [65]. Other encountered particles are pions π^+ (211), π^- (-211) and π^0 (111) and kaons K^+ (321), K^- (-321) or K^0_L (130). Hadrons in the region between Id 3000 and 3500 are charged and neutral Σ baryons. It is important that all events with charged and neutral hadrons are detected in the calorimeters, to maintain sensitivity in the signal region. Though events where a charged hadron produces a track in the tracking layers can also be vetoed. To get a handle on the energies and angles the hadrons obtain from the electro-nuclear interaction, they will be examined in the following. Additionally the distributions for the photons will be analysed and compared.

In figure 4.7 the kinetic energy of photons and hadrons are presented. The secondary photons only obtain energies of a few $O(\text{MeV})$, whereas the secondary hadrons can have energies up to 3 GeV. Though most hadrons also obtain only a small amount of kinetic energy up to 100 MeV.

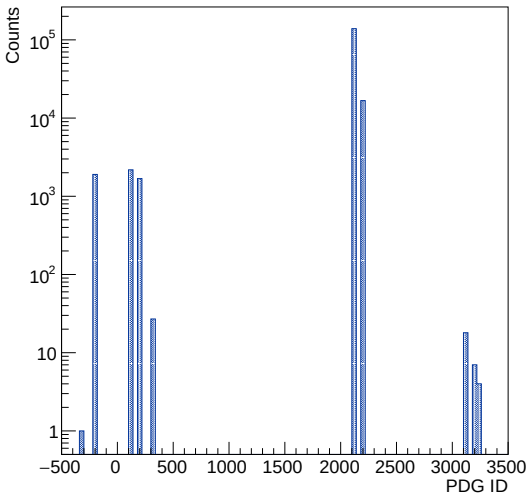

Figure 4.6: PDG particle Ids of encountered secondary hadrons for a Geant4 simulation with $2.5 \cdot 10^9$ e.o.t..

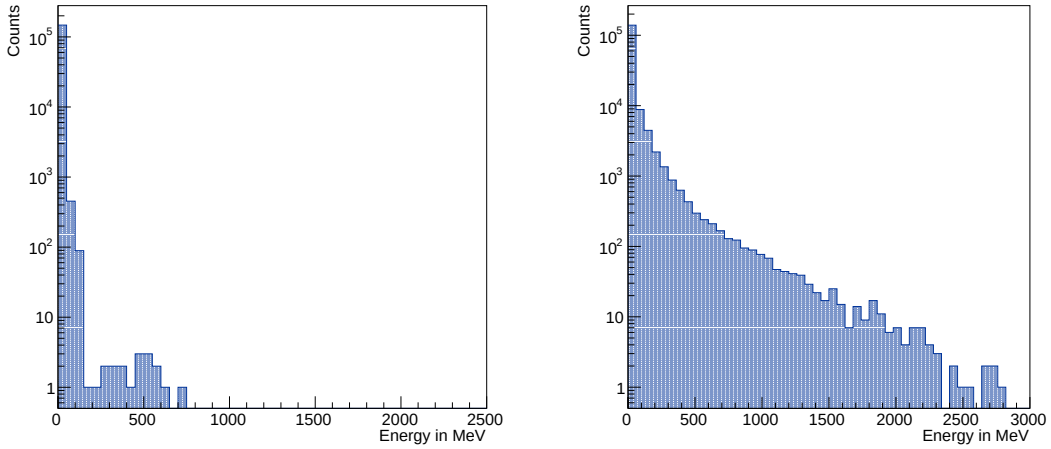

Figure 4.7: Kinetic energy of photons (left) and hadrons (right) for a Geant4 simulation of $2.5 \cdot 10^9$ electrons on target.

In figures 4.8 and 4.9 the angles ϕ and θ for secondary photons and hadrons are provided. The artifacts in the θ and ϕ distributions arise from the use of the standard `FTFP_BERT` physics list, in particular when including `G4HadronElasticPhysics`, which handles elastic interactions of hadrons [61]. The distribution of ϕ for both secondary photons and hadrons has distinct peaks at 0 rad, π and 2π. These artifacts are especially visible in the secondary photon ϕ distribution. When analysing the kinematics of events with photons emerging the target at such angles, it became apparent that GEANT4 creates many secondary particles with $\vec{p} = 0$. These are particles that convert in the simulation, do not obtain any momentum and energy and are only created due to technical reasons. Since these are not actual final

state particles, they need to be excluded in the distribution. This can be seen in figure 4.10, where only secondary particles with $p_z \neq 0$ are included.

Including `G4HadronElasticPhysics` in the physics list also causes the dent in the θ distribution for the secondary particles. This dent is not expected in the spectrum and might be another effect of the way GEANT4 handles electro-nuclear kinematics.

Excluding the dents in θ and the artifacts in ϕ, the distributions are isotropic. The choice of coordinates gives rise to the sine-shape of the θ distribution, as it takes the area of the sphere into account, whereas ϕ is isotropic when evenly distributed. This simply means that if spots on a sphere are isotropically distributed, more accumulate around the equator of the sphere than at the poles. The angular distribution of θ for the hadrons is slightly shifted towards smaller angles, hinting at the existence of some high-energy hadrons boosted in forward direction.

Reason for the roughly isotropic distribution is that in electro-nuclear events, only a few $O(1)$ hadrons obtain a large amount of energy, while the rest of the low-energetic hadrons are radiated off the nucleus during its de-excitation. Applying a cut on hadrons with energies above 500 MeV, the distribution shifts towards smaller angles, verifying the existence of some high-energy secondary hadrons that emerge the target with smaller angles, see figure 4.11. Though from the loss of statistics the rareness of the high-energy hadrons can be seen. Thus electro-nuclear interactions are dominated by low-energy isotropically distributed secondary particles. The same can be done for the photons emerging from electro-nuclear interactions. In figure 4.12 the corresponding distributions for photons with energies above 200 MeV are given. Compared to the hadrons there are less high-energy photons, though the distribution also shifts towards smaller angles.

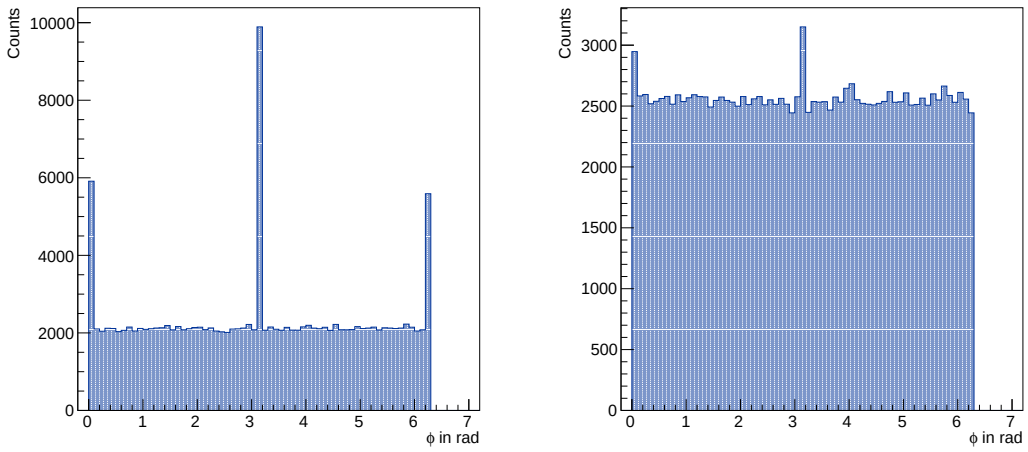

Figure 4.8: ϕ of photons (left) and hadrons (right) for a GEANT4 simulation of $2.5 \cdot 10^9$ electrons on target.

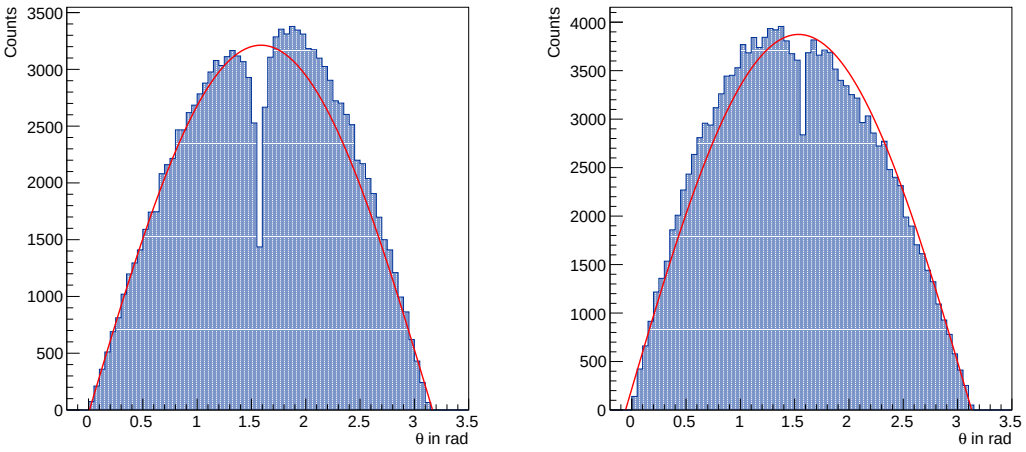

Figure 4.9: θ of photons (left) and hadrons (right) for a GEANT4 simulation of $2.5 \cdot 10^9$ electrons on target. In red an additional sine fit is applied.

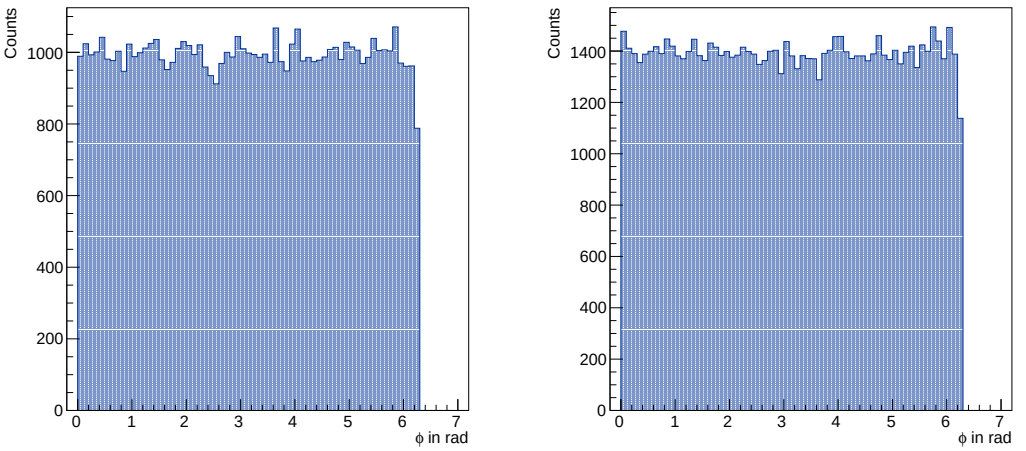

Figure 4.10: ϕ of photons (left) and hadrons (right) with $p_z \neq 0$ for a GEANT4 simulation of $2.5 \cdot 10^9$ electrons on target.

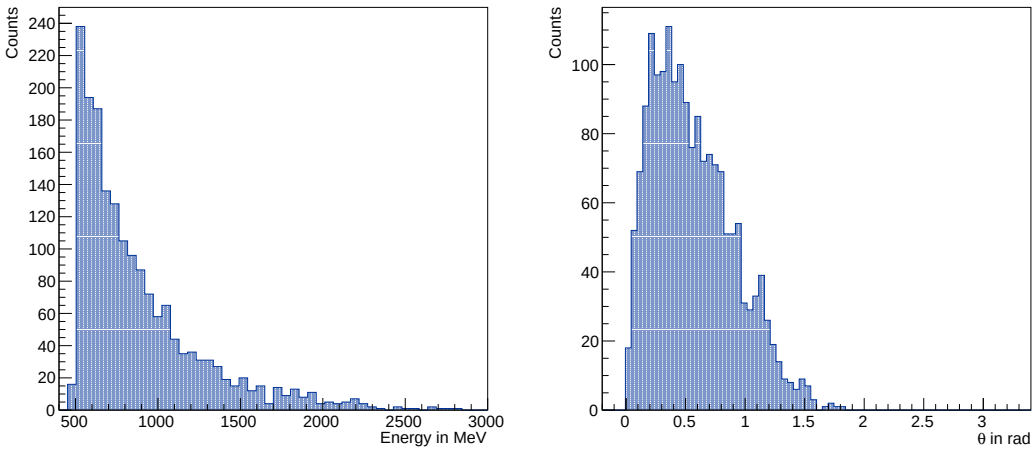

Figure 4.11: Kinetic energy (left) and θ of hadrons (right) with applied energy cut $E_{\mathrm{kin}} \geq 500\,\mathrm{MeV}$ for a GEANT4 simulation of $2.5 \cdot 10^9$ electrons on target.

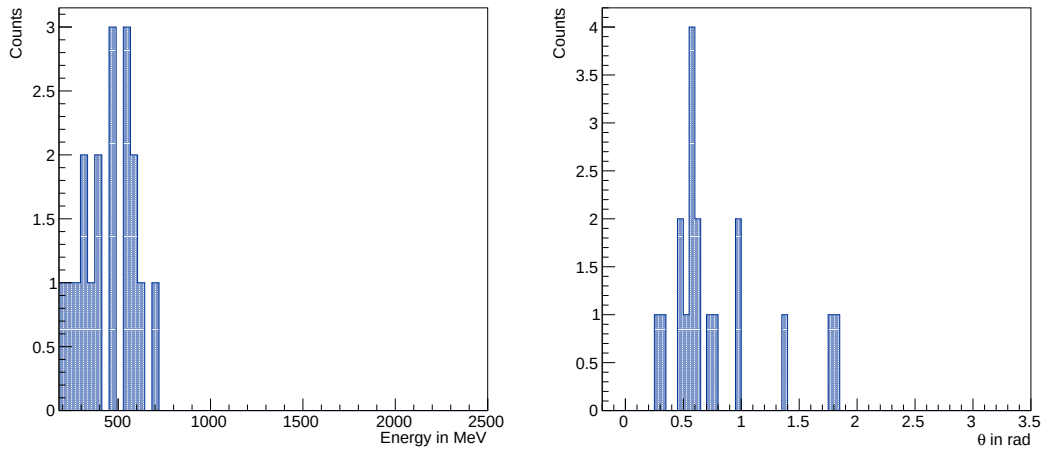

Figure 4.12: Kinetic energy (left) and θ of photons (right) with applied energy cut $E_{\mathrm{kin}} \geq 200\,\mathrm{MeV}$ for a GEANT4 simulation of $2.5 \cdot 10^9$ electrons on target.

4.4 Electro- vs. Photo-Nuclear Interactions

As explained in section 3.3, the overall largest background for LOHENGRIN are QED interactions with out of acceptance high-energy photons, for example photons produced via hard bremsstrahlung of the electron in the target or also tracker material. In most cases the hard bremsstrahlung itself does not pose a problem to the sensitivity of the experiment, as the photon will most likely be detected in the ECal, it might happen that a photon undergoes a photo-nuclear interaction in the target, trackers or the ECal and the outgoing particles remain undetected. Although the trackers will be much thinner than the target, and photo-nuclear interactions of secondary photons will be rare, it is still of interest to investigate the overall distributions of secondary particles from photo-nuclear interactions.

As an extreme case the photon will be directed onto the target and the photo-nuclear interactions of the photon in the target will be studied. Similarly to before, a 3.2 GeV photon beam is therefore directed onto the center of the target. In reality one would have to account for the bremsstrahlung beforehand and thus analyse the impact of photons from the energy spectrum of the SM QED process, which will most likely be less than 3.2 GeV. For now the most pessimistic case - so maximum amount of energy - is chosen, as the angular distributions of the secondary particles are of interest. Further studies regarding the impact of photo-nuclear interactions in the detector setup should be done in the future.

The photo-nuclear interactions will be compared to the electro-nuclear interactions in the following and thus events that have been simulated with the electron beam and contain electro-nuclear interactions will be called EN and events simulated with a photon beam containing photo-nuclear interactions will be called PN. For each scenario only final state particles that have undergone the respective interaction are analysed.

To save computation time in these exhaustive simulations, a custom physics list has been implemented. This custom physics list only allows for electro-nuclear and photo-nuclear interactions via `G4EmExtraPhysics` and hadronic decays via `G4DecayPhysics`. This way the processes of interest are isolated to study only such events and save computation time, while reaching a large number of statistics. Additionally an enhancement factor for the electro- or photo-nuclear cross section has been implemented. The enhancement factor is simply multiplied to the respective cross section, to make the interaction more likely and thus generate more electro- or photo-nuclear events, see section A.1 in the appendix for more details. If an enhancement factor is used, it will be given in the caption of each figure in the form EF_{xy}, where xy stands for either EN or PN depending on the process at hand.

In figure 4.13 the secondary photon energies for photo- and electro-nuclear interactions are presented. Both photo- and electro-nuclear interactions have most secondary photons at energies below 100 MeV. Only few secondary photons obtain energies above that threshold in both simulations. The similarity in distributions also hold for the θ and ϕ distributions of secondary photons, see figures 4.14 and 4.15, which are isotropic for both simulations. One very obvious observation in the histograms is the missing dent and artifacts in the angular distributions in comparison to the results in the previous section. In this simulation only the electromagnetic interactions (`G4EmExtraPhysics`) and hadronic decays (`G4DecayPhysics`) are included, which do not cause the artifacts observed previously. Overall there are more secondary photons produced during photo-nuclear interactions, compared to the electro-nuclear interactions.

Figure 4.16 shows the kinetic energy distributions of secondary hadrons for the electro- and photo-nuclear processes. The energies of secondary hadrons of the respective processes are distributed similarly, with most hadrons obtaining only a small amount of kinetic energy. The angular distributions

of secondary hadrons are given in figure 4.17 and 4.18. The angle θ is distributed isotropically with a slight shift towards smaller angles for electro-nuclear interactions and has a more distinctive shift towards smaller angles for the photo-nuclear process. The ϕ distributions are both isotropic, as expected. As already observed for the photons, there are more secondary hadrons produced in photo-nuclear interactions at 3.2 GeV, compared to the electro-nuclear interactions at the same energy of incident electrons. Since the two processes are closely related by the virtual photon exchange during an electro-nuclear interaction, this difference in statistics is expected. The photo-nuclear process at 3.2 GeV corresponds to an electro-nuclear interaction, where the incident electron looses all of its initial energy to the virtual photon. Therefore a photo-nuclear interaction corresponds to the first bin in figure 4.5, discussed in the previous section. For the electro-nuclear events with such large energy transfers the number of encountered hadrons varied from 0 up to 70. Thus photo-nuclear interactions at an energy of 3.2 GeV are expected to have more secondary particles, as they are an extreme case of the electro-nuclear interactions discussed in the previous section.

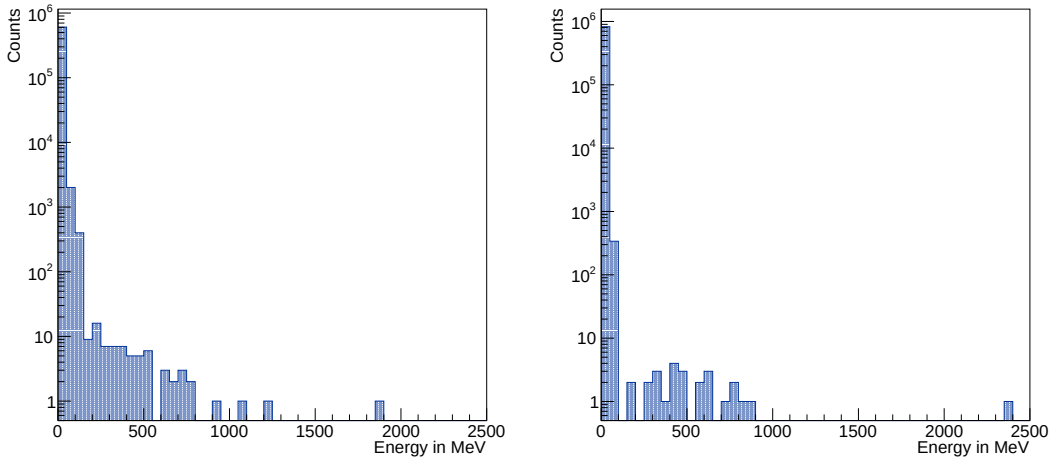

Figure 4.13: Kinetic energy of secondary photons with logarithmic scale for an electron beam with $EF_{EN} = 10^3, EF_{PN} = 1$ (left) and a photon beam with $EF_{EN} = 1, EF_{PN} = 10^3$ (right). For both cases 10^7 beam particles on target are simulated.

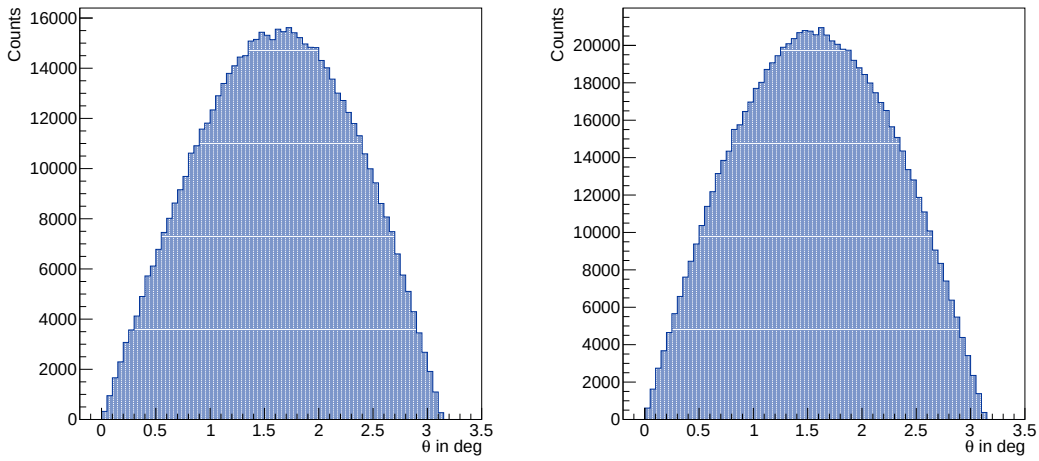

Figure 4.14: θ of secondary photons for an electron beam with $EF_{EN} = 10^3, EF_{PN} = 1$ (left) and a photon beam with $EF_{EN} = 1, EF_{PN} = 10^3$ (right). For both cases 10^7 beam particles on target are simulated.

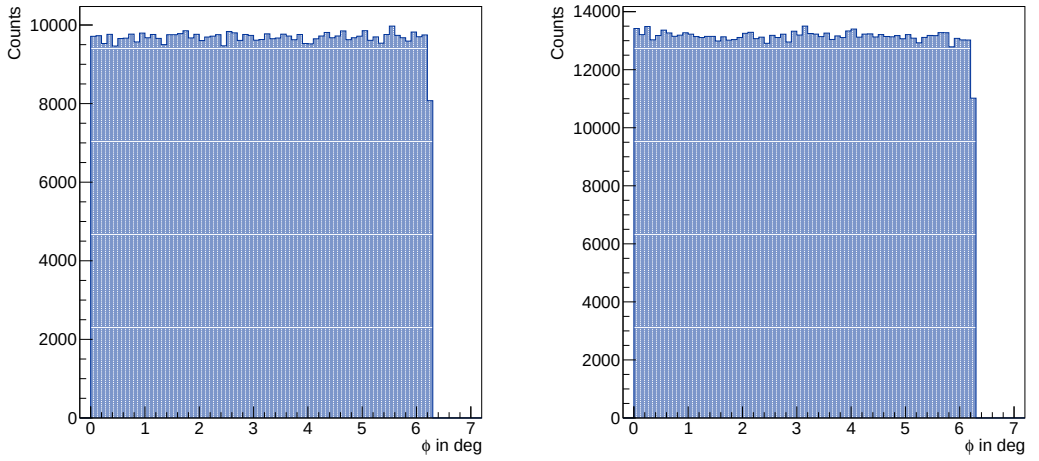

Figure 4.15: ϕ of secondary photons for an electron beam with $EF_{EN} = 10^4, EF_{PN} = 1$ (left) and a photon beam with $EF_{EN} = 1, EF_{PN} = 10^3$ (right). For both cases 10^7 beam particles on target are simulated.

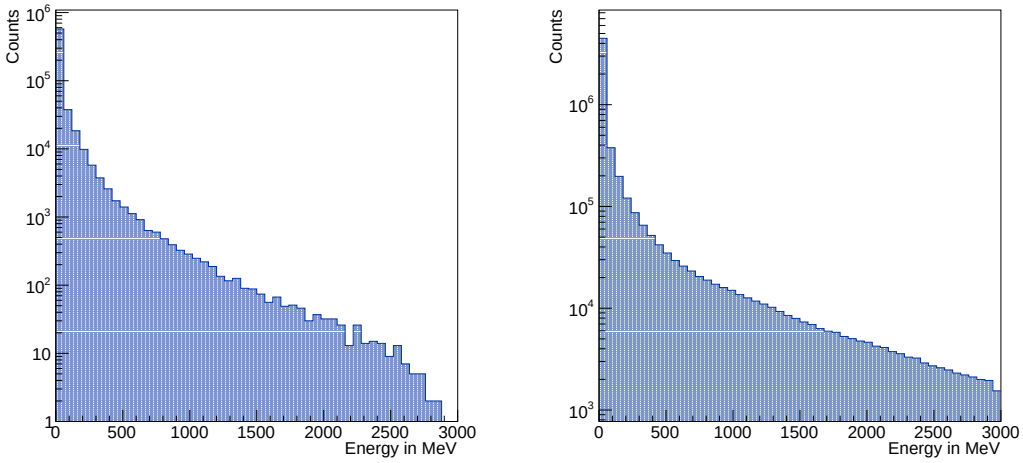

Figure 4.16: Kinetic energy of secondary hadrons for an electron beam with $EF_{EN} = 10^3, EF_{PN} = 1$ (left) and a photon beam with $EF_{EN} = 1, EF_{PN} = 10^3$ (right). For both cases 10^7 beam particles on target are simulated.

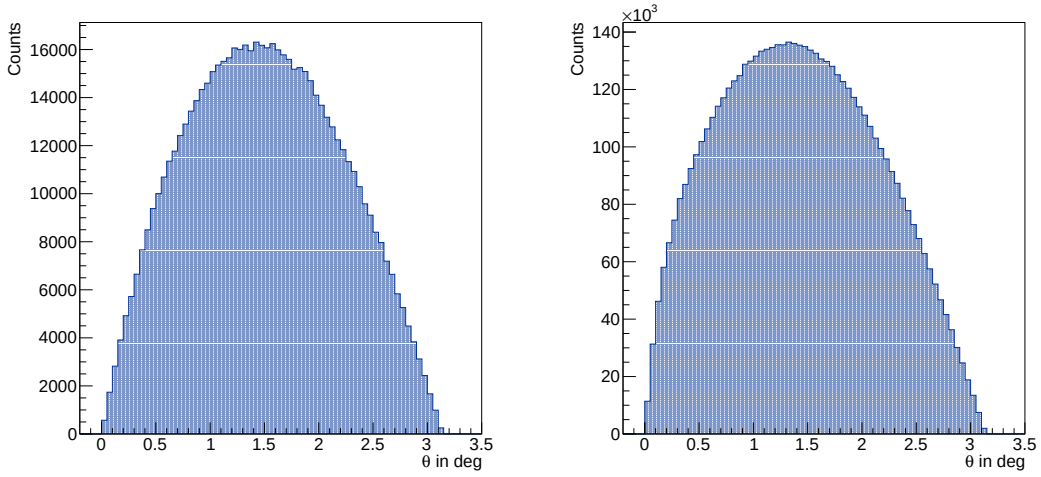

Figure 4.17: θ of secondary hadrons for an electron beam with $EF_{EN} = 10^3, EF_{PN} = 1$ (left) and a photon beam with $EF_{EN} = 1, EF_{PN} = 10^3$ (right). For both cases 10^7 beam particles on target are simulated.

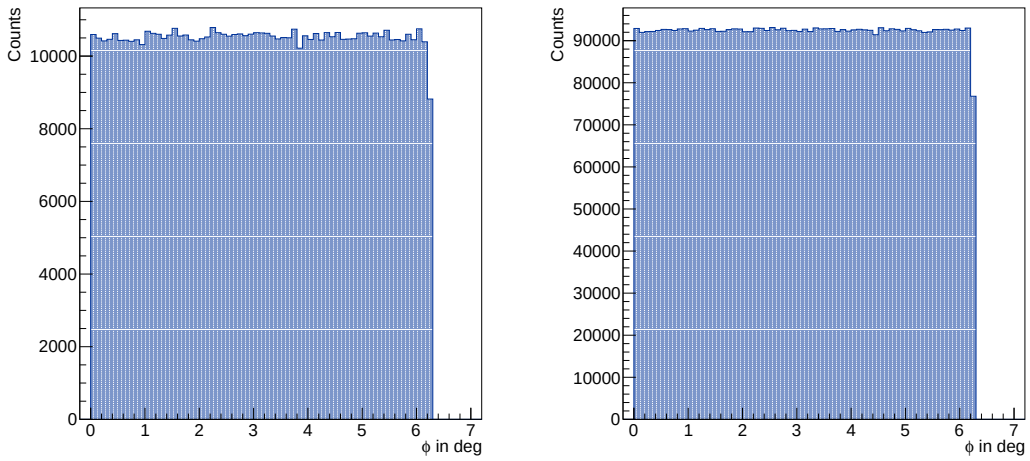

Figure 4.18: ϕ of secondary hadrons for an electron beam with $EF_{EN} = 10^3, EF_{PN} = 1$ (left) and a photon beam with $EF_{EN} = 1, EF_{PN} = 10^3$ (right). For both cases 10^7 beam particles on target are simulated.

It becomes apparent in all figures that the distributions for the individual variables are very similar between the electro- and photo-nuclear interactions. Since the overall distributions are important to study the impact of photo-nuclear interactions to the experiment, the experiment should be able to veto events with photo-nuclear interactions of hard bremsstrahlungs photons the same way as electro-nuclear background events. This is to be expected, due to the processes themselves being closely related. More studies should be conducted concerning the ability to veto backgrounds from photo-nuclear interactions, especially regarding the full detector setup and the impact of hadronic backgrounds being produced in other sensitive materials in the detector setup. Of course the impact of photo-nuclear interactions at lower energies should also be studied in more detail, as the photons emerge from SM bremsstrahlung and will have less than 3.2 GeV.

4.5 Summary

In this chapter electro-nuclear interactions as background for the LOHENGRIN experiment were investigated using the simulation framework GEANT4 as an event generator. After fixing some apparent bugs in GEANT4, the kinematics of individual events were analysed and it became apparent that GEANT4 does not reliably simulate electro-nuclear interactions in the signal region of the LOHENGRIN experiment. Recoiling electrons in the signal region obtain values of $\theta = 0$ rad for recoiling electron energies below ≈ 183 MeV. Due to the unreliability of GEANT4 in the signal region, an alternative event generator will be introduced in the next chapter.

The secondary particles of electro-nuclear interactions were analysed to get an understanding of the energy and angular distributions in GEANT4. From these distributions it became apparent that most of the secondary particles from electro-nuclear interactions obtain energies below 100 MeV and are isotropically distributed. Only high-energy secondary photons and hadrons are boosted in forward direction and thus obtain smaller angles. If each event contains at least one high-energy hadron or photon that deposits energy in the forward calorimeters, such that the event can be vetoed, then the current veto

strategy can remain. However, if there is a significant amount of events without a hadron or photon that produce a measurable signal in the calorimeters, then the veto strategy needs to be adapted.

In the last section of this chapter the electro-nuclear interactions in GEANT4 were compared to photo-nuclear interactions. Overall the distributions for secondary particles from photo- and electro-nuclear interactions are similar, with mainly statistical fluctuations. The main difference is that there are more secondary hadrons and photons produced during photo-nuclear interactions and there are more high-energy secondaries. The overall veto-strategies for photo- and electro-nuclear interactions should therefore be similar as well. Further studies on this should be conducted in the future with a full detector simulation, to investigate the impact of photo-nuclear interactions in other detector materials in the setup.

CHAPTER 5

FLUKA event generator for LOHENGRIN

During the simulations of electro-nuclear interactions with GEANT4, it quickly became clear that it is not well suited and reliable in the signal region of the LOHENGRIN experiment. Consequently, the search for an alternative event generator was pursued, one of which is FLUKA.

In this chapter the simulation framework FLUKA will be used as an event generator for electro-nuclear interactions to investigate and further strengthen the understanding of such processes at the LOHENGRIN experiment and study the impact on the current detector setup.

FLUKA is also a Monte Carlo based simulation framework for particle transport and interactions with matter and will be tested as an alternative event generator for electro-nuclear events particularly in the signal region of the LOHENGRIN experiment. There are various applications of FLUKA, such as radiation protection, medical physics, detector design and accelerator physics. FLUKA is able to simulate the interaction and propagation of photons and electrons in matter, with energies from 100 eV to thousands of TeV and hadrons can be simulated with energies from thermal energies for neutrons up to 20 TeV. In the scope of this thesis version 4-4.1 of FLUKA is used, downloaded July 2024. [66, 67]

Electro-nuclear interactions are implemented in FLUKA in a broad energy range from MeV to TeV [68]. The model to simulate electro-nuclear interactions in FLUKA is the so-called EMD (electromagnetic dissociation), which uses the basic equivalent photon approximation to create the virtual photon for high-energy incident electrons. However, it is a more extensive model with corrections for small energy transfers, where the EPA does not suffice. [69]

In figure 5.1 the electro-nuclear cross section simulated with FLUKA and compared to real data for ^{181}Ta(e^-, n)^{180}Ta can be viewed. The red dots correspond to the basic EPA approach and the blue line corresponds to the current version of the simulation framework with the EMD model [69]. The figure serves as a proof of principle for the accuracy of the FLUKA simulations, as one can see that the current state of the simulation framework indeed describes the data to high precision. Though the total cross section is described well by the implemented model in FLUKA, it is no proof of how accurate the differential cross section is described and how precise the kinematics of electro-nuclear processes are defined in the model. Especially important for the application at hand is the ability to reliably handle events with recoiling electron energies below 75 MeV, which is possible with FLUKA [63, 70].

In addition the yield of neutrons per incident electron against the electron energy is provided in figure 5.2 for electro-nuclear interactions. The FLUKA simulations are compared to experimental data and describe the data with high precision. From the yield of neutrons the kinematics of the electro-nuclear interaction can be assessed, which seem to be described well. [71]

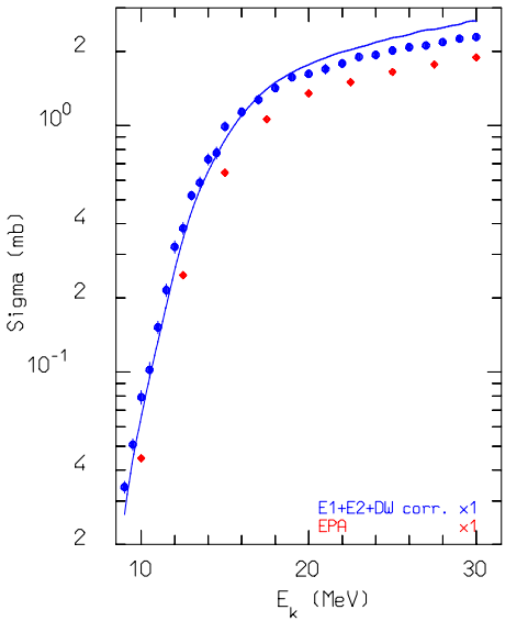

Figure 5.1: Electro-nuclear cross section for ^{181}Ta$(e^-, n)^{180}$Ta against the energy of the electron. The blue data points correspond to data taken from [72], the blue line is the current state of FLUKA and the red dots correspond to the basic EPA approach. Taken from [69].

In the following chapter electro-nuclear interactions in FLUKA will be discussed. First the implemented geometry will be explained in section 5.1 and a short effort towards the visualisation of electro-nuclear events in FLUKA will be made to further strengthen the understanding of the processes at hand, see section 5.2. The results of electro-nuclear interactions in FLUKA will be presented and discussed in section 5.3. In section 5.4 the impact of the composition of the target will be studied. To do so the impact of the fermionic isotope in the tungsten target will be investigated, as well as impurities of the target. Finally, in section 5.6, an event selection will be applied to the Monte Carlo results to get a rough estimate of hadronic backgrounds in the signal region of the LOHENGRIN experiment.

5.1 Geometry setup

The geometry setup in FLUKA works similar to GEANT4: first a so-called "black body" is defined, into which a "void sphere" is placed. Particles outside the void sphere are not propagated further. Inside the void sphere detector components can be placed. Since FLUKA is used as an event generator, a small black body and void sphere, filled with vacuum, suffice. The target can be placed inside the void and the beam can start directly in front of the target. This way the events are simulated by FLUKA and all outgoing particles can be analysed or later placed into a detector simulation. For a chosen number of primary electrons, all secondary particles from inelastic electro-nuclear interactions are recorded in a `.dat` file. The type of information to be saved can be defined by the user. In the present case all secondary energies, momenta, positions and particle types are collected on event basis, as well as the respective information on the incoming electron and the recoiling nucleus. This data can then be analysed using an analysis

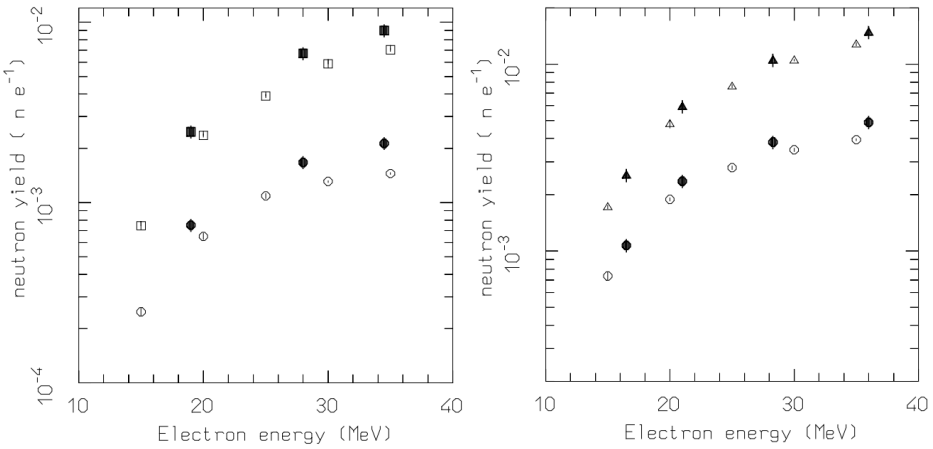

Figure 5.2: Neutron yield per incident electron energy against the initial electron energy for FLUKA simulations (open symbols) and data (closed symbols) with a lead (left) and an iron target (right). The upper point correspond to a target thickness of $5.93 \cdot X_0$ (Pb) and $3.46 \cdot X_0$ (U) and the lower points correspond to $1.01 \cdot X_0$ (Pb) and $1.14 \cdot X_0$ (U). Taken from [71].

framework of choice. Particles in FLUKA are not categorized by PDG identification numbers, but the framework has its own numbering scheme for particles. In table 5.1 the particle numbers for different particles in FLUKA and their corresponding PDG particle number are given, in order to translate between the FLUKA numbering scheme and the PDG numbers. All of the particles given in the table are observed during the electro-nuclear interactions in FLUKA. [73]

The chosen black body dimensions are

- $(28\,\text{cm} \times 28\,\text{cm})$ in x and y directions,
- $(2\,\text{cm} \times 2\,\text{cm})$ in z direction,

the void extends from

- $(27\,\text{cm} \times 27\,\text{cm})$ in x and y directions,
- $(1\,\text{cm} \times 1\,\text{cm})$ in z direction,

and the target has the dimensions

- $(13\,\text{cm} \times 13\,\text{cm})$ in x and y directions, and
- $0.03504\,\text{cm}$ in z direction.

Each component is centered around $(0, 0, 0)$ in all directions. The beam starts at $z_0 = -0.1\,\text{cm}$, also centered in the xy-plane and has an energy of $3.2\,\text{GeV}$. The target material is the bosonic tungsten isotope ^{184}W, similar to the simulations in GEANT4.

In the following the MC truth distributions of the observables, such as energy and angles of the recoiling electron and secondary photons and hadrons will be analysed. A more thorough analysis of the events will be done. It is important to note that momentum and energy are conserved to floating point precision for electro-nuclear events in FLUKA. The corresponding figures can be found in the appendix A.2.

Table 5.1: Tabulated particle numbers in FLUKA with corresponding PDG particle number. Sorted by FLUKA particle numbers. [74] [75]

Particle	Symbol	PDG number	FLUKA number
proton	p	2212	1
anti proton	$\bar{p}$	-2212	2
electron	e^-	11	3
photon	γ	22	7
neutron	n	2112	8
anti neutron	$\bar{n}$	-2112	9
muon +	μ^+	-13	10
muon -	μ^-	13	11
kaon long	K_L^0	130	12
pion +	π^+	211	13
pion -	π^-	-211	14
kaon +	K^+	321	15
kaon -	K^-	-321	16
lambda	Λ	3122	17
anti lambda	$\bar{\Lambda}$	-3122	18
kaon zero short	K_S^0	310	19
sigma -	Σ^-	3112	20
sigma +	Σ^+	3222	21
sigma zero	Σ^0	3212	22
pion zero	π^0	111	23
kaon zero	K^0	311	24
anti kaon zero	$\bar{K}^0$	-311	25
anti sigma -	$\bar{\Sigma}^-$	-3222	31
anti sigma zero	$\bar{\Sigma}^0$	-3212	32
anti sigma +	$\bar{\Sigma}^+$	-3112	33
xi zero	Ξ^0	3322	34
anti xi zero	$\bar{\Xi}^0$	-3322	35
xi -	$\bar{\Xi}^-$	3312	36
xi +	$\bar{\Xi}^+$	-3312	37

5.2 Event visualization

To get an understanding of electro-nuclear events in FLUKA on a more fundamental level, multiple, randomly chosen events are visualized in three dimensions. In figure 5.3, two example events with all encountered secondary particles are presented, to visualize how many and what types of particles are emerging the target per event. For both events the complete set of momentum vectors is given on the left and a zoomed-in version is provided on the right. The momentum vectors all originate from the center of the coordinate system, even though the interaction took place in the area around the origin in the target. For a qualitative discussion this is sufficient. In table 5.2 the colour coding for each particle is given. Notice that this is only a small excerpt of all events and also other hadrons are encountered in the electro-nuclear events, that are not drawn here. In the first event (on the top) most of the energy is divided between two π^0 (1 GeV and 600 MeV) and a neutron (170 MeV), while the rest of the energy is spread over nucleons, a π^- and very low-energetic $O(1\,\text{MeV})$ neutrons and photons. The second event (on the bottom) has most of the energy spread over a photon (2.5 GeV) and a neutron (500 MeV). The

Table 5.2: Tabulated encountered particles in FLUKA simulation with corresponding colour used in the visualisation.

Particle	Symbol	Colour
proton	p	blue
electron	e^-	red
photon	γ	green
neutron	n	cyan
neutral pions	π^0	magenta
charged pions	$\pi^\pm$	yellow
kaon +	K^+	orange
lambda	Λ	black

rest of the energy is distributed again over low-energetic nucleons and photons.

Some more visualised events are provided in figure 5.4. In these events only particles with energies above 50 MeV are drawn and the number of particles per event is drastically reduced, which corresponds to the understanding of electro-nuclear interactions this far. All events have in common that the majority of the transferred energy $O(100 \text{ to } 1\,000\,\text{MeV})$ is obtained by only two to three particles and the rest of the particles obtain only a small amount of energy $< 100\,\text{MeV}$.

The isotropic distribution of electro-nuclear secondaries becomes especially apparent in the first figure without the applied energy cut, whereas the events with the applied energy cut have more forward directed particles. However, even with the applied energy cut the events have high-energy particles emerging the target at a large angle, which is not well covered by the current veto strategy and will be investigated in more detail in the following.

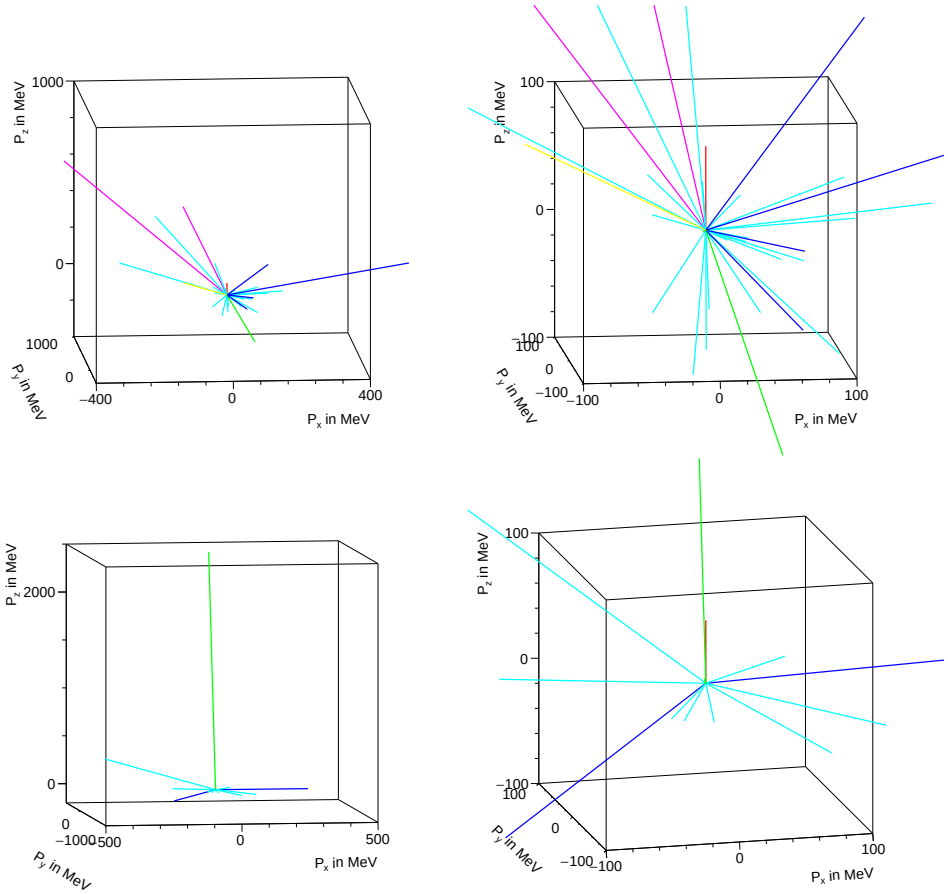

Figure 5.3: Exemplary event $e^- + {}^{184}\mathrm{W} \rightarrow e^- + {}^{157}\mathrm{Er} + 2\pi^0 + 22n + 5p + \pi^- + 6\gamma$ (top) and $e^- + {}^{184}\mathrm{W} \rightarrow e^- + {}^{157}\mathrm{Er} + 8n + 2p + 8\gamma$ (bottom) with all encountered secondary particles from a $2.5 \cdot 10^{12}$ e.o.t. FLUKA simulation (left) and zoomed in (right). The colour coding is given in table 5.2.

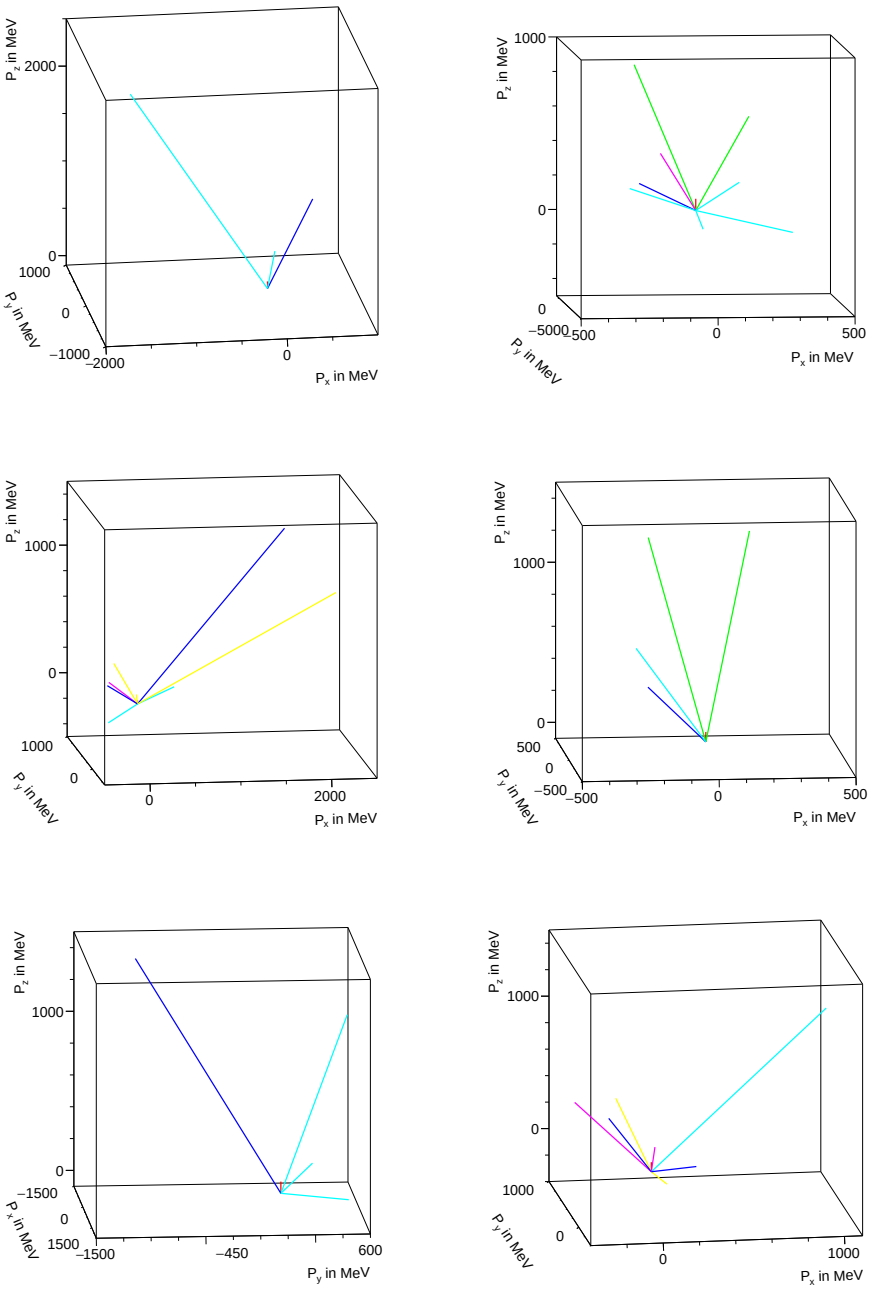

Figure 5.4: Visualized events from a $2.5 \cdot 10^{12}$ e.o.t. FLUKA simulation. The colour coding is given in table 5.2. Only particles with energies above 50 MeV are drawn.

5.3 FLUKA output

In FLUKA $2.5 \cdot 10^9$ e.o.t. are simulated to quantify the observed events from the previous section. Roughly $8 \cdot 10^4$ out of the $2.5 \cdot 10^9$ events are electro-nuclear interactions in the target and the rest are other processes like elastic scattering of the electron or SM QED interactions. In figure 5.5 the distributions of the kinetic energy and angle θ of the recoil electron are presented. They look similar to the distributions observed in GEANT4. It is clearly visible that recoil energies below 100 MeV are possible and FLUKA is able to reliably simulate this region [63, 70]. The angular distribution of the recoiling electrons looks as expected with a distinct peak for angles below 0.1 rad and only a few $O(10)$ electrons with angles above this value.

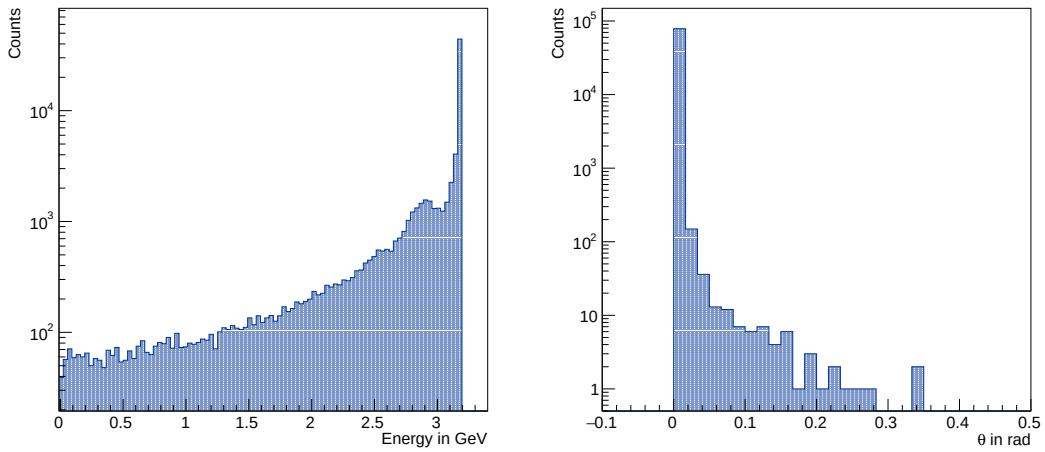

Figure 5.5: Kinetic energy (left) and angle θ (right) of the recoil electron for $2.5 \cdot 10^9$ electrons on target for FLUKA simulation with a logarithmic scales.

Again the number of encountered hadrons per event against the recoiling energy of the electron is analysed, to get an overview of encountered hadrons, see figure 5.6. The overall distribution looks similar to that seen in GEANT4, with one major difference: contrary to the results in GEANT4, the number of hadrons encountered per event is almost always $n_{\text{had}} > 0$. There are only extremely rare events with zero hadrons, which corresponds to the understanding of electro-nuclear interactions, as pure photon dexcitation of the nucleus is supposed to be rare [63, 64]. As mentioned previously: even at small energy transfers to the nucleus, the binding energy of nucleons to the nucleus are exceeded and thus hadrons should be released. The histogram does show an increased probability to have 1-2 hadrons per event, which seems plausible, as in many events the electron only transfers a small amount of energy, making it unlikely to produce more than 2 or 3 secondary hadrons.

Additionally to the recoiling electron, the information on the recoiling nucleus can be acquired in FLUKA. The corresponding histogram can be viewed in figure 5.7. The recoiling nucleus obtains only a small amount of energy from the interaction in the MeV range, as is to be expected.

As for secondary hadrons produced during electro-nuclear interactions, it is also interesting to see what kind of particles are created during electro-nuclear interactions in FLUKA. The secondary FLUKA particles for all encountered secondary particles can be viewed in figure 5.8. Additionally the particle numbers for hadrons with energies above 500 MeV is provided. It becomes apparent that including all

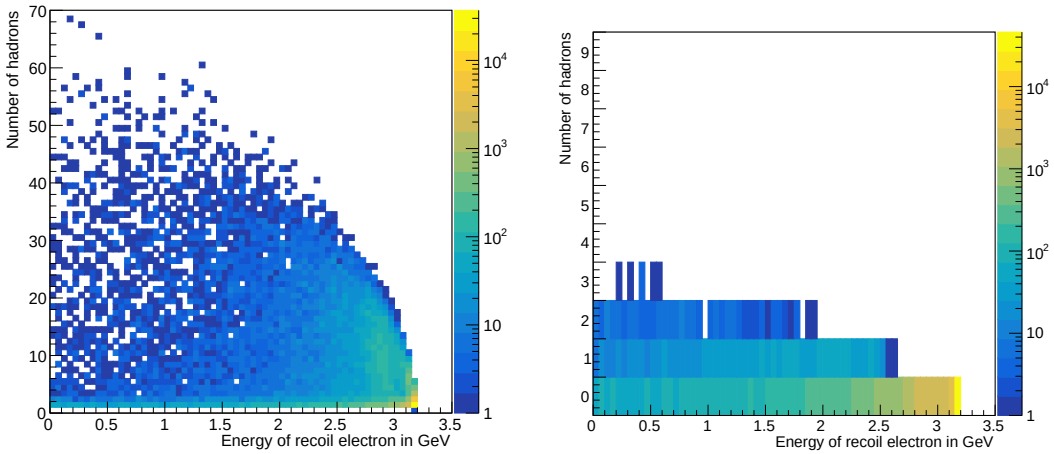

Figure 5.6: Number of encountered hadrons (left) and number of encountered hadrons with more than 500 MeV energy (right) per event against energy of the recoil electron for a FLUKA simulation of $2.5 \cdot 10^9$ e.o.t.

energies, protons (1), neutrons (8) and photons (7) make up the majority of produced secondary particles (excluding the recoiling electrons). But when applying the energy cut for hadrons of 500 MeV, the relative number of neutrons and protons is significantly smaller and pions π^0 (23), $\pi^\pm$ (13,14), kaons K^0 (24), K^+ (15) and sigma Σ^0 (22) gain in relative amount. The overall number of hadrons is significantly smaller $O(10^3)$, proving that most of the outgoing secondary hadrons are low-energetic. This supports the theory, that during an electro-nuclear interaction most of the energy the electron looses is transferred only to a few hadrons, while the neutrons are radiated off during the de-excitation of the remaining nucleus.

As mentioned in the previous chapter, knowing which particles emerge from the electro-nuclear interactions is very important, and the detector design is heavily dependent on it. Though it was suspected that neutral hadrons such as the K^0_L would be the main challenge for the veto efficiency against hadron final states, it turns out that the neutrons and protons pose a much larger problem, as they are radiated off isotropically. But also high-energy hadrons, such as pions and kaons, must be detected with the current veto strategy, to obtain a high background rejection efficiency. The results of the FLUKA simulations regarding the angular distributions of the secondary photons and hadrons will be analysed in the following.

In figure 5.9 the energy distributions for the secondary photons and hadrons of electro-nuclear interactions are given. Most of the secondary photons are low-energetic with energies less than 10 MeV and only a few particles are observed outside of that scope. A similar behaviour can be observed for secondary hadrons, with most of the hadrons having less energy than 100 MeV. However, there are more high-energy hadrons with energies above 1 GeV compared to the photons. If high-energy neutral hadrons obtain angles that exceed the angular coverage of the HCal (0.6 rad) and no other veto strategy applies for the event, then signal-like signatures are left in the detector setup. The angular distributions are given in figures 5.10 and 5.11. As expected these distributions are isotropic, with a slight shift towards smaller angles of θ for secondary hadrons. This can be seen from the slight difference to the sine-function fitted to the histogram data. It is obvious that the low-energy hadrons and photons that are radiated at large angles are impossible to detect with the forward calorimeters in the current detector setup. Additionally

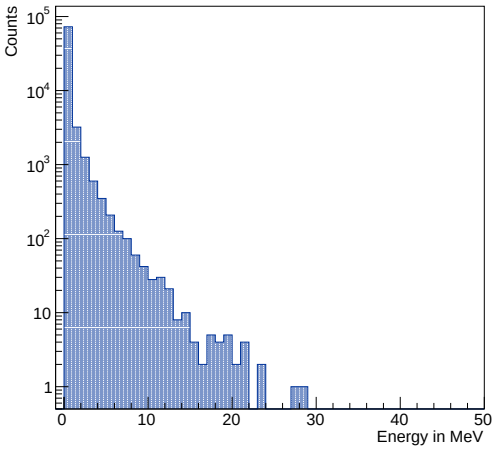

Figure 5.7: Kinetic energy for recoil nucleus for $2.5 \cdot 10^9$ e.o.t. for FLUKA simulation with logarithmic scale.

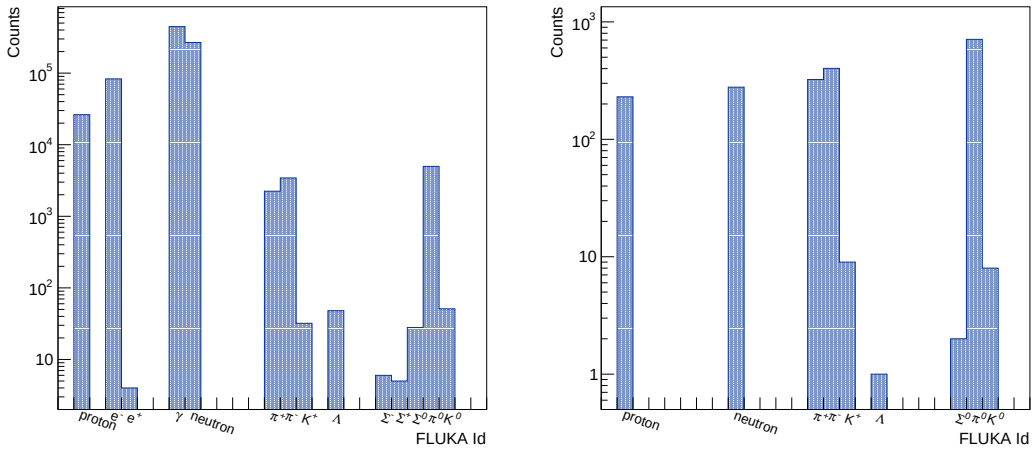

Figure 5.8: Secondary particle numbers for $2.5 \cdot 10^9$ e.o.t. for FLUKA simulation (left) and for hadrons with more than 500 MeV kinetic energy (right) with a logarithmic scale.

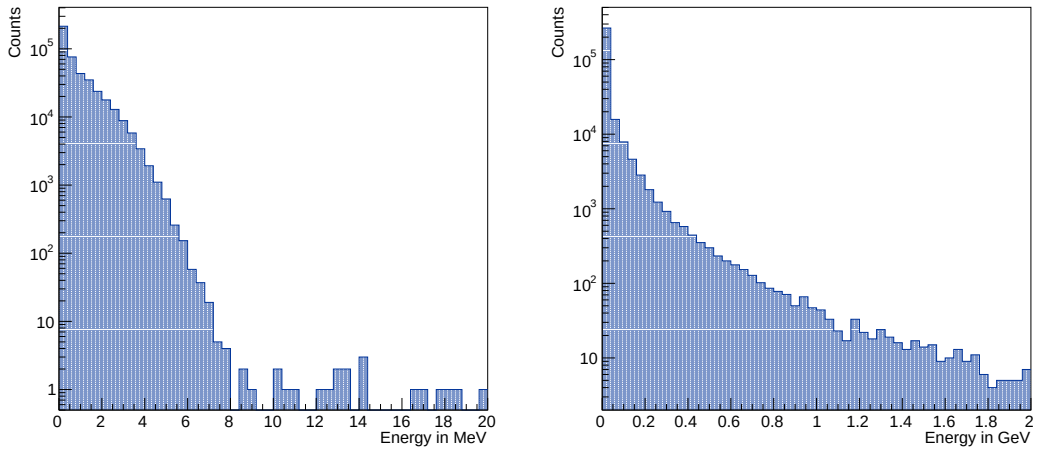

Figure 5.9: Energy of secondary photons (left) and hadrons (right) for $2.5 \cdot 10^9$ e.o.t. for FLUKA simulation with a logarithmic scale.

it is suspected that many of the low-energy particles with larger opening angles than the magnet will be absorbed by the iron bulk. Thus high-energy hadrons emitted in forward direction provide a possibility to veto electro-nuclear events with the current detector design. Therefore it is of interest to look at only the high-energy particles. The cuts are applied similarly to the previous chapter: for the photons the high-energy cut is set to 200 MeV and for hadrons at 500 MeV. The energy distributions for the high-energy secondary particles can be viewed in figure 5.12. For both the photons and hadrons only a small fraction of particles pass the energy cut compared to the total number of particles. This is in accordance with the theoretical expectation, where only a small number of high-energy hadrons and photons are emitted from the electro-nuclear interaction.

The θ distribution in figure 5.13 is shifted towards smaller angles for high-energy secondary photons and hadrons. Thus higher energy particles emerge at smaller angles, which also corresponds to the expectation. Though it is visible from the two histograms that there is a significant amount of high-energy secondaries that obtain large angles outside the scope of the calorimeters.

The correlation between energy and angle θ of secondary hadrons can be visualised to further strengthen the model of electro-nuclear interactions. In figure 5.14 the angles θ of secondary hadrons are plotted against the hadrons energy and the mean of each bin is provided additionally in a separate histogram. Indeed it can be verified that for small energies, the angular distribution of the hadrons is isotropic and the larger the hadron energy, the smaller the obtained angle. While the majority of high-energy hadrons are emitted in forward direction, there is a significant fraction of events with high-energy hadrons emitted at large angles. Together with the small number of high-energy hadrons, this presents a challenge to the current veto strategy of the LOHENGRIN experiment.

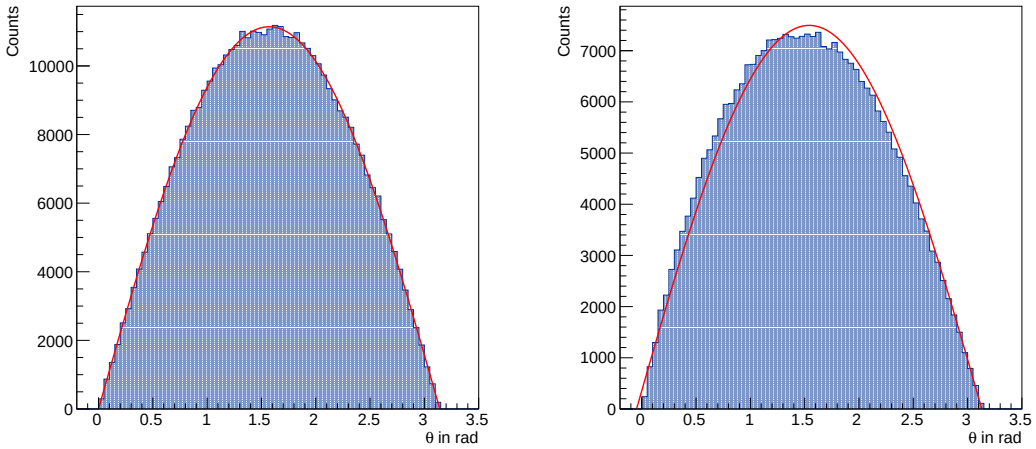

Figure 5.10: θ of the secondary photons (left) and θ of the secondary hadrons (right) for $2.5 \cdot 10^9$ e.o.t. for FLUKA simulation.

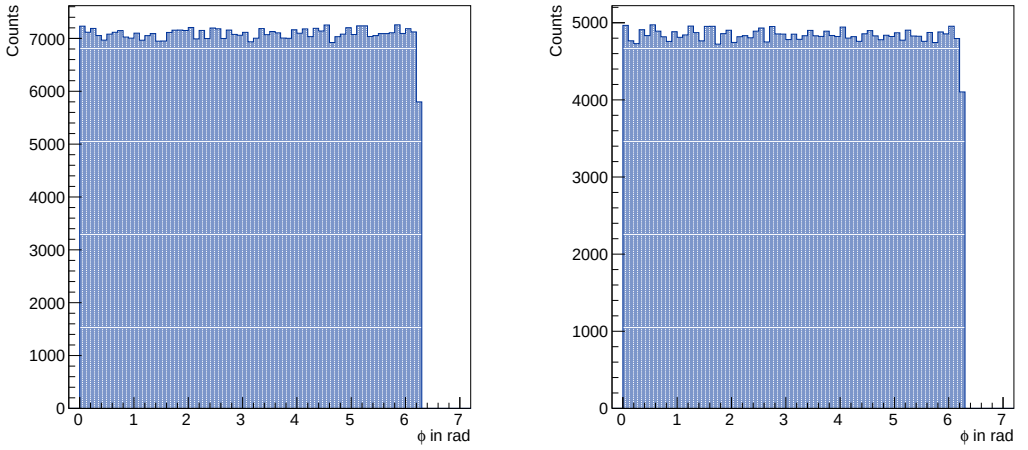

Figure 5.11: Gamma ϕ (left) and hadron ϕ (right) for $2.5 \cdot 10^9$ e.o.t. for FLUKA simulation.

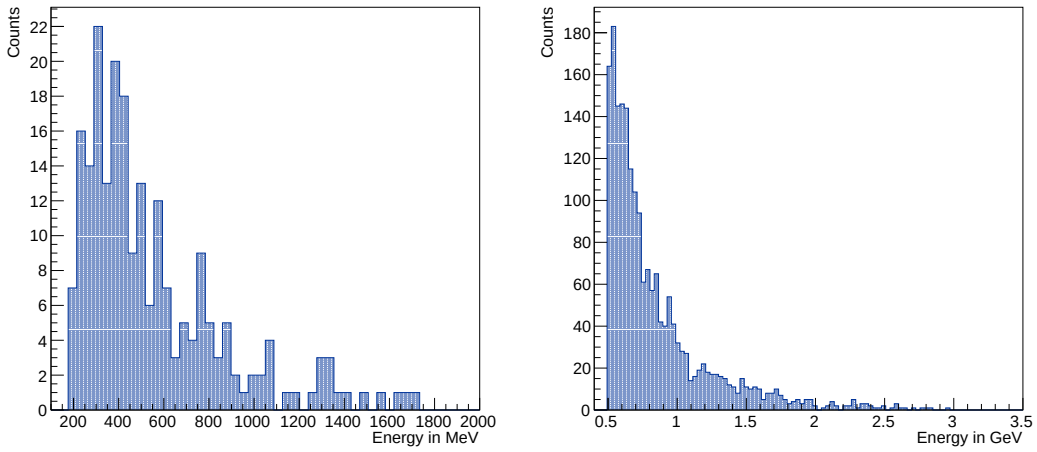

Figure 5.12: Energy distributions for a FLUKA simulation with $2.5 \cdot 10^9$ e.o.t. of photons (left) and hadrons (right) and the respective energy cuts applied.

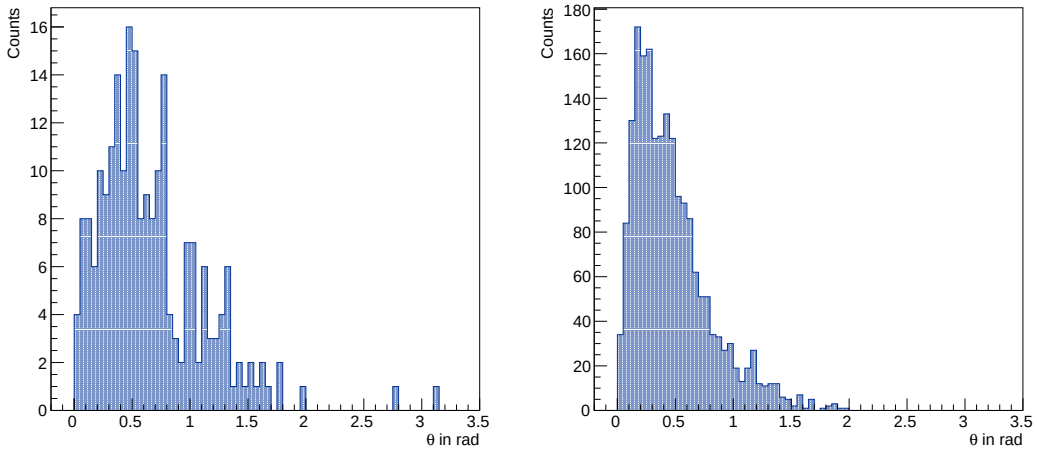

Figure 5.13: θ distributions for a FLUKA simulation with $2.5 \cdot 10^9$ e.o.t. of photons (left) and hadrons (right) and the respective energy cuts applied.

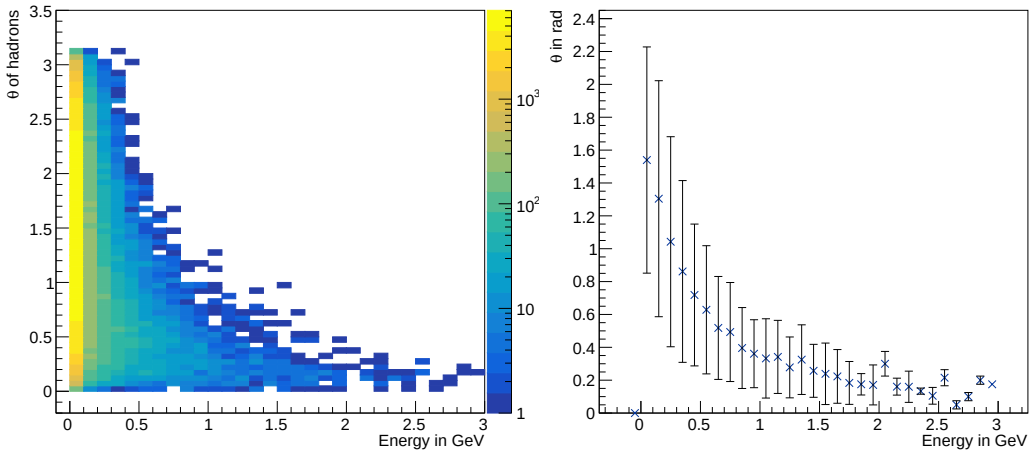

Figure 5.14: θ-energy correlation of hadrons encountered in a FLUKA simulation with $2.5 \cdot 10^9$ e.o.t. (left) and the mean per energy bin with standard deviation (right). If the standard deviation is zero, then there is only one hit in that bin.

5.4 Target composition Study

Before investigating the signal region at LOHENGRIN for the simulated FLUKA data, a short study concerning the target material is conducted. To this point only the scalar isotope ^{184}W of tungsten was used as the material of the target. This has been well motivated in section 3.2 and in more detail in [5]. The impact of the fermionic isotope of tungsten as target material will be analysed in the following section 5.4.1, to further strengthen the assumptions above.

In reality the target will consist of natural tungsten and thus be composed of a mixture of the fermionic and bosonic isotopes. However, the production of such targets for physics experiments is not ideal and impurities are often found in the material. In section 5.4.2 a target with an impurity will be used in the simulation to study the impact on the electro-nuclear interactions.

5.4.1 Fermionic vs. bosonic tungsten

As mentioned in chapter 3, the naturally stable tungsten isotopes are ^{182}W, ^{183}W, ^{184}W and ^{186}W and the physical target will contain a mixture of these isotopes. For simplicity only ^{184}W was taken as target material in the previous studies. All but ^{183}W are bosonic particles with spin 0 and the impact of the fermionic isotope is supposedly low, since it contributes to the cross section with its squared inverse nuclear mass and only makes up 14 % of the natural tungsten [5]. To study and verify the small impact of the fermionic isotope ^{183}W, a target consisting of that isotope only is simulated in FLUKA and the distributions of the secondary particles of electro-nuclear interactions are analysed. To be able to compare the distributions to the previous results using ^{184}W in the target, also $2.5 \cdot 10^9$ e.o.t. are simulated.

In the following the observables for the simulations with ^{183}W and ^{184}W will be compared in ratio plots. Each histogram is scaled by the number of its entries and then the ratio between the two histograms is calculated.

In figure 5.15 the ratio plots for the energy and angle θ of the recoiling electron are presented. The energy distributions of the recoiling electron look similar, particularly in the region with a large amount of statistics. At lower energies there are less statistics due to the rareness of such events and fluctuations are visible in the ratio plot. These fluctuations are of statistical manner and should not impact the result as a whole. The same observations can be made for the angular θ distribution for the recoiling electron: at small angles and large statistics the ratio is ≈ 1 and towards larger angles and in the region with less counts there are fluctuations in the distributions.

The energy and angle θ distributions for secondary photons can be viewed in figure 5.16. The distribution of secondary photon energies has some differences, with a slight tendency of higher energy photons for a target with ^{183}W. Fluctuations are again more visible, where there are less statistics, as is to be expected. The angular distributions for secondary photons have a ratio of ≈ 1 over the full range of θ. The overall distributions for secondary photons are the same up to statistical fluctuations.

The same figures are given in 5.17 for secondary hadrons from electro-nuclear interactions in a target with ^{183}W and ^{184}W. Similarly to the photon spectra, the ratio of the energy distributions for secondary hadrons is ≈ 1 and fluctuates for larger energies, where less statistics are present. The angular distribution for the two target isotopes is also similar over the full range of θ, with small fluctuations towards the edges of the distribution.

For high-energy photons and hadrons the same distributions can be analysed. For photons with energies above 200 MeV the ratio plots are given in figure 5.18. Differences are more difficult to asses due to the loss of statistics for high-energy photons compared to the distribution of photons at all energies. Overall the energies and angles θ are distributed the same, with a slight tendency towards smaller angles for the target composed of ^{183}W. For the high-energy hadrons with energies above 500 MeV the energies and angles θ are given in figure 5.19. The distributions for the two isotopes look the same up to statistical fluctuations.

For the purpose of this thesis the difference between the two tungsten isotopes can be neglected and the assumption that signal modelling with only the fermionic isotope ^{184}W is sufficient could be verified. However, since differences can be observed, this should be kept in mind and investigated in more detail in a future study.

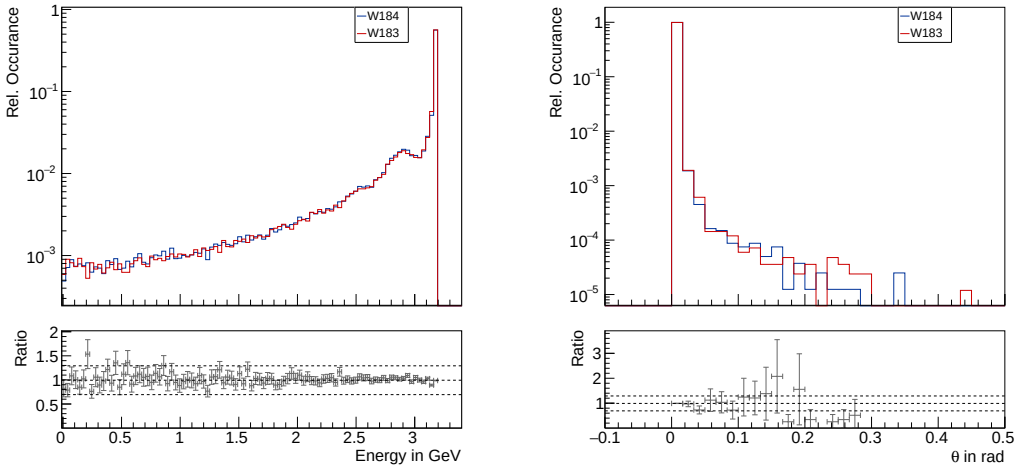

Figure 5.15: Energy (left) and θ (right) of the recoiling electron for a FLUKA simulation with $2.5 \cdot 10^9$ e.o.t. comparing the target material ^{184}W and ^{183}W.

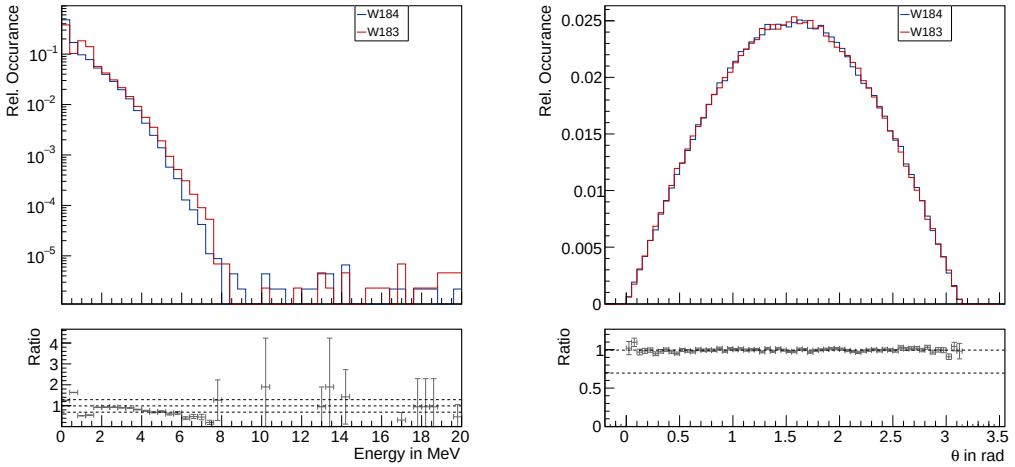

Figure 5.16: Energy (left) and θ (right) of secondary photons for a FLUKA simulation with $2.5 \cdot 10^9$ e.o.t. comparing the target material ^{184}W and ^{183}W.

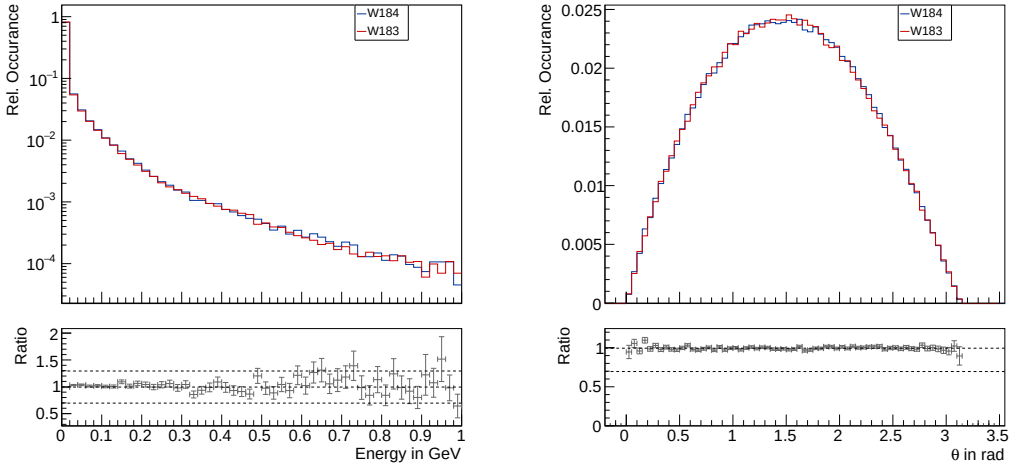

Figure 5.17: Energy (left) and θ (right) of secondary hadrons for a FLUKA simulation with $2.5 \cdot 10^9$ e.o.t. comparing the target material ^{184}W and ^{183}W.

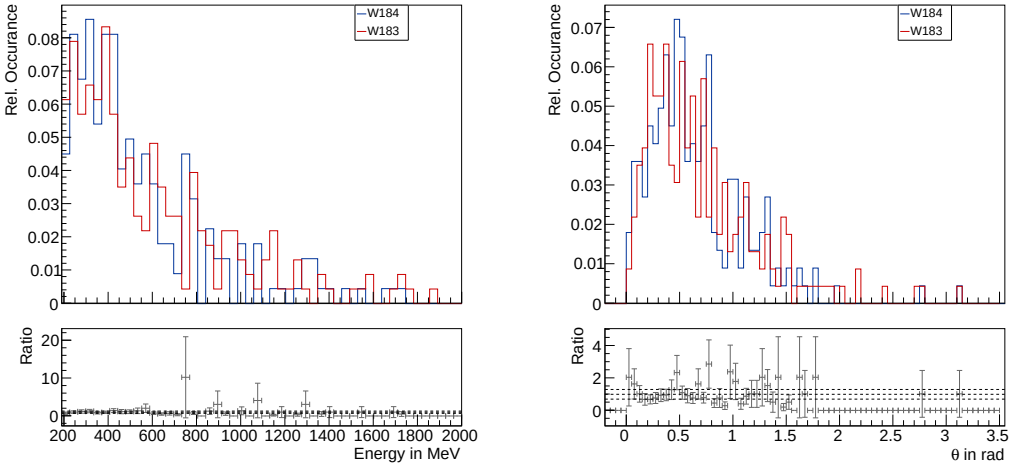

Figure 5.18: Energy (left) and θ (right) of secondary photons with applied energy cut for a FLUKA simulation with $2.5 \cdot 10^9$ e.o.t. comparing the target material ^{184}W and ^{183}W.

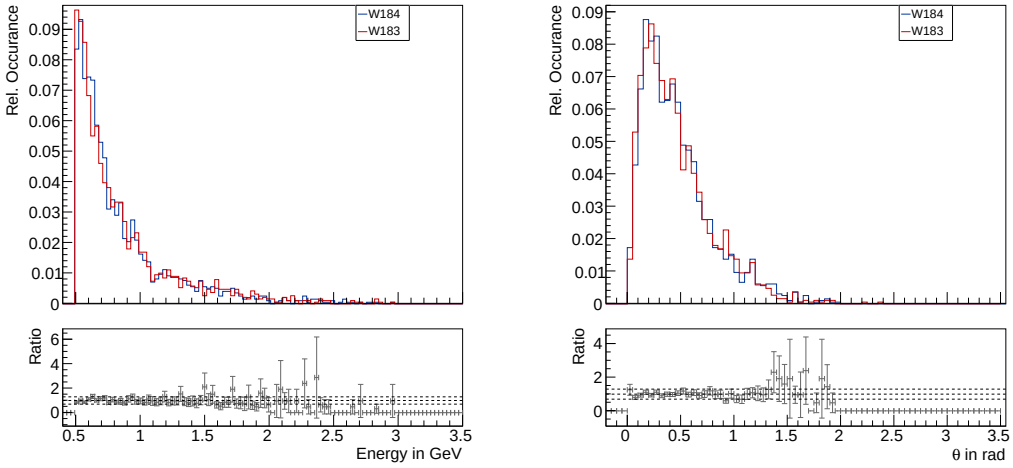

Figure 5.19: Energy (left) and θ (right) of secondary hadrons with applied energy cut for a FLUKA simulation with $2.5 \cdot 10^9$ e.o.t. comparing the target material ^{184}W and ^{183}W.

5.4.2 Impurities in Target

In reality it is impossible to obtain a target purely made up of the bosonic tungsten isotope ^{184}W. Often even pure natural tungsten targets are difficult to produce and the target material might have some impurities. Such impurities could be small amounts of other materials, like e.g. nickel or iron. There are different degrees of impurities, ranging from state-of-the-art productions with as little as 0.001 % for nearly pure tungsten to 0.03 % or even more depending on the price point of the target [76]. To study the impact of more drastic impurities a larger percentage is chosen.

The impact of such impurities of the target is examined with a FLUKA simulation of $2.5 \cdot 10^9$ e.o.t. with a 95 % tungsten target and an impurity of 5 % nickel. In this instance the predefined tungsten and nickel in FLUKA are used, which are defined as

- Tungsten: $A = 183.84$, $Z = 74$, $\rho = 19.3\,\mathrm{g\,cm^3}$
- Nickel: $A = 58.6934$, $Z = 28$, $\rho = 8.902\,\mathrm{g\,cm^3}$,

where A is the nuclear mass number, Z corresponds to the nuclear charge number and ρ is the density. Natural nickel is composed of five isotopes, namely ^{58}Ni (68.077 %), ^{60}Ni (26.223 %), ^{61}Ni (1.1399 %), ^{62}Ni (3.6346 %) and ^{64}Ni (0.9255 %) [77]. All of the natural stable nickel isotopes are scalar and have spin $J^P = 0^+$, except for isotope ^{61}Ni, which has spin $J^P = \frac{3}{2}^-$ [78].

The histograms with the same observables as in the previous section will be discussed in the following. The ratio is again determined after each histogram has been normalized by the number of entries.

Figure 5.20 presents the energy and angle θ distribution of the recoiling electron from electro-nuclear interactions in a tungsten target with impurities compared to the pure ^{184}W target. The distributions overlap for the most part, especially in the regions with large statistics. Fluctuations of the ratio in the regions with lower statistics can be observed and are to be expected.

In figures 5.21 and 5.22 the energy and angular distributions of secondary photons and hadrons at all energies are given. For both secondary photons and hadrons the angular distributions have a ratio of

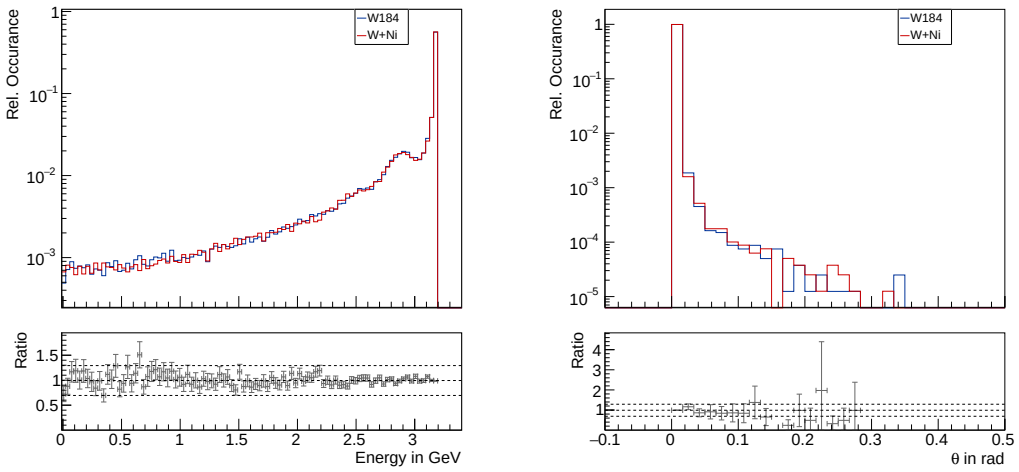

Figure 5.20: Energy (left) and θ (right) of the recoiling electron for a FLUKA simulation with $2.5 \cdot 10^9$ e.o.t. comparing the target material ^{184}W and an impure version.

approximately 1 over the range of the angle θ. At the edges of the distributions small fluctuations can be observed. The ratio of the energy distributions of the secondary photons and hadrons are approximately constant for small energies and fluctuate at higher energies in the region with less statistics. The energy distribution for secondary hadrons remains constant over a larger energy range compared to the photons.

The distributions for high-energy hadrons and photons are presented as well, see figures 5.23 and 5.24. For hadrons the high-energy cut corresponds to 500 MeV and for photons it is at 200 MeV. Similarly to before, the assessment of these distributions is difficult due to the lack of statistics in the energy range of high-energy secondary particles. For secondary high-energy hadrons the ratios are almost constant up to 1 GeV and 1.5 rad and the overall distributions are very similar for the energy and angles θ. Fluctuations are more dominant towards the tails of the distributions, where less counts occur. The distributions for the secondary high-energy photons also have a similar distribution, though they have more fluctuations over the whole spectrum. This is to be expected, since there are less high-energy photons compared to high-energy hadrons.

From the histograms only a small impact on the angular and energy distributions of electro-nuclear secondary particles using an impure target can be observed, which can be explained from statistical fluctuations. Therefore impurities in the target of up to 5 %, do not impact the angular distributions of the secondary particles drastically. If impurities of more than 5 % are present or other material impurities are given, this study can be repeated for arbitrary mixtures and materials.

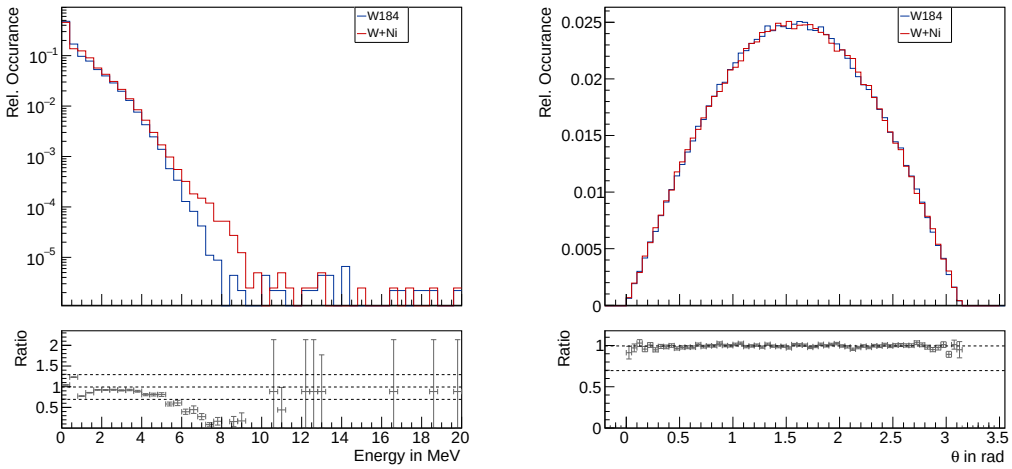

Figure 5.21: Energy (left) and θ (right) of secondary photons for a FLUKA simulation with $2.5 \cdot 10^9$ e.o.t. comparing the target material ^{184}W and an impure version.

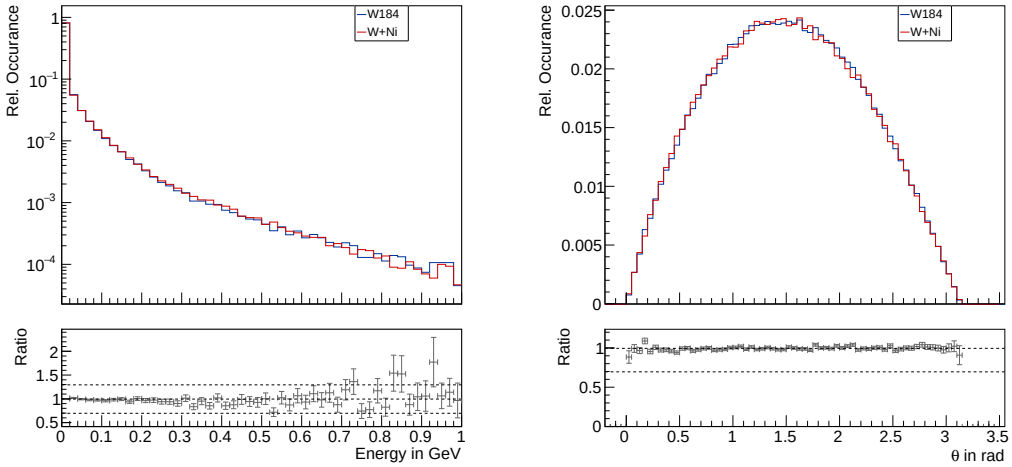

Figure 5.22: Energy (left) and θ (right) of secondary hadrons for a FLUKA simulation with $2.5 \cdot 10^9$ e.o.t. comparing the target material ^{184}W and an impure version.

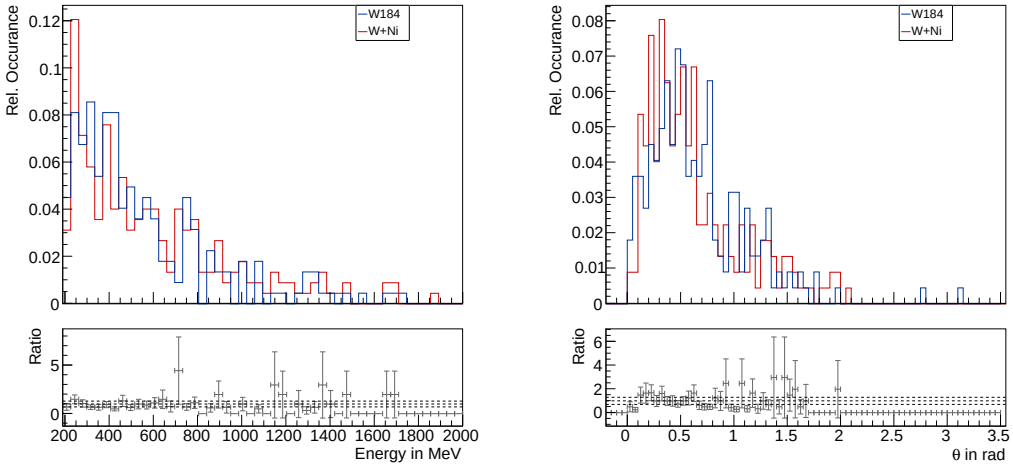

Figure 5.23: Energy (left) and θ (right) of secondary photons with applied energy cut for a FLUKA simulation with $2.5 \cdot 10^9$ e.o.t. comparing the target material ^{184}W and an impure version.

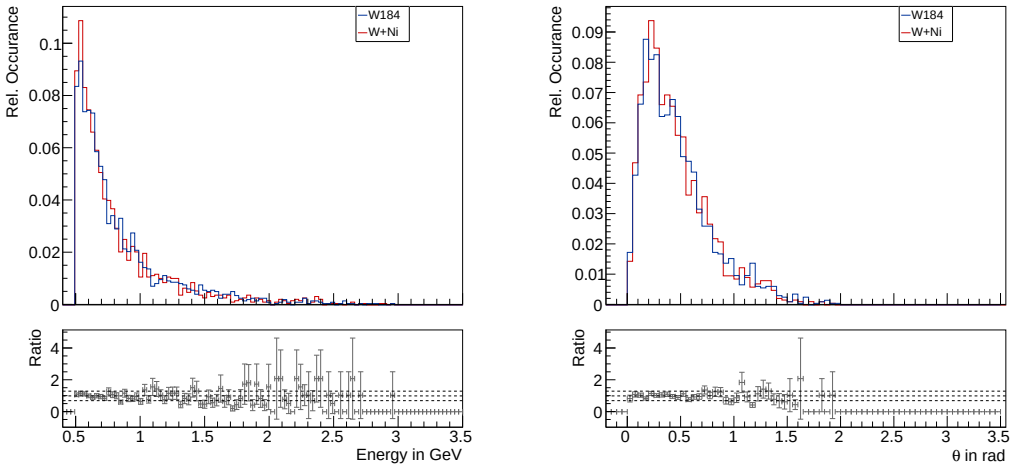

Figure 5.24: Energy (left) and θ (right) of secondary hadrons with applied energy cut for a FLUKA simulation with $2.5 \cdot 10^9$ e.o.t. comparing the target material ^{184}W and an impure version.

5.5 Electro- vs. Photo-Nuclear Interactions

Another important aspect of the experiment are photo-nuclear backgrounds created by secondary photons in sensitive materials in the detector setup. In section 4.4 this has been studied with the simulation framework GEANT4 using a custom physics list. The angular distributions of secondary photons and hadrons from photo-nuclear processes in FLUKA are discussed in the following. For this simulation the tungsten isotope ^{184}W is chosen as target material again and $2.5 \cdot 10^9$ photons are shot at the target with an energy of 3.2 GeV. The comparison to the electro-nuclear interactions of an electron with the target material are given in form of ratio plots in figures 5.25 to 5.29. These figures depict the ratio of the

electro- and photo-nuclear histograms, which are scaled by their respective number of entries before the ratio is calculated. The unscaled ratio plots can be viewed in figures A.8 to A.11.

In figure 5.25 the energy and angle θ for secondary photons are presented. The secondary photon energies are similarly distributed up to approximately 4 MeV, after which the electro-nuclear secondary photon spectrum rapidly falls to zero and the photo-nuclear distribution falls off less steep and rises slowly after 8 MeV. The differences between the two spectra become apparent for larger energies, where many more high-energy photons are produced during photo-nuclear interactions. Here two effects need to be differentiated: one very obvious reason is that during photo-nuclear interactions the photon transfers all of its energy onto the nucleus, whereas in electro-nuclear interactions only a fraction of the electrons energy is transferred to the virtual photon. In electro-nuclear interactions this amount of energy is mostly very small and larger energy transfers get increasingly rare. The photo-nuclear interactions studied here correspond to the extreme case of electro-nuclear processes, where the electron transfers all of its energy onto the virtual photon. In such cases more and much higher-energetic particles are expected. The other effect that needs to be differentiated is the definition of photo-nuclear and electro-nuclear interactions in FLUKA. To analyse electro-nuclear interactions in the simulation framework, a cut on the type of interaction is made via the variable ICODE. For electro-nuclear interactions all secondary particles have to have ICODE== 101. The same is done during the analysis of photo-nuclear interactions, except for a photon as beam particle. However, in FLUKA the ICODE== 101 merely corresponds to all secondary particles from inelastic interactions [73] and for photons this might also contain Compton scattering on the tungsten nucleus, which could explain the visible shoulder after 8 MeV. If the full distribution of secondary photons from photo-nuclear interactions is visualised, then the Compton spectrum becomes visible, see 5.26.

The angular distribution is approximately isotropic for the secondary photons from photo-nuclear interactions with a slight shift towards smaller angles, which hints at the existence of more high-energy particles for photo-nuclear interactions.

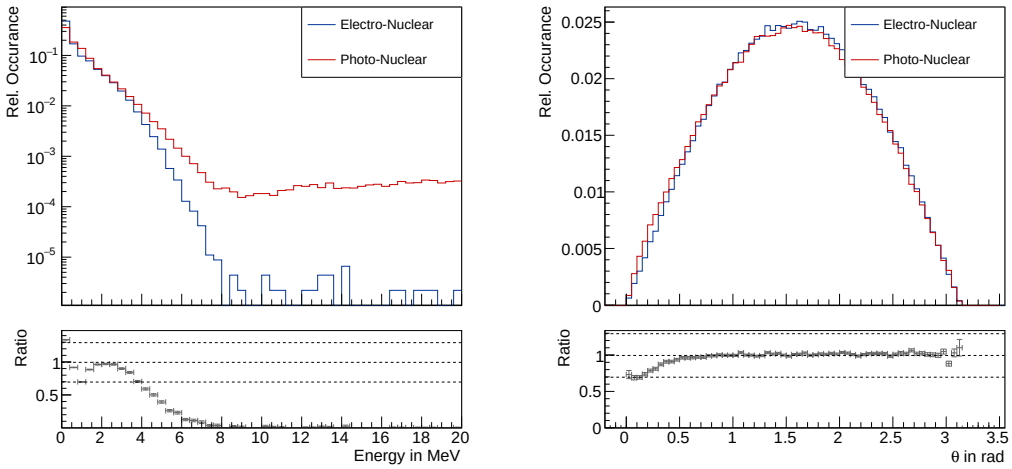

Figure 5.25: Energy (left) and θ (right) of secondary photons for a FLUKA simulation with $2.5 \cdot 10^9$ photons on target, comparing electro-nuclear processes and photo-nuclear processes.

In figure 5.27 the distributions are given for the secondary hadrons from either electro- or photo-nuclear processes. The energy distributions of the secondary hadrons are similarly distributed for the two

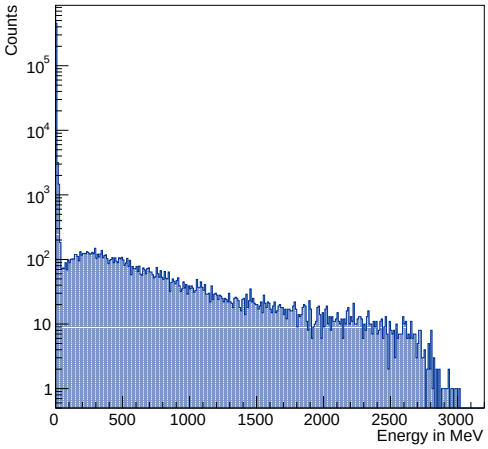

Figure 5.26: Energy of secondary photons for a FLUKA simulation with $2.5 \cdot 10^9$ photons on target.

processes. Both θ distributions are roughly isotropic, with shifts towards smaller angles. The shift is more dominant in the photo-nuclear spectrum, thus more high-energy hadrons are produced in such processes.

As mentioned above and observed in the figures, the photo-nuclear interaction has more high-energetic secondary particles compared to its total amount of particles, which explains the shifts of the angular θ distributions of secondary photons and hadrons towards smaller angles. The statistical difference becomes apparent in the unscaled histograms (see A.8 to A.11), where the photo-nuclear distribution has less hadrons at all energies, but the distribution of the high-energy hadrons has more statistics than the electro-nuclear distribution. Since photo-nuclear interactions correspond to the extreme case of electro-nuclear interactions, where the electron looses all of its energy, the many hadrons and photons with large energies can be explained.

The distributions for high-energy photons and hadrons can be viewed in figures 5.28 and 5.29. For the high-energy secondary hadrons the ratio is constant over a large range of the energy and angle θ and fluctuates only in the region with less statistics. The ratio for the secondary high-energy photons exhibits fluctuations over the full range of the energy distribution and angle θ. There is a substantially larger amount of high-energy secondary photons for the photo-nuclear process compared to the electro-nuclear secondary photons. The energy spectrum has many more entries up to much higher energies and the θ spectrum is shifted towards smaller angles.

In figure 5.30 the correlation between the angle θ and energy a hadron obtains in the photo-nuclear interaction is given together with the mean per bin. The same result as for electro-nuclear interactions can be obtained, namely that low-energetic hadrons are radiated isotropically from the nucleus and the higher the energy of the hadron, the smaller the angle and thus the more forward its direction. Though similarly to the electro-nuclear interactions, there is a substantial amount of high-energy (>500 MeV) hadrons that obtain angles larger than the coverage of the HCal (>0.6 rad).

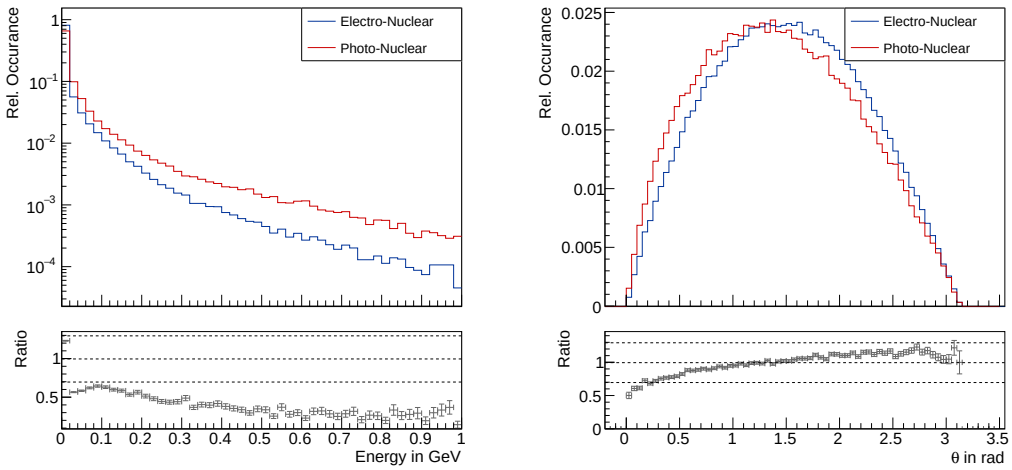

Figure 5.27: Energy (left) and θ (right) of secondary hadrons for a FLUKA simulation with $2.5 \cdot 10^9$ photons on target, comparing electro-nuclear processes and photo-nuclear processes.

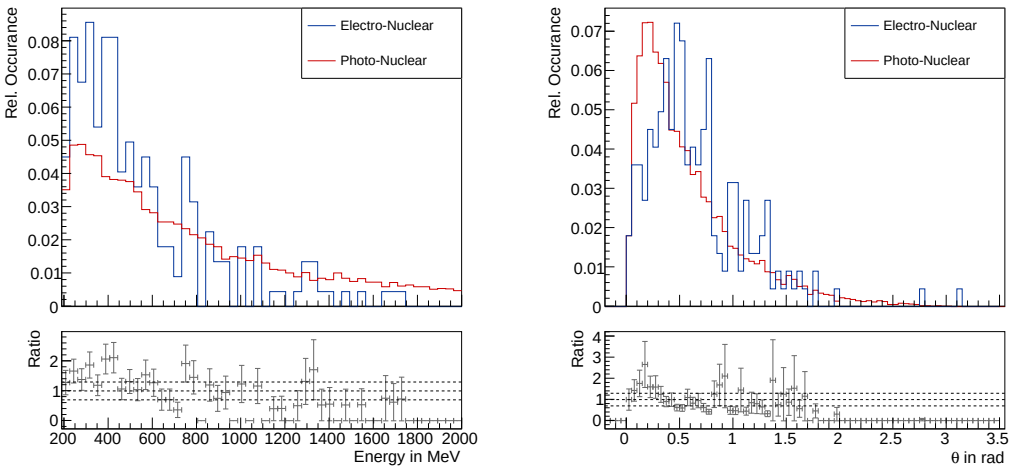

Figure 5.28: Energy (left) and θ (right) of secondary photons with applied energy cut for a FLUKA simulation with $2.5 \cdot 10^9$ photons on target, comparing electro-nuclear processes and photo-nuclear processes.

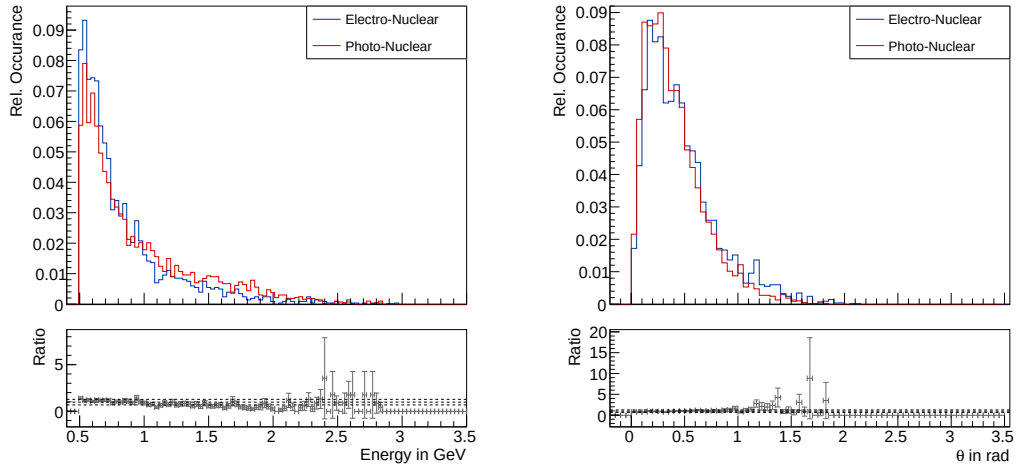

Figure 5.29: Energy (left) and θ (right) of secondary hadrons with applied energy cut for a FLUKA simulation with $2.5 \cdot 10^9$ photons on target, comparing electro-nuclear processes and photo-nuclear processes.

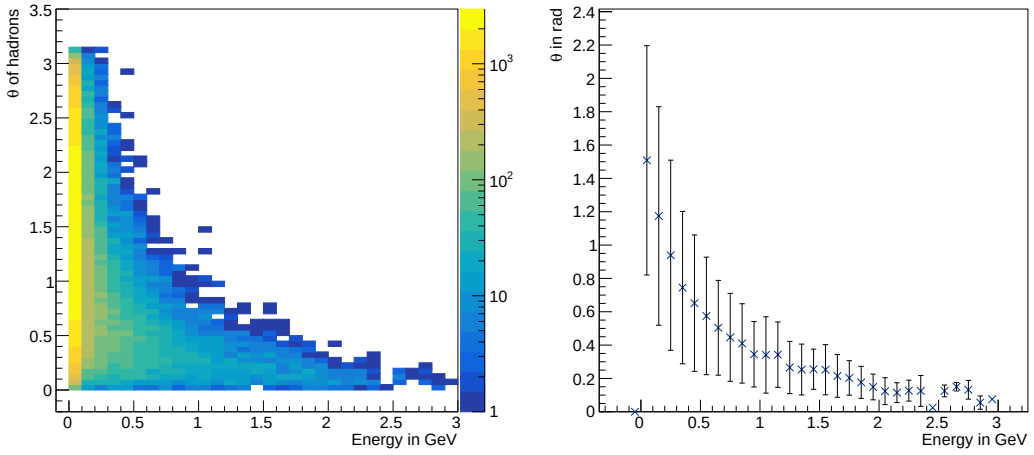

Figure 5.30: θ-energy correlation of hadrons encountered in a FLUKA simulation with $2.5 \cdot 10^9$ photons on target, (left) and the mean per energy bin with standard deviation (right). If the standard deviation is zero, then there is only one hit in that bin.

Even though differences can be spotted and are also expected for photo- and electro-nuclear interactions, the overall distributions are similar, making the veto strategies analogous. Both electro- and photo-nuclear interactions have a substantial amount of secondary photons and hadrons radiated isotropically, challenging current veto strategies. It is important to note that the probability to obtain a 3.2 GeV photon from bremsstrahlung in the target is highly unlikely and most photons that potentially produce photo-nuclear backgrounds will have substantially less energy, making differences between the electro- and photo-nuclear distributions smaller.

The impact of secondary particles from photo-nuclear interactions that are created in other sensitive detector materials, like the tracking planes or the ECal should be kept in mind and must be studied in more detail with a full detector simulation of the LOHENGRIN experiment. Since the tracking layers are much thinner $0.01 \cdot X_0$ than the actual target $0.1 \cdot X_0$, the impact of photo- or electro-nuclear interactions are expected to be low there.

5.6 FLUKA event selection

In order to get a rough estimate of electro-nuclear events in the signal region of the experiment, an event selection is applied to the Monte Carlo truth data. The number of simulated events is increased to $2.5 \cdot 10^{12}$ to obtain more statistics, while using a reasonable amount of computational resources. This leaves a factor of 160 to obtain the planned $4 \cdot 10^{14}$ e.o.t. and the results must be scaled by that factor.

The applied event selection is based on section 3.5. In table 5.3 four different scenarios are presented. The first event selection is based on the baseline scenario presented in [5], with the added constraints of the calorimeters. The equations are chosen such that if particles in an event fulfil the conditions, then it counts as a signal-event. For scenario (1) a signal-like electron is found if a recoiling electron with less than 75 MeV and $\theta < 0.2$ rad is detected. The θ-cut is applied due to the angular coverage of the trackers downstream of the target, as a recoiling low-energetic electron is required for a signal event. The whole event is signal-like if in addition to the signal-like recoiling electron, no hadron is detected in the HCal and no photon leaves a significant amount of energy in the ECal, hence the angular cuts for hadrons and photons. This leaves a total of 90 events in the signal-region.

In this first scenario the energy cut on the recoil electron is rather optimistic, since recoiling electrons with less than 25 MeV get increasingly difficult to reconstruct using the baseline tracker [5]. However, the presence of a recoiling electron in the final state is needed for a signal event. Thus in the second scenario the minimum recoil electron energy cut is applied in addition to the previous cuts,leaving 71 signal-like events.

Since high-energy photons can create an electromagnetic shower in the hadronic calorimeter and thus produce a signal there, a cut is added in scenario (3) to take this into account, which reduces the signal-like events to 30. The number of signal-like events for each scenario is given in table 5.4 together with the number of hadrons and photons encountered. The number of signal-like events decreases with the additional cuts, regarding scenarios (1) to (3). Exemplary for scenario one the energy and θ distributions for secondary photons and hadrons are presented in figures 5.31 to 5.34. The angular coverage of the calorimeters is clearly visible in the θ histograms for the secondary particles. In figures 5.31 and 5.32 the angles θ start after 0.1 rad, where the ECal is placed. For the high-energy photons it is clearly visible that many photons with energies $O(\text{GeV})$ are not detected by the ECal and also many low-energy photons are radiated at angles far above the angular coverage of the calorimeter. The same observations can be seen for the secondary hadrons in figures 5.33 and 5.34. In the angular histograms

the coverage of the HCal is left out and all other secondary hadrons obtain angles above 0.6 rad and therefore miss the HCal. While many low-energetic hadrons are radiated isotropically, some events contain high-energy hadrons with angles up to $\theta = \pi$.

The distributions for the other scenarios are given in the appendix in section A.4 in figures A.12 to A.22.

The results of the three presented scenarios must be scaled to the actual number of electrons on target in order to compare it to the expected signal events. To scale the $2.5 \cdot 10^{12}$ to the planned $4 \cdot 10^{14}$ e.o.t. LOHENGRIN is planned to run for, the results must be multiplied by a factor of 160. The magnitude of signal-like events would therefore be $\mathcal{O}(10^3 - 10^4)$. Comparing this to the expected 10 to 100 actual signal events for the planned run time, it is obvious that the background rejection needs to improve by several orders of magnitude or other veto strategies need to be explored.

Table 5.3: Tabulated encountered particles in FLUKA simulation with corresponding event selection.

Event Selection	1	2	3	4
$E_{\text{recoil}} < 75\,\text{MeV}$	×	×	×	×
$\theta_{\text{recoil}} < 0.2\,\text{rad}$	×	×	×	×
$E_{\text{recoil}} > 25\,\text{MeV}$		×	×	×
No hadron with $\theta_{\text{had.}} < 0.6\,\text{rad}$	×	×	×	
No photon with $\theta_\gamma < 0.1\,\text{rad}$	×	×	×	×
No photon with $\theta_\gamma < 0.6\,\text{rad}$ if $E_\gamma > 200\,\text{MeV}$			×	
No hadron with $\theta_{\text{had.}} < 0.1\,\text{rad}$				×

Table 5.4: Tabulated encountered particles in FLUKA simulation with corresponding event selection.

Scenario	# of signal-like events	# of hadrons	# of photons	# of hadrons $E_{\text{had.}} > 500\,\text{MeV}$	# of photons $E_\gamma > 200\,\text{MeV}$
1	90	1340	494	75	92
2	71	1129	386	60	70
3	30	589	151	51	0
4	13218	372690	57503	15893	447

Up to now the MC truth data has been taken without the applied magnetic field or even taking the magnet into account. Scenario four applies a rigorous selection on the opening angle of the magnet, which is only 0.1 rad. At this point we use the MC truth data, where the magnet and magnetic field were not simulated for a rough estimation and also assume that hadrons and photons will be absorbed by the 30 cm thick iron bulk of the magnet. In section 6.3 in the next chapter, the ability of different particles to pass though the magnet will be studied. With this event selection 13218 events in the signal-region are left, see table 5.4. From what we have learned and understood about electro-nuclear interactions to this point, it is obvious that if the opening angle is determined by the geometry of the magnet, the ability to veto such events becomes increasingly difficult with the current detector setup. An addition of a hadron veto at large angles outside the magnet or extra tracking layers inside of the magnet bore, covering larger angles, might be possible solutions to this problem.

However, it is important to note that this is only an estimation using the MC truth data and the actual

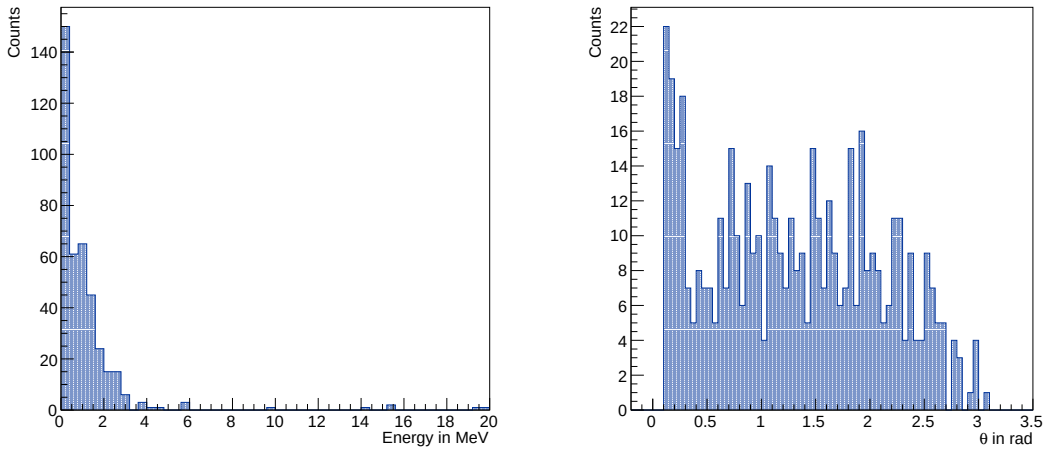

Figure 5.31: Photon energies and θ for a FLUKA run with $2.5 \cdot 10^{12}$ e.o.t. and applied event selection.

event selection must be studied with the detector responses of the ECal and HCal. A full simulation of the LOHENGRIN experiment should therefore be conducted to have more realistic results and also take the propagation and further interactions of the primary and secondary particles into account. In this context the impact of charged hadrons producing tracks in the tracking planes downstream of the target could also be studied. Since only a single charged track is required in the final state, any additional charged track produced by a charged hadron or even additional electrons, serves as a veto of the event. Another factor that needs to be studied in a full simulation of the experiment are the many neutral pions (FLUKA number 23) encountered in the final state, as they decay almost instantaneously into a pair of photons [75]. These photons might leave a measurable signal in the ECal and could veto further events.

From the studies on electro-nuclear interactions presented in the previous chapters, it has become apparent that electro-nuclear processes might pose a problem to the sensitivity of the experiment. An additional hadron and photon veto at large angles might be able to restore the sensitivity of the experiment.

Some event selection scenarios applied to the MC truth data have been explored in this section and even though this helps in understanding the distributions of particles and estimates the sensitivity of the detector setup, it is a first-order and rather simplified approach. Therefore in the next chapter, the electro-nuclear events simulated with FLUKA will be seeded into the detector setup and sampled into events from SM QED interactions. Especially interesting is the ability of the ECal to veto high-energetic photons from electro-nuclear interactions with the constant background of photons from SM QED Bremsstrahlung. This way the realistic detector responses can be studied and the number of events vetoed by the actual setup can be compared to the MC truth results.

5.7 Summary

This chapter focused on the investigation of electro-nuclear interactions as background for the LOHENGRIN experiment with the simulation framework FLUKA. The kinematics of electro-nuclear processes in a target made up of ^{184}W have been analysed using Monte Carlo truth data. The angular distributions of secondary photons and hadrons were visualized, confirming the isotropic distribution of the low-energy

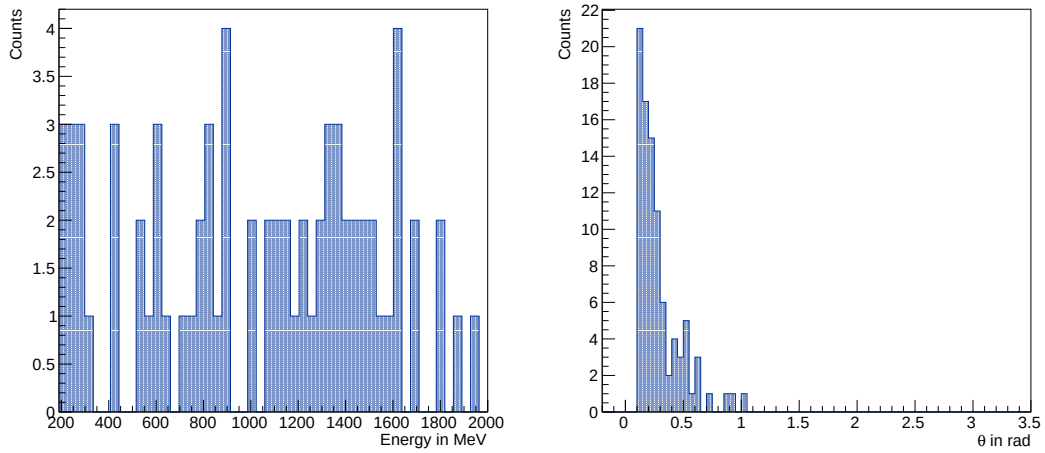

Figure 5.32: Photon energies above 200 MeV and corresponding angles θ for a FLUKA run with $2.5 \cdot 10^{12}$ e.o.t. and applied event selection.

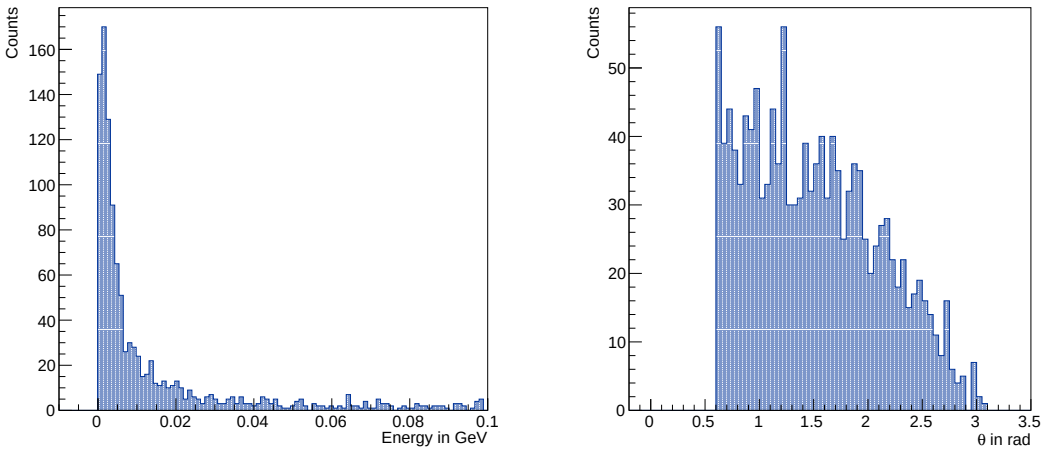

Figure 5.33: Hadron energies and θ for a FLUKA run with $2.5 \cdot 10^{12}$ e.o.t. and applied event selection.

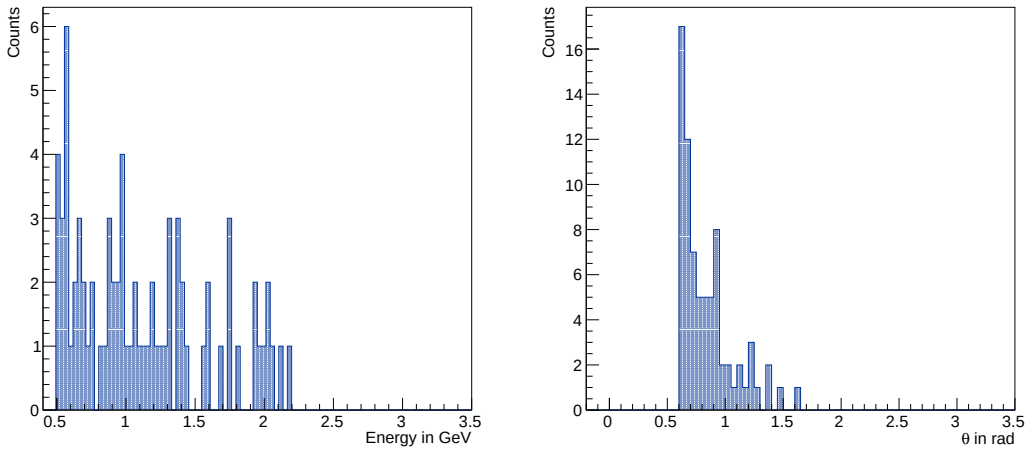

Figure 5.34: Hadron energies above 500 MeV and corresponding angles θ for a FLUKA run with $2.5 \cdot 10^{12}$ e.o.t. and applied event selection.

secondaries. In contrast, high-energy secondary particles are boosted in forward direction and thus obtain smaller polar angles θ, as expected. Various hadrons have been observed in the FLUKA simulation of electro-nuclear interactions with the low energy spectrum dominated by neutrons and protons and at higher energies pions and kaons gain in relative amount. FLUKA was shown to reliably simulate the signal region of the LOHENGRIN experiment with recoiling electron energies below 100 MeV.

The impact of the fermionic isotope of tungsten was also investigated by simulating electrons imping on a target made of ^{183}W. For the scope of this thesis the assumption of the neglectable impact of the fermionic tungsten isotope was verified, though further studies should be conducted regarding the full detector setup and a full simulation of the experiment. Additionally the impact of an impurity of 5 % nickel in the target was investigated and found to have minimal influence on the results.

Similarly to the previous chapter, the contribution of photo-nuclear interactions to the experimental background was examined and compared to the electro-nuclear process. Though differences could be observed, given their overall similar distributions, the veto strategies should be analogous. However, the impact of photo-nuclear interactions in other materials than the target should be investigated in a simulation of the full detector setup as well.

The final section in this chapter applied an event selection to the Monte Carlo truth data. From this section it became apparent that the current veto strategies for electro-nuclear events will not be able to sufficiently veto hadronic backgrounds from the experiment, leaving $O(10^4 - 10^6)$ hadronic background events in the signal region. Compared to the 1 to 100 actual signal events, the experiment would not be sensitive to the dark photon search any more. An alternative detector layout must be investigated to obtain the needed background rejection.

This far, the MC truth data has been analysed only, without accounting for the propagation of particles, the magnetic field and magnet bulk around the target and energy depositions in the calorimeters. This will be done in the next chapter, to study the detectability of electro-nuclear events in an actual detector geometry and take effects such as propagation, decay and interaction with matter of the secondary FLUKA particles into account.

CHAPTER 6

Detector simulation for hadronic backgrounds in GEANT4

From the analysis of the electro-nuclear events at generator level in the previous chapters, it is evident that a significant number of events with electro-nuclear interactions produce a signal-like signature in the final state. Up to now only the MC truth data has been analysed, which does not take into account the actual detector setup, detector responses and particle propagation. Therefore the final state particles from electro-nuclear interactions need to be placed into a detector geometry and the efficiency to veto electro-nuclear interactions with the current veto strategy, so the hadronic and electromagnetic calorimeters, will be studied. To do so, the detector setup excluding the trackers will be implemented in GEANT4. In chapter 4, problems with the simulation of the electro-nuclear interaction in the target were found, however, the simulation of detector responses works well in GEANT4 [55, 56]. Additionally it is written in C++ in contrast to `Fortran` used in FLUKA and the detector construction as a whole is more straight forward. The interaction of the electron beam with the target is therefore simulated using FLUKA and the detector response to the final state particles is simulated using GEANT4 by embedding the four-vectors of the final state particles simulated in FLUKA into a GEANT4 detector simulation.

The detector setup implemented in GEANT4 for this study is introduced in section 6.1 and the calorimeter function is tested in section 6.2. Due to the issues during the event selection in the previous chapter with the opening angle of the magnet, a short study on the transmission of neutrons, photons and charged hadrons through thick iron sheets will be conducted, to see if in reality particles are able to pass the magnet bulk used in the setup, see section 6.3. In section 6.4, energy deposits in the ECal and HCal produced by electro-nuclear final state particles from FLUKA are discussed. A short effort towards an additional veto strategy will be made in section 6.5, by adding a calorimeter around the magnet. Finally in section 6.6 the electro-nuclear events are sampled into the constant QED background and the detector results including a digitization algorithm for the ECal are evaluated.

While in the previous chapters only primary electrons and secondary particles from electro-nuclear interactions have been analysed, it is important to note that in this chapter the secondary electro-nuclear particles can decay or interact with the detector material an thus produce secondary particles. These particles will be called *tertiary* particles in the following, meaning all particles that have been produced by secondary electro-nuclear particles in the detector setup. This applies to the following sections, except section 6.3, where the primary particles are simulated in GEANT4.

6.1 Detector Setup

The detector setup is implemented as explained in section 3.4 but with some simplifications. The main simplification is the geometry of the magnet, as it is implemented as a cylinder with a slit, and not a rectangular "C"-shape. The cylinder has an inner radius of $r_{\text{inner}} = 10\,\text{cm}$ and an outer radius of $r_{\text{outer}} = 40\,\text{cm}$ and extends from 2.86° to 357.14°. The magnet is in total 1 m long and starts at position $(0, 0, 0)$ cm. The extent and placement of the magnet has a historical reason: at the time of the implementation of the setup, it did not seem important that the magnet extends downstream of the target, due to the forward placement of the calorimeters, and thus this simplified geometry was chosen. However, it should be kept in mind and tested with the correct extent of the magnet in the setup.

The ECal is implemented according to the CALICE ECal, see figure 3.8 in chapter 2. One ECal layer consists of an active silicon sheet and an absorber tungsten sheet, separated by air to account for glueing the assembly of the calorimeter in its support frame. Each such layer is separated by 5.4 mm of air. The silicon layers consist of 96×96 pixels, which are (5×5) mm large. The readout chips will not be simulated here, but need to be kept in mind for future applications.

The second major simplification in this geometry setup is the HCal, which is designed as an alternation of large iron absorber sheets and active silicon sheets. In this study silicon is used as the material for the hadronic calorimeter, as it provides an adequate approximation. Which active material will be used in the final detector setup is not set yet. However, in a practical experimental setup, a different material would have to be chosen due to the high cost of silicon.

The HCal has a hole in its center to account for the ECal and a slit along the positive x axis. The assumption to be verified for the HCal is, that there is no continuous background and thus the HCal can trigger for any significant energy deposit. The slit therefore needs to account for the deflected beam, such that the recoiling electrons do not deposit energy in the HCal and it needs to be chosen sufficiently large to reduce this background. For the purpose at hand a 30 cm large slit is used. A smaller slit extension in the xy plane would be ideal, to miss as few background particles as possible. However, smaller slit sizes do not sufficiently suppress energy deposits produced by the recoiling beam electrons.

The assumption for the HCal is that there is no continuous background and the simple existence of an energy deposit in the HCal is sufficient to veto events. This is rather idealistic, as leakages of energy deposits from the ECal and other backgrounds need to be considered. Whether this assumption is viable, will be investigated in the following sections.

The pixel detectors used for the tracking of the electron beam particles before and after the target, are not simulated at this point. The focus for this study is the HCal and ECal detector acceptance of the background events, which is why the tracking layers are not simulated in addition. However, the tracking layers add an important layer to the veto strategy and should be considered in the future, together with the HCal and ECal.

In figure 6.1 the detector setup drawn by the GUI in GEANT4 is given. The HCal is drawn in blue, the ECal in green, the magnet in yellow and the target in magenta. As the target is small in comparison to the calorimeters, it is visible by the pink pixel just before the magnet. The target is drawn for visibility only and will not be implemented in the following sections, since electron-target interaction was entirely simulated using FLUKA and thus the secondary particles should not interact in a GEANT4 target again. The blue outlines of the HCal clearly show the 30 cm slit and the hole for the ECal. The white outline corresponds to the size of the world volume.

In the following simulations the standard `FTFP_BERT` physics list is used in GEANT4.

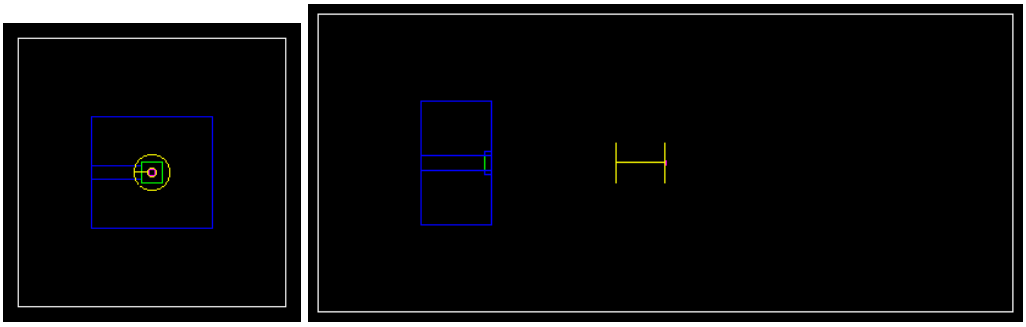

Figure 6.1: Detector setup implemented and visualized in GEANT4 along the z-axis (left) and along the x-axis (right) with the HCal (blue), ECal (green), magnet (yellow) and the target (magenta).

6.2 Test of calorimeter function

In order to validate the simulation of the calorimeters, a simple GEANT4 simulation without the target, magnet and magnetic field is performed. For this 10^4 e.o.t. are simulated and the energy deposits - or *hits*[1] - collected in the sensitive material of the calorimeters are analysed. Each hit in the GEANT4 simulation has a distinct energy, position and time, which can be saved. In figure 6.2 the collected hits over all events and all layers of the calorimeters can be viewed for the ECal and HCal. This hit map is a projection of all energy deposits in the calorimeter layers onto the xy-plane. The spot of hits accumulated in the center of the ECal is created by the electrons, which are not deflected since the magnetic field is not included.

The HCal does not have pixelized sensitive layers in this simulation and thus gives a more precise position in x, y and z. This is misleading, as in reality the HCal will not be able to supply such precision, but since the HCal simply serves the purpose to veto all events with significant energy deposition, this approach will suffice at this point.

The implemented slit is clearly visible and the hits accumulate in the center of the HCal and get more rare at larger angles. The single hit that appears to be in the region of the slit is a binning issue during the visualisation of the energy deposits. The HCal also has a spot of higher hit rates in its center, in the layers behind the ECal. The electromagnetic showers initiated by the 3.2 GeV electron beam in the ECal therefore leak into the HCal. At such energies this is to be expected, though it should be checked for the full simulation, whether or not this leakage effect is present. If so it might be considered to build a thicker ECal with more layers to avoid this type of leakage into the HCal. It is important to note that not all leakages can be reduced completely, since particles can also hit the ECal along its borders or at an angle, but it is important to minimize leakages as far as possible. It would be interesting to study leakage effects into the HCal in the future in more detail, in particular how likely events are vetoed by the HCal due to leakages from the ECal.

In figure 6.3 the position in z direction per hit is provided. The longitudinal shower profiles correspond to the theoretical expectation [79], though the shower profiles are slightly cut-off at their tails. This is to be expected, since the leakage into the HCal is visible.

Additionally the amount of energy deposited in the calorimeters can be viewed in figure 6.4. The energy deposits per hit are less than 10 MeV for the majority of hits in both calorimeters. This is to be

[1] Hits and energy deposits are used synonymously in the following sections.

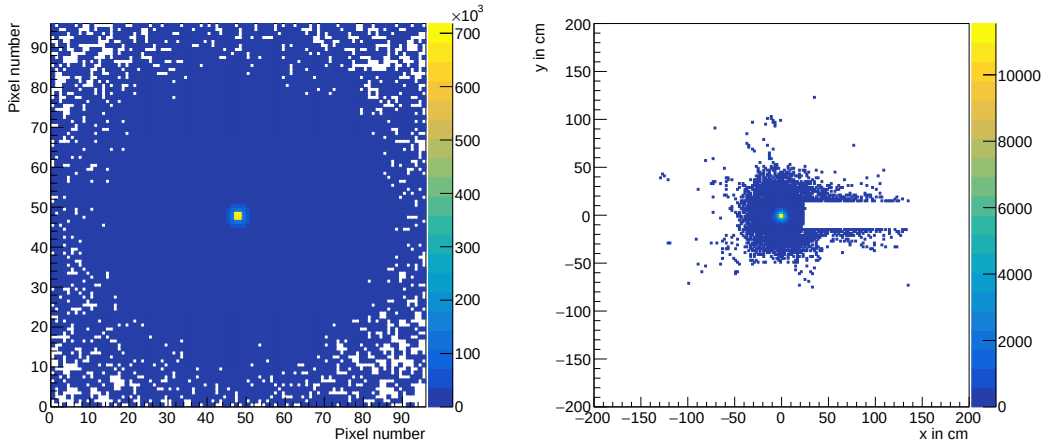

Figure 6.2: Simulated 10^4 e.o.t. to show the hits in the ECal and HCal accumulated over all events. Hits are accumulated in the pixels in the ECal and for the HCal the position is provided.

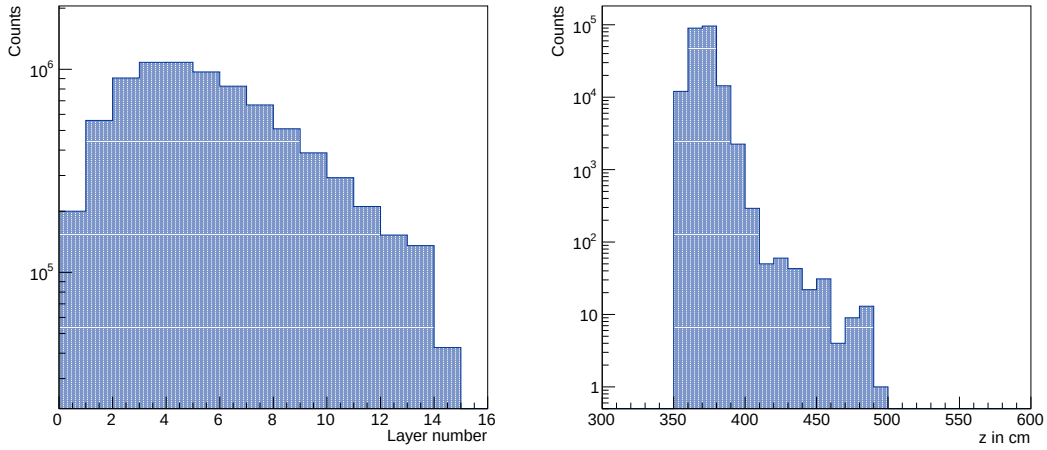

Figure 6.3: Simulated 10^4 e.o.t. to show the z-position in the ECal and HCal accumulated over all events. Energy deposits are recorded per layer in the ECal and the position in z is given for the HCal.

expected, since high-energy particles loose most of their energy in the non-active absorber material and the energy deposits are collected in the sensitive materials and are thus much smaller. A 640 MeV photon would for example correspond to a $\approx$ 20 MeV energy deposit in the ECal. Most energy deposits are far below that, showing that most hits are created by low-energetic particles with only few MeV in the calorimeters.

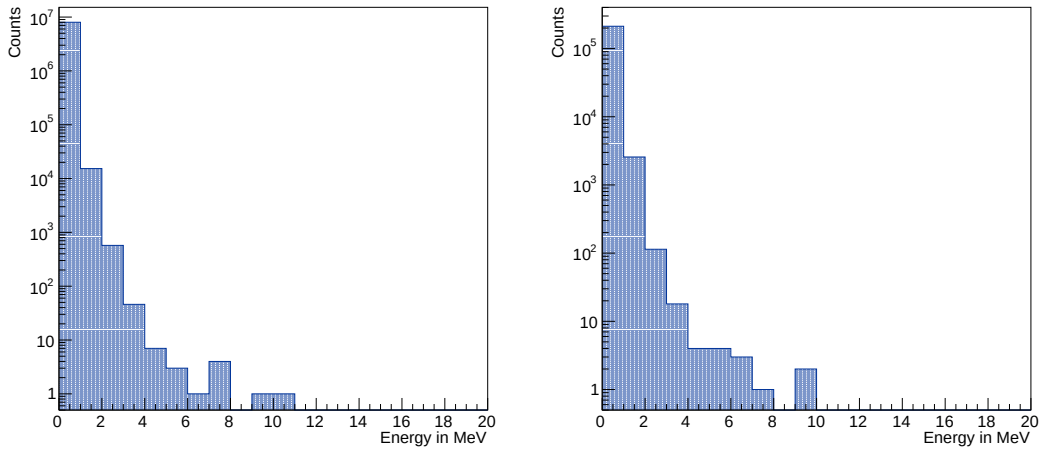

Figure 6.4: Simulated 10^4 e.o.t. to show the energy deposits in the ECal and HCal accumulated over all events.

6.3 Magnet study

An important component of the experiment is the magnet and as already mentioned, it might pose a problem regarding the detectability of hadrons and photons at larger angles than the opening of the magnet itself. To study at which energies particles are able to pass through the iron of the magnet, a simple GEANT4 simulation is set up. It is important to note that in this simulation the beam particles are simulated using GEANT4 and different particles at varying energies are shot onto iron slabs of varying thicknesses and the percentage of primary particles passing the iron slabs is presented. For each thickness and energy paring, 10^5 events are simulated. A primary beam particle is shoot onto the iron slab and only if that particle passes the material, it is counted as a "surviving" particle. If a high-energy particle is stopped in the magnet, and its secondary particles escape the iron slab, then this is not counted as a signal at this point. This should be kept in mind especially regarding the study of an additional veto calorimeter around the magnet.

In table 6.1 the results for neutrons as beam particles can be viewed. The results for different energies can be explained from the cross section of neutrons interacting with matter. Neutrons only interact via the strong interaction and can interact elastically or inelastically with the iron material. For energies up to a few MeV the cross section is slightly larger than for energies of hundreds of MeV to GeV, where the cross section remains roughly constant. [80] The attenuation of high-energy neutrons in iron with a nuclear interaction length of 16.77 cm [81] can be approximated by [48]

$$f = e^{-x/\lambda_{\text{iron}}} = 0.888 \quad , \tag{6.1}$$

where λ_{iron} corresponds to the nuclear interaction length and $x = 2\,\text{cm}$ is the thickness of the iron slab. This approximated value corresponds to the observations from the data simulated with GEANT4 for neutrons with an energy above 100 MeV. Below that the elastic cross section is slightly larger and thus the neutrons are more likely stopped. [80]

At 30 cm thickness only a small fraction of high-energy neutrons pass through the iron slab. At energies lower than 10 MeV the detection of neutrons behind the magnet bulk is almost not possible.

Since most produced neutrons during electro-nuclear interactions have kinetic energies in the order of 10 MeV or below and obtain large angles, the need of a hadron veto in close proximity to the target becomes apparent. Of course events also contain a few high-energy particles, but since many of the high-energy hadrons also obtain larger angles than the opening angle of the magnet, it is not clear if they are enough to veto full events.

Additionally pions, protons and photons are studied as beam particles and the results are given in tables 6.2, 6.3 and 6.4. Since protons and pions are charged under the electromagnetic interaction, they can loose energy via ionization and atomic or collective excitation. The Bethe-Bloch formula describes this energy loss behaviour, which steeply decreases from energies between 10 MeV to 100 MeV and then only slightly rises again from 500 MeV to 1 GeV and onwards [48]. This is reproduced by the simulations with GEANT4: at low energies the protons and π^+ interact in the magnet and are thus stopped, whereas at higher energies the charged hadrons interact less likely and can therefore pass the iron bulk. At 30 cm iron thickness, the charged pions are slightly more likely to pass the magnet bulk.

In table 6.4 the photon results are presented. The cross section for photons at energies between 10 MeV and 1 GeV is a combination of different processes. The most dominant are Compton scattering off an electron and pair production. At low energies Compton scattering dominates, resulting in some of the photons to be absorbed, but a majority passing the thin slab. At higher energies pair production is the dominating process and the photons are thus absorbed more likely. [48]

For both photons, protons and pions the detectability at 30 cm iron slab thickness is small. Due to the large magnet bulk, the ability to detect electro-nuclear events is drastically reduced, since hadrons with angles 0.1 rad $< \theta <$ 0.6 rad are less likely to be detected. The previously assumed rigorous event selection, which was determined from the opening angle of the magnet, might not be as pessimistic, but rather realistic. The idea of a hadron veto at large angles and close proximity to the target seems to be necessary for efficient background rejection. However, previously only the MC truth data has been analysed and particle propagation has not been considered, therefore a full simulation of the detector setup is necessary to study the detectability of electro-nuclear events.

Table 6.1: Fraction of neutrons observed after the iron slab for varying iron slab thicknesses and particle energies from a simple GEANT4 simulation with 10^5 events.

	2 cm	10 cm	20 cm	30 cm
10 MeV	0.76	0.21	0.037	0.0063
100 MeV	0.88	0.52	0.29	0.13
500 MeV	0.89	0.54	0.29	0.15
1 GeV	0.88	0.51	0.26	0.13

Table 6.2: Fraction of protons observed after the iron slab for varying iron slab thicknesses and particle energies from a simple GEANT4 simulation with 10^5 events.

	2 cm	10 cm	20 cm	30 cm
10 MeV	0	0	0	0
100 MeV	0	0	0	0
500 MeV	0.89	0.55	0.30	0
1 GeV	0.88	0.51	0.26	0.14

Table 6.3: Fraction of π^+ observed after the iron slab for varying iron slab thicknesses and particle energies from a simple GEANT4 simulation with 10^5 events.

	2 cm	10 cm	20 cm	30 cm
10 MeV	0	0	0	0
100 MeV	0.83	0	0	0
500 MeV	0.89	0.53	0.27	0.12
1 GeV	0.88	0.53	0.28	0.15

Table 6.4: Fraction of photons observed after the iron slab for varying iron slab thicknesses and particle energies from a simple GEANT4 simulation with 10^5 events.

	2 cm	10 cm	20 cm	30 cm
10 MeV	0.75	0.20	0.03	0.004
100 MeV	0.53	0.04	0.002	0.0002
500 MeV	0.45	0.02	0.0004	0.00003
1 GeV	0.43	0.02	0.0003	0.00002

6.4 Electro-Nuclear events in the Detector setup

Up to now the electro-nuclear events have been analysed on the basis of the Monte Carlo truth data, without taking the detector setup into account. In the following section the electro-nuclear events simulated with FLUKA are placed into the above explained GEANT4 geometry and the secondary particles are all propagated and handled by GEANT4. Energy deposits in the calorimeters can be recorded, as explained in section 6.2, to study the detectability of the secondary particles and detector responses of the calorimeters. The MC truth FLUKA particles are placed into the detector geometry and simulated separately, to examine the energy deposits and veto strategies for these isolated events. A possible pile-up effect from SM QED events on the veto efficiency will be analysed in section 6.6.

All events with a signal-like electron from the FLUKA simulation of $2.5 \cdot 10^{12}$ e.o.t. will be analysed, which are in total 17394 events. These events are read into the GEANT4 simulation and placed at the position of the target. To account for the beam extent, the positions x and y are smeared by a Gaussian [82]:

$$G(x) = \frac{1}{\sqrt{2\pi}\sigma} e^{-\frac{(x-\mu)^2}{2\sigma^2}} \quad , \tag{6.2}$$

with $\sigma = 1$ mm standard deviation in both the x and y directions. The z position is chosen as the center of the target, so at -0.01752 mm. Once placed, particles of a single event are propagated and they interact with the detector materials as predicted by the underlying physics processes. Every 2 ns a new event is propagated through the detector setup, where one event corresponds to one electro-nuclear interaction from FLUKA and its respective secondary particles.

As mentioned before, it is important to differentiate two different types of secondary particles: the primary GEANT4 particles in this simulation correspond to the secondary particles from electro-nuclear interactions in FLUKA. These secondary FLUKA particles can in turn produce secondary particles through interactions in the detector material or decays in the GEANT4 simulation. As mentioned above, all MC truth FLUKA particles will be called *secondary* particles in the following and all other produced particles

in GEANT4 are called *tertiary* particles. The primary electron is not simulated in the detector setup.

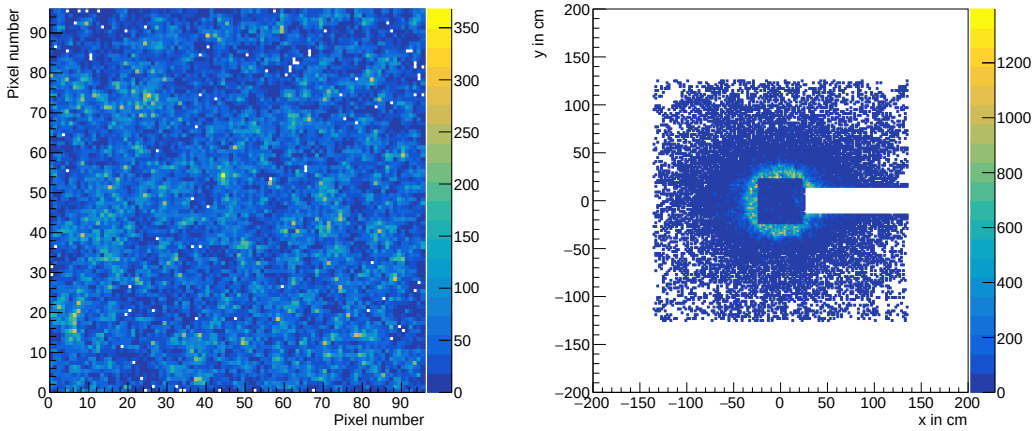

Figure 6.5: Hit collections in the pixels of the ECal (left) and positions in the HCal (right) for all 17394 electro-nuclear FLUKA events in the GEANT4 geometry.

In figure 6.5 the hit collections of the full run in the ECal and HCal can be viewed. The histograms show all energy deposits in the xy-plane by secondary FLUKA particles and tertiary particles produced in the GEANT4 simulation. The histogram is a projected hit map in the xy-plane, meaning it is integrated over z. As expected for the isolated electro-nuclear events, rates in the ECal are low and homogeneously distributed. In the HCal a ring of higher hit rates can be viewed around the ECal, which corresponds to the opening angle of the magnet. Particles with smaller angles than the opening angle of the magnet are detectable and at larger angles they are most likely absorbed by the bulk of the magnet.

Hits of different particle types in the hadronic calorimeter can also be analysed, see figures 6.7 and 6.8, where the hit collections in the HCal for photons, electrons, positrons and different hadrons can be viewed. At this point all energy deposits of different particle types are taken into account, thus not differentiating secondary FLUKA particles and particles produced during electromagnetic or hadronic showers in the calorimeters. In figure 6.7 the energy deposits of photons, electrons and positrons are given. It is interesting that the magnet opening angle is visible for photons and the leptons in the HCal, whereas this ring of hits cannot be seen for any hadrons, see 6.8. Secondary FLUKA photons that emerge the "target" in forward direction, with angles $\theta > 0.1$ rad above the opening angle of the magnet, induce a chain of reactions in the first few centi meters of the magnet bulk. Electrons and positrons are produced via photon conversion and can in turn produce photons via bremsstrahlung. In many instances one of the tertiary photons from such a reaction escapes the bulk of the magnet and initiates an electromagnetic shower in the HCal. This is the reason for the many hits in the HCal with a slightly larger angle than that of the magnet. Since electrons and positrons are produced during the creation of an electromagnetic shower, the ring of higher hit rates around the ECal is also visible for the leptons. In figure 6.6 this is visualised for an exemplary photon, to get a better understanding of the production of the higher hit rates around the ECal in the HCal.

It was shown that tertiary particles are created in the bulk of the magnet through decays or interactions of the secondary FLUKA particles and these tertiary particles deposit energy in the calorimeters. The effect of removing the magnet bulk, while keeping the magnetic field, can be viewed in figures A.23 and

A.24. Without the magnet bulk more hits are collected in the calorimeters and the ring of hits around the ECal is not visible in the HCal any more. As expected, hits accumulate at smaller angles in the ECal and HCal and get rarer for larger angles.

In figure 6.8 hits produced by hadrons in the HCal are presented. Energy deposits by all secondary FLUKA hadrons and protons, neutrons and pions that are produced during hadronic showers in the HCal are visualized. The distributions of hits for the oppositely charged pions show the impact of the magnetic field on the secondary FLUKA particles, as the negatively charged pions accumulate to the right of the ECal and the positively charged pions accumulate on the opposite side. Single particles that produce multiple energy deposits in the layers of the HCal can be seen by the track-like signatures of energy deposits for the charged pions.

Similar figures can be viewed in 6.9, where only the secondary particles from the electro-nuclear interactions in FLUKA that produced hits in the HCal are visualized. In comparison much less energy deposits of the different particle types are collected. This is to be expected, as a single particle can deposit energy multiple times in the sensitive material of the calorimeters and also induce an electromagnetic or hadronic shower, which in turn consists of hundreds of energy deposits. The many hits observed in figures 6.7 and 6.8 are thus mostly due to tertiary particles produced through showers in the calorimeters initiated by the secondary FLUKA particles and tertiary particles produced in the magnet bulk.

Photons and positrons from the FLUKA data do not produce hits in the HCal. The hit collections in figure 6.7 are thus mainly tertiary particles produced in the GEANT4 simulation, except for the few $O(1)$ FLUKA electrons.

It could be suspected, that the many additional hits in the previous figures are produced by particle interactions of the secondary FLUKA particles with air molecules, and thus producing tertiary particles that deposit energy in the calorimeters. However, changing the world volume material to vacuum does not reduce the amount of hits produced in the calorimeters, see figures A.25 and A.26. This shows that it is not necessary for the LOHENGRIN experiment to run in a vacuum tube, as the results of this study are not significantly altered in an experimental hall filled with air.

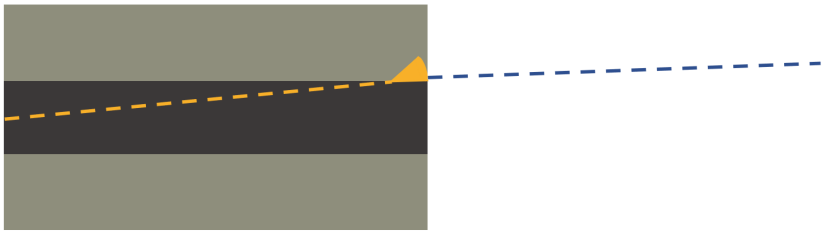

Figure 6.6: Visualized exemplary photon emerging from the target at an angle $\theta > 0.1$ rad in forward direction, producing a chain of reactions in the magnet bulk (yellow) and a photon from this reaction chain escaping the magnet bulk (blue) that produces a hit in the HCal.

Though quantitatively many energy deposits are recorded in the calorimeters, the ability to veto events is heavily dependent on how much energy is actually deposited per event. Each recorded energy deposit in both calorimeters can be viewed in figure 6.10. Both calorimeters have a majority of small energy deposits below 10 MeV and only rare high-energy single deposits are observed.

The number of vetoed events can be estimated using the energy deposits in the calorimeters on an

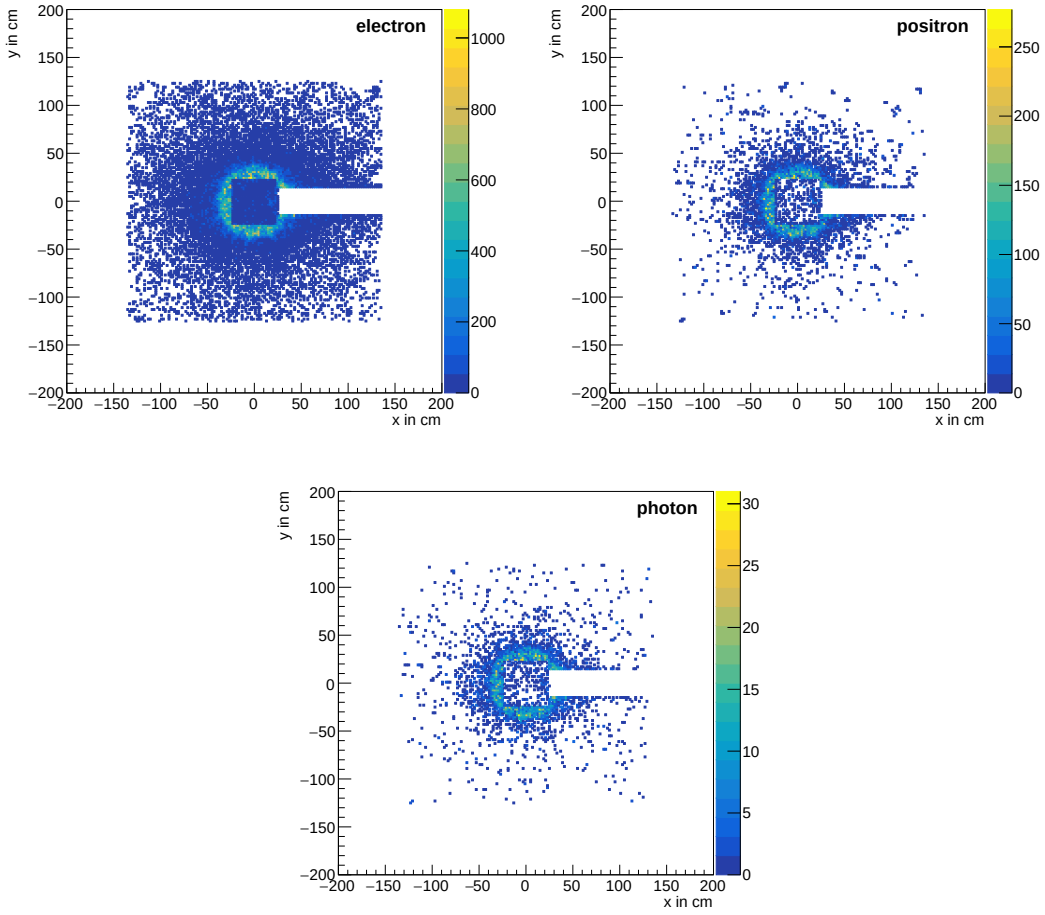

Figure 6.7: Hit collections in the HCal produced by photons, electrons and positrons for all 17394 electro-nuclear FLUKA events in the GEANT4 geometry.

event by event basis[2]. This corresponds to an idealistic, instantaneous read-out of the calorimeters that is not possible in reality. For the ECal the constant SM QED background would need to be considered for a more realistic read-out and digitization process. However, for a first approximation of hadronic final states in the signal region this will suffice. Thus all energy deposits in the calorimeter sensitive materials are summed up per event, see figure 6.11. Most of the events only have small energy deposits of a few MeV, with only few events with energy deposits in the ECal and HCal above 10 MeV. A significantly larger amount of events obtain larger energies in the HCal compared to the ECal. For different amounts of energy deposited in the ECal and HCal the number of vetoed events is presented in table 6.5. Most striking is the entry for events with more than 0 MeV: only 5526 events are vetoed for a minimum deposited energy in the calorimeters. This means that with such idealised conditions regarding the read-out of the calorimeters only 32 % of the electro-nuclear events deposit energy in the calorimeters and thus can be vetoed. Comparing the 11868 signal-like events to the 13218 hadronic

[2] For this simplified read-out, pileup cannot alter the results. In a realistic scenario pileup effects will become important and need to be kept in mind.

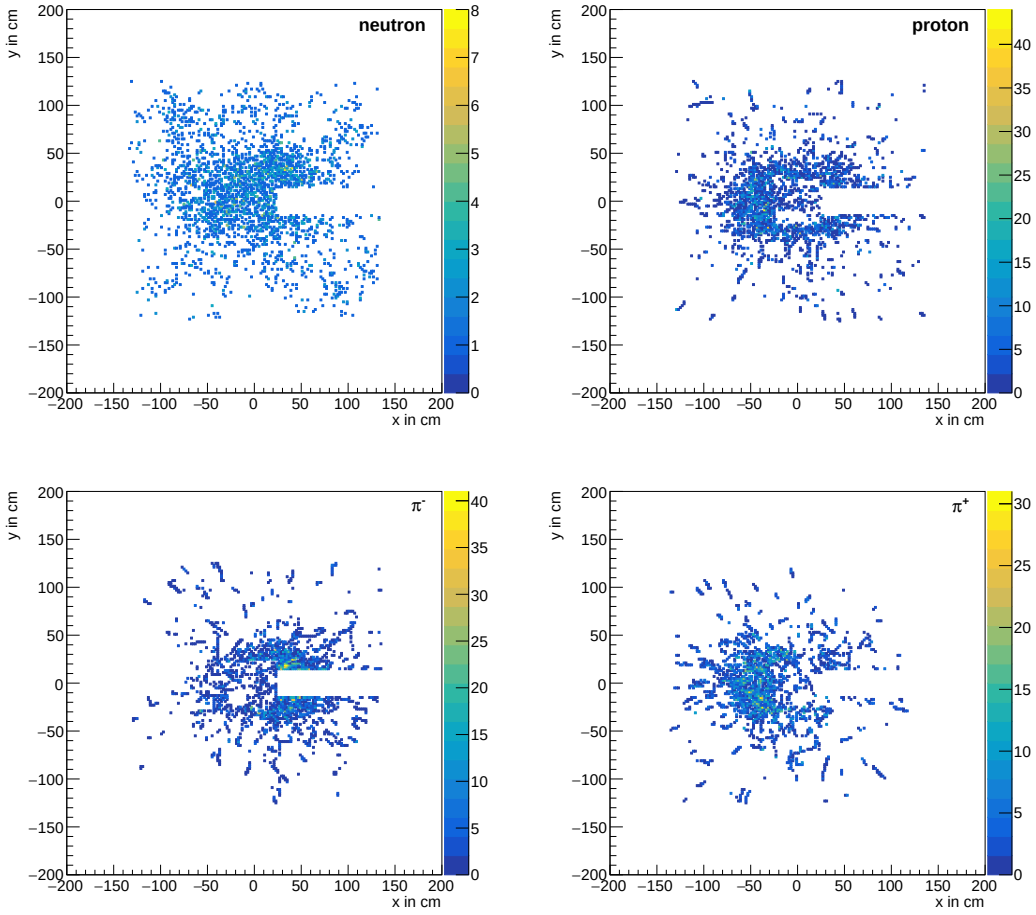

Figure 6.8: Hit collections in the HCal produced by different hadrons for all 17394 electro-nuclear FLUKA events in the GEANT4 geometry. The type of particle considered is given on the top right of the histogram.

background events from section 5.6, it is obvious that the event selection determined from the opening angle of the magnet was not as pessimistic as first assumed. The need for a larger angular coverage of the calorimeters and less impact of the magnet opening angle can be deduced from this data.

The number of hadronic background events must be extrapolated to the number of electrons on target at the LOHENGRIN experiment, yielding a total of

$$11868 \cdot 160 = 1.9 \cdot 10^6 \tag{6.3}$$

signal-like hadronic background events. Comparing this again to the 1 to 100 signal events for the same amount of electrons on target, it is clear that the current veto strategy is not sufficient for rejecting hadronic backgrounds produced via electro-nuclear interactions and the detector setup must be adapted to obtain sensitivity for the dark photon search.

It is important to note that the impact of the tracking detectors on the veto strategy regarding charged secondary hadrons has not been considered. In a future study this must be done in an implementation of

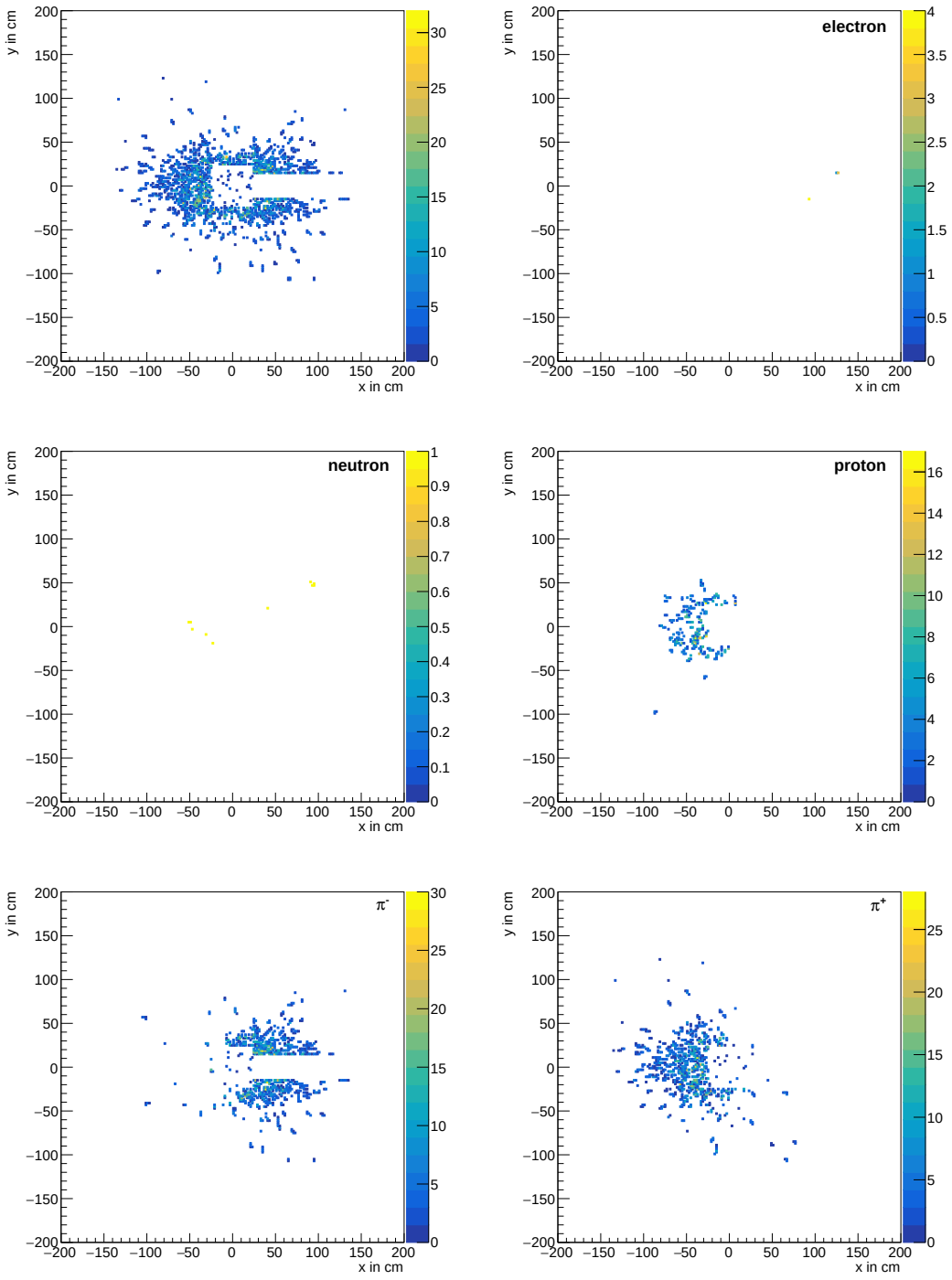

Figure 6.9: Hit collections in the HCal produced by different types of particles for all 17394 electro-nuclear FLUKA events in the GEANT4 geometry of only the secondary particles from the FLUKA simulation. The type of particle considered is given on the top right of the histogram.

the complete detector setup, as an improvement of the hadronic background rejection is to be expected with the tracking layers. Since many of the secondary hadrons are charged protons, pions or kaons, many of the electro-nuclear events might be vetoed due to the additional track in the final state. Though the trackers should not be able to account for all the hadronic events left in the signal region. A combination of the additional veto through the trackers and a redesign of the detector layout might be able to efficiently reject the hadronic final states in the signal region.

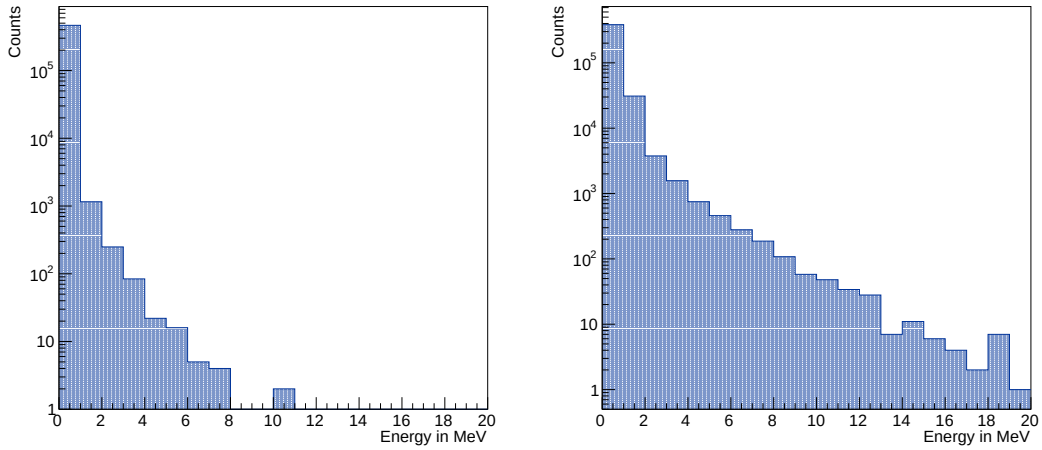

Figure 6.10: Energy deposits in the ECal (left) and HCal (right) for all 17394 electro-nuclear FLUKA events in the GEANT4 geometry.

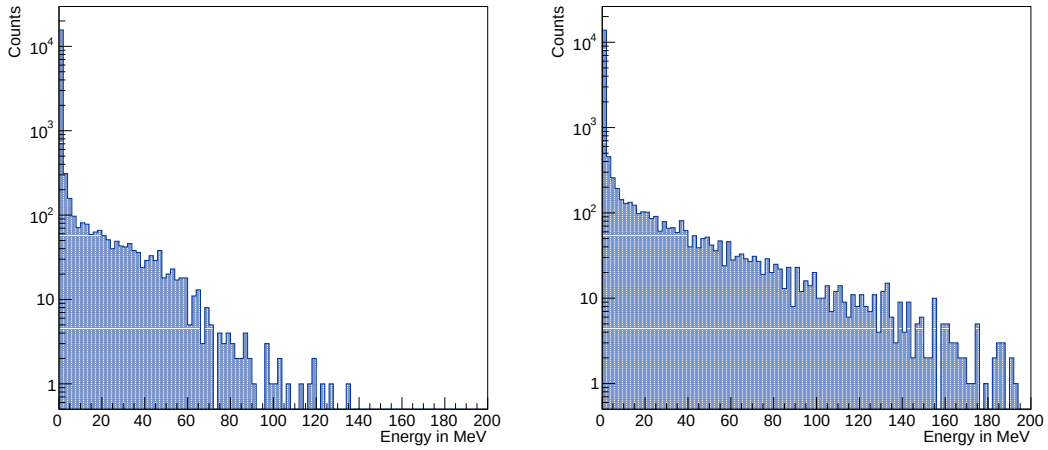

Figure 6.11: Energy deposits per event in the ECal (left) and HCal (right) for all 17394 electro-nuclear FLUKA events in the GEANT4 geometry.

In addition the hits in the ECal layers and HCal z positions are given in figure 6.12 and look similar to the previous section, where the function of the calorimeters was tested.

Table 6.5: Number of vetoed events by the ECal and HCal for different thresholds for the energy deposits in the calorimeters for the 17394 electro-nuclear FLUKA events.

ECal energy deposited	HCal energy deposited	vetoed events
30 MeV	20 MeV	2312
20 MeV	15 MeV	2708
20 MeV	10 MeV	2986
20 MeV	1 MeV	4113
10 MeV	1 MeV	4232
1 MeV	1 MeV	4569
> 0 MeV	> 0 MeV	5526

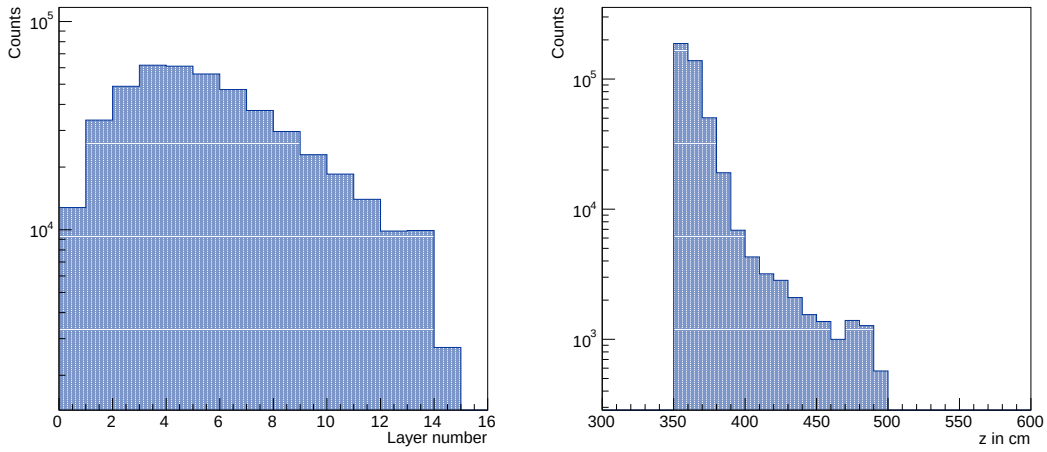

Figure 6.12: Collected hit layer in the ECal (left) and position in z HCal (right) for all 17394 electro-nuclear FLUKA events in the GEANT4 geometry.

To further strengthen the results from above, the angular correlation between a particle's polar angle at its creation and its last step in the simulation is calculated and analysed. For each hadron or photon its angle θ at the first and at its last step in the simulation is thus recorded and the two angles are filled in a histogram, see figure 6.13. The correlation between the two angles is presented for all secondary hadrons and photons from the FLUKA simulation. The distribution of all encountered hadrons looks as expected: most hadrons are isotropically distributed and do not change their direction before their track is stopped. For angles below π, so hadrons that emerge in forward direction, the magnetic field applies, changing the direction and angle of charged secondary hadrons. As the magnet bulk is also placed in forward direction, particles that obtain angles $\theta_{\text{start}} < \pi$ can be scattered in the material of the magnet. This explains the spread of the angles in the bottom half of the histogram. If particles are absorbed by the magnet bulk, their momentum components are set to zero and these particles are thus not included in the histogram, which explains the loss of statistics below starting angles of π.

The distribution for the secondary FLUKA photons is similar to the distribution of the hadrons. For secondary photons the loss in statistics below angles $\theta_{\text{start}} < \pi$ is more drastic. Most photons that emerge the target in forward direction are absorbed by the magnet and their 4-momentum components are set

to zero. These particles are not included in the histogram, which is causing the loss in statistics below $\theta_{\text{start}} < \pi$. That photons are absorbed more likely in the magnet than hadrons corresponds to the results of the previous section 6.3.

In addition the angular correlation for hadrons that deposit energy in the ECal and HCal is given in figure 6.14. For particles that produce a hit in the HCal, the distribution of θ looks as expected, with small θ at the start of the simulation and also small angles at the end of the simulation. Some hadrons obtain larger angles at their last step in the simulation, which is to be expected when they interact in the HCal. However, only 922 out of 475352, so a fraction of ≈ 0.002, of the secondary hadrons from electro-nuclear interactions deposit energy in the HCal and an additional 373, so a fraction of ≈ 0.0008, of the hadrons deposit energy in the ECal. The veto efficiency of the described hadron calorimeter can thus be expected to be low.

No secondary photon from an electro-nuclear interaction deposits energy in the ECal. Therefore all energy deposits observed in the ECal in figure 6.5 are produced by either secondary FLUKA hadrons, which produce a shower of electrons, positrons and photons or tertiary particles produced during the interaction of particles with the material of the magnet.

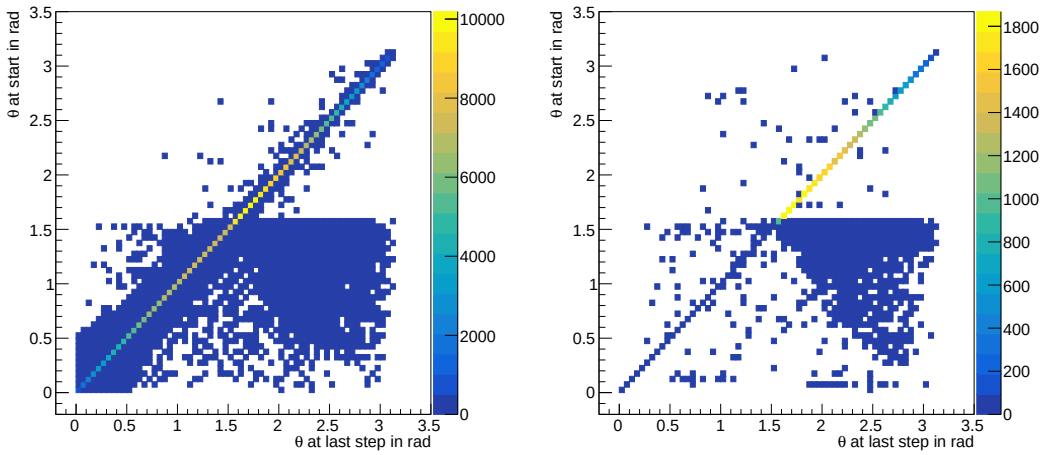

Figure 6.13: Angular correlation between angle θ at first encounter of a particle and its last step in the simulation for all secondary FLUKA hadrons (left) and secondary FLUKA photons (right) for all 17394 electro-nuclear FLUKA events in the GEANT4 geometry.

From what could be observed about the secondary particles in the GEANT4 detector setup, the veto efficiency for electro-nuclear backgrounds with the current strategy is low. Only a fraction of ≈ 0.002 of the secondary FLUKA hadrons deposit energy in the forward HCal and including all secondary particles in the GEANT4 simulation, only 32 % of the FLUKA events with signal-like recoiling electrons could be vetoed with the ECal and HCal in the current detector setup.

This section has thus shown the current veto strategy does not ensure efficient hadronic background rejection. The addition of a calorimeter with a larger angular coverage could be one way to improve the background suppression, which will be investigated in the following section.

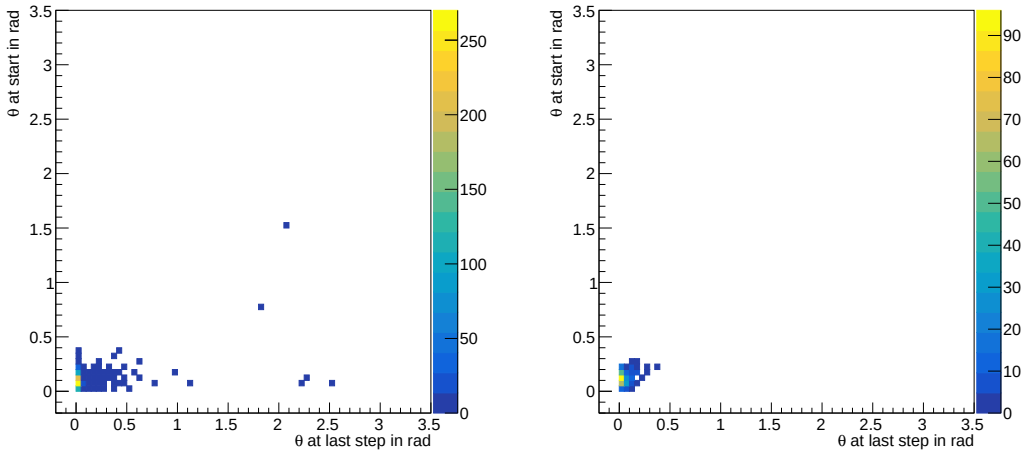

Figure 6.14: Angular correlation between angle θ at first encounter of a hadron and its last step in the simulation for all secondary FLUKA hadrons that produce hits in the HCal (left) and ECal (right) for all 17394 electro-nuclear FLUKA events in the GEANT4 geometry.

6.5 Additional veto calorimeter around the magnet

In the previous section the ability to detect electro-nuclear interactions with the detector setup in GEANT4 was shown to be minimal. Due to the opening angle of the magnet and the many hadrons and photons that emerge the target at large angles, the detectability in the calorimeters is small. One idea to improve the background rejection is to build an additional calorimeter around the magnet bulk. The probability to detect the particles outside the 30 cm thick iron bulk of the magnet is low, as presented in section 6.3. However, a silicon layer is added around the magnet to test the detectability of electro-nuclear secondaries there and verify the results. For simplicity a large silicon sheet is used as the calorimeter. If and how this additional calorimeter can be realised in the experimental setup is not determined yet and thus this simplification is sufficient for the study at hand. Silicon provides an adequate approximation and does not significantly affect the results. Again, in a practical experimental setup, a different material would have to be chosen due to the high cost of silicon.

Two different thicknesses for the silicon calorimeter are tested: a thin silicon sheet (1 mm) and a thick silicon sheet (10 cm). The latter option simulates the use of large crystal calorimeters around the magnet.

For this simple setup only the amount of energy deposited is of interest and not the position of the hit. The silicon layer starts at 40.1 cm radius, with a distance of 1 mm to the magnet. To account for the opening in the magnet, the silicon layer also does not cover the full angular coverage of 2π. It starts at 5 rad and extends to $(360 - 5)$ rad. The slit size is chosen slightly larger than that of the magnet, to ensure no particle producing a hit in the silicon layer, that escaped through the slit in the magnet. For the same slit size of calorimeter and magnet, many recoiling electrons from the electro-nuclear interaction escaped the slit in the magnet and produced a signal in the new calorimeter. A schematic is provided in figure 6.15. With a larger slit in the calorimeter, the amount of hits by recoiling electrons could be reduced. It is obvious that without a slit in the magnet bulk and the magnet extending behind the position of the target, that no recoiling electrons produce a signal in the additional calorimeter, which could be verified with a simulation.

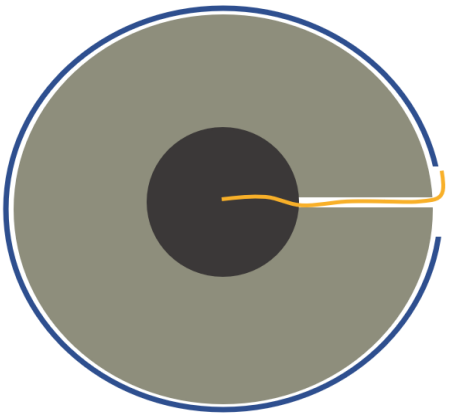

Figure 6.15: Schematic drawing of the geometry of the magnet and surrounding silicon calorimeter. An exemplary track of a recoiling electron that escapes the magnet bulk through the slit of the magnet and deposits energy in the calorimeter is drawn.

In figure 6.16 the energy deposits in the 1 mm thick silicon layer for different secondary particles from electro-nuclear interactions can be viewed. There are a few hundreds of energy deposits in the silicon calorimeter, though hit rates are much too low to be able to efficiently veto the electro-nuclear events. It is especially interesting that some secondary FLUKA electrons produce hits in the calorimeter, even though they should be absorbed by the magnet. Though a wider slit in the calorimeter compared to the magnet has reduced the electron hits. Most hits produced in the silicon layer are charged hadrons, in particular pions and protons, which is in accordance with the findings from section 6.3. It is important to remember that the magnet and thus also the silicon calorimeter only start at position $(0, 0, 0)$ cm, and does not extend in backward direction. Back scattered particles are therefore currently not considered at all and might contribute energy deposits in the silicon layer. Though the impact on the number of energy deposits is expected to be a maximum factor of 2, which is not enough to veto the elector-nuclear events efficiently.

The results for the 10 cm silicon calorimeter around the magnet are given in figure 6.17. A whole magnitude of additional hits is gained, though a majority of hits are produced by recoiling secondary FLUKA electrons that escape the magnet slit and produce a hit in the silicon layer. Due to the magnet not extending behind the target, recoiling electrons - and other secondary particles - can also deposit energy in the calorimeter if traversing the magnet perpendicular to the z axis. Hits by charged and neutral hadrons are improved massively as well. Thus the use of a thick crystal calorimeter around the magnet might be the more viable choice to improve the background rejection. This should also be tested in a full detector setup with a more final detector geometry.

For the two calorimeter scenarios the fraction of events with more than $x \cdot$ MeV of deposited energy are presented in figure 6.18, where x corresponds to the amount of energy deposited in the whole calorimeter. Almost all of the 17394 events have more than 0.1 MeV deposited energy in the calorimeter. At more than 0.5 MeV deposited energy, the fraction of events is substantially less in both scenarios. For the 1 mm thick silicon layer the number of events falls exponentially with larger thresholds, whereas the number of events for the thicker calorimeter almost has a linear behaviour (excluding the first threshold). The thicker calorimeter seems to be a much more promising option to enhance the background rejection

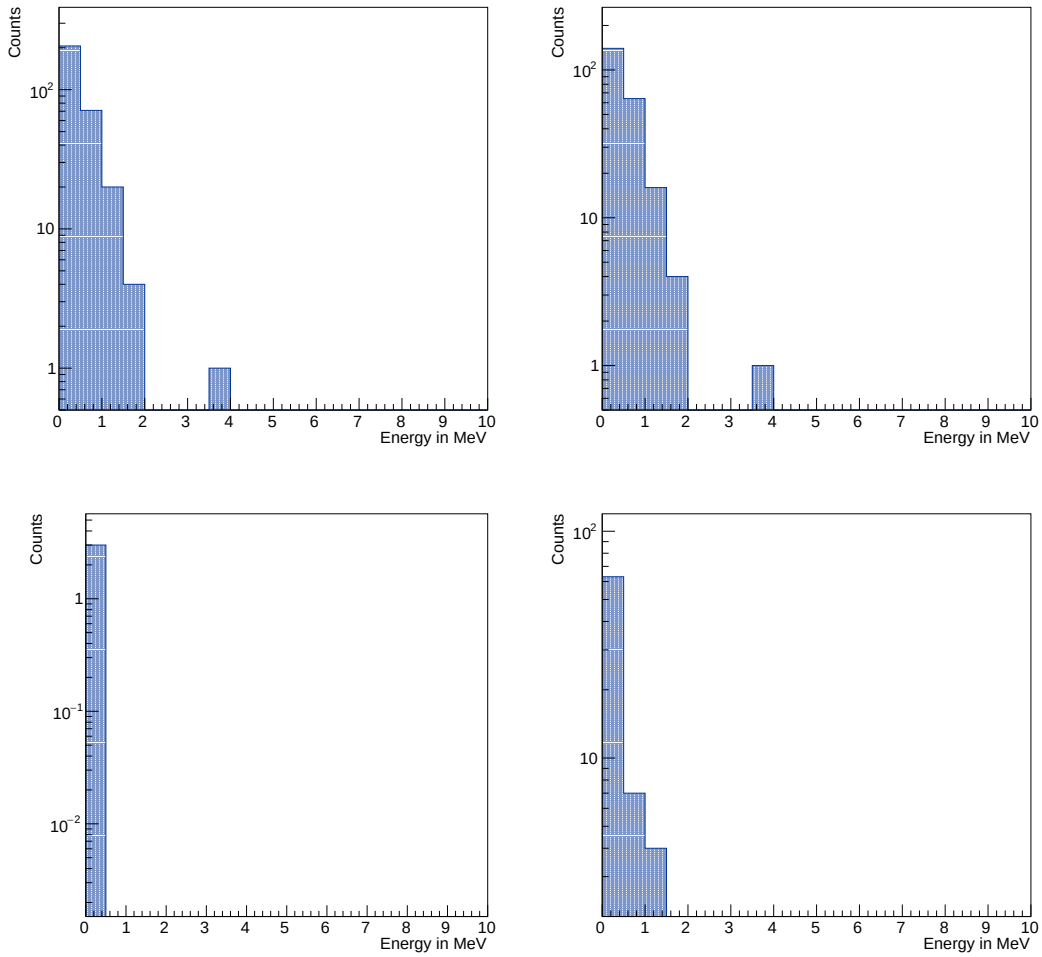

Figure 6.16: Energy deposits by all secondary FLUKA particles (top left), charged hadrons (top right), neutral hadrons (bottom left) and electrons (bottom right) in a 1 mm thick silicon layer around the magnet, for all 17394 electro-nuclear FLUKA events in the GEANT4 geometry.

of hadronic events, though still its impact is expected to be minor due to the few energy deposits.

One factor that could improve the veto efficiency of such a calorimeter around the magnet, is the reduction of the size of the magnet bulk, as could be seen in section 6.3. The simulated 30 cm thick magnet bulk is thus reduced to 20 cm and 10 cm respectively to study the impact on the amount of energy deposits in the 10 cm thick silicon sheet around the magnet. In figures 6.19 the energy deposits of all secondary FLUKA particles in the calorimeter for a 10 cm and 20 cm thick magnet are given. It is clearly visible that the amount of hits increases significantly, the thinner the magnet bulk is, which is in accordance with the results from section 6.3. The number of events with more than 0.1 MeV, 0.5 MeV, 1 MeV, 2 MeV, 5 MeV, 10 MeV, 20 MeV and 30 MeV deposited energy for the two magnet thicknesses is presented in figure 6.20. More events have a larger energy deposited in the calorimeter for the 10 cm thick magnet bulk, compared to the 20 cm thick magnet, as is to be expected. Therefore a thin magnet and a thick calorimeter around it would be the desirable combination, though the veto efficiency of the

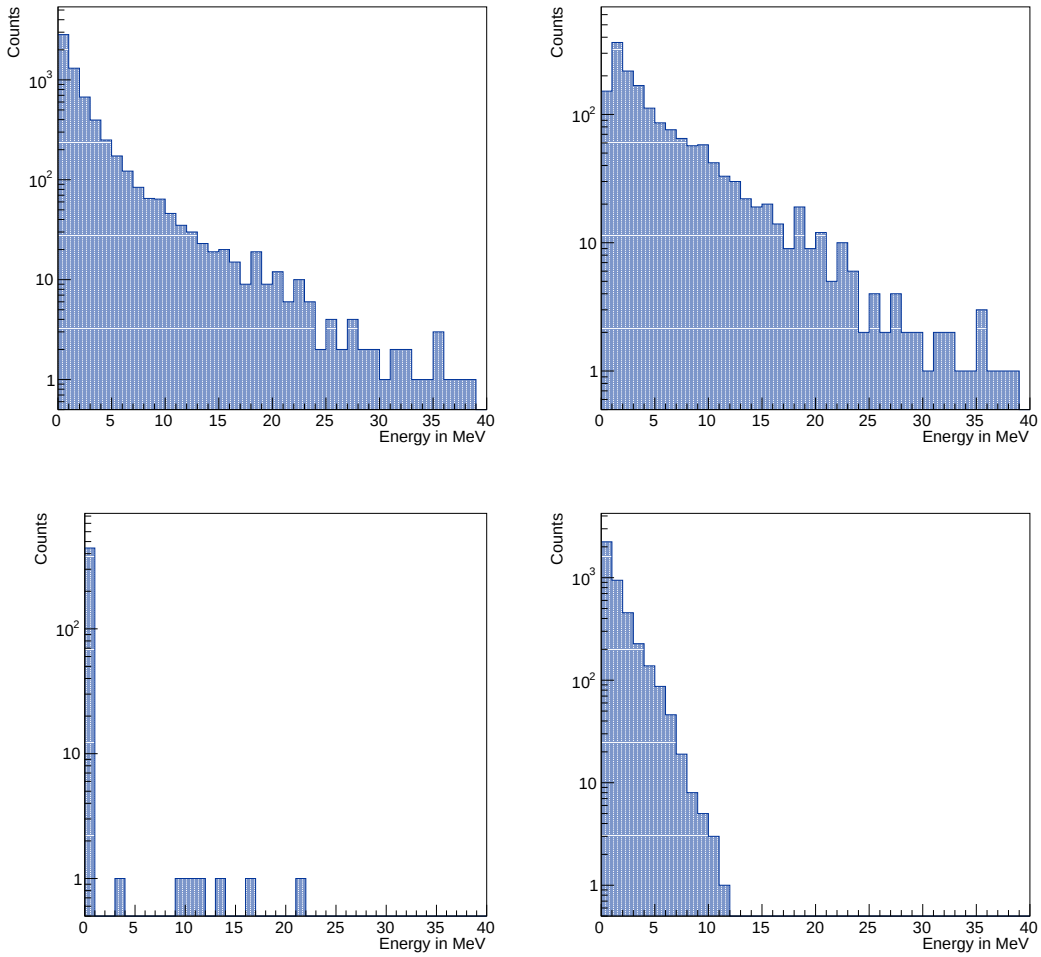

Figure 6.17: Energy deposits by all secondary FLUKA particles (top left), charged hadrons (top right), neutral hadrons (bottom left) and electrons (bottom right) in a 10 cm thick silicon layer around the magnet, for all 17394 electro-nuclear FLUKA events in the GEANT4 geometry.

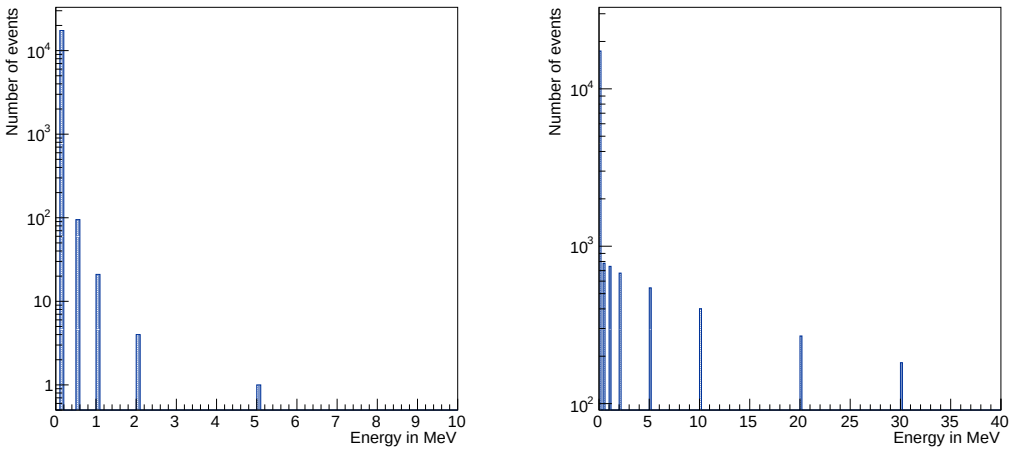

Figure 6.18: Number of events with more than 0.1 MeV, 0.5 MeV, 1 MeV, 2 MeV, 5 MeV, 10 MeV, 20 MeV and 30 MeV energy deposited in a 1 mm (left) and 10 cm (right) thick silicon layer around the magnet, for all 17394 electro-nuclear FLUKA events in the GEANT4 geometry.

events is still too low at higher energy thresholds.

Since even a calorimeter at larger angles around the magnet does not sufficiently suppress the background, the experimental setup might have to be adapted further: a shorter magnet and thus a larger opening angle could help reduce backgrounds and improve the hadronic background rejection. Though there would be less diversion of the electrons, which needs to be accounted for as well.

It is important to note that similarly to section 6.3, only the secondary FLUKA particles that deposited energy in the calorimeter were taken into account. However, the secondary FLUKA particles can produce numerous tertiary particles in the magnet bulk, which might deposit energy in the calorimeter. In a future study with the complete detector setup, this should be investigated further to rule out the significance of an additional calorimeter around the magnet regarding the hadronic background rejection.

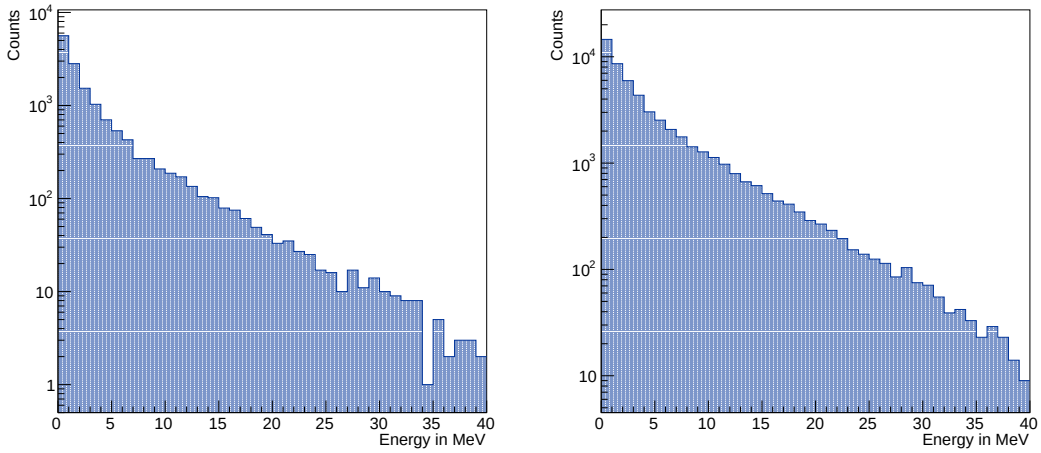

Figure 6.19: Energy deposits of secondary FLUKA particles in a 10 cm thick silicon layer around the magnet for a magnet thickness of 20 cm (left) and 10 cm (right), for all 17394 electro-nuclear FLUKA events in the GEANT4 geometry.

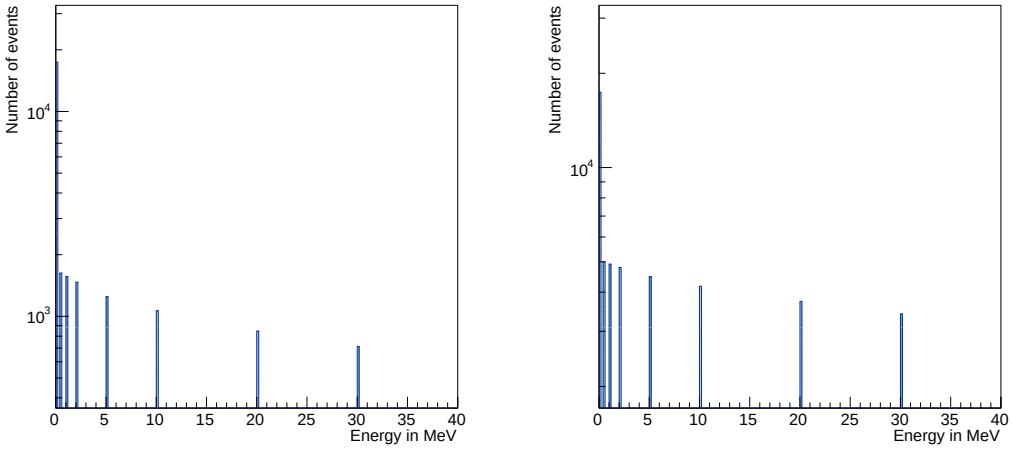

Figure 6.20: Number of events with more than 0.1 MeV, 0.5 MeV, 1 MeV, 2 MeV, 5 MeV, 10 MeV, 20 MeV and 30 MeV energy deposited in a 10 cm thick silicon layer around the magnet for a magnet thickness of 20 cm (left) and 10 cm (right), for all 17394 electro-nuclear FLUKA events in the GEANT4 geometry.

6.6 Sampling Electro-Nuclear events into constant QED Background

To study a realistic scenario of electro-nuclear backgrounds, the electro-nuclear FLUKA events need to be sampled into the constant background produced from SM QED interactions and the ability of the ECal to veto electro-nuclear interactions within the constant background is investigated. In the GEANT4 simulation each pixel in the ECal is simulated separately and all energy deposits are collected per pixel. These energy deposits are then evaluated with a separate digitization script. Assuming reading out the energy deposits of the whole ECal, the read-out is realised by integrating over the whole calorimeter. The temporal evolution of the analogue signals in the front-end ASIC is included in the simulation in order to properly model pile-up. [54]

The energy deposits in the ECal are digitized by a CRRC-shaper with the following shaping function [54, 83]:

$$A(t) = A_0 \cdot \frac{t - t_0}{\tau} \cdot e^{1-((t-t_0)/\tau)} \quad , \tag{6.4}$$

with the peak amplitude $A_0 = 6.11\,\text{mV} \cdot E_{\text{dep}}/0.09\,\text{MeV}$, the fall time constant $\tau = 30\,\text{ns}$, the time of the energy deposit t_0 and t is the time the amplitude is calculated. To take the background of SM QED photons into account, the energy deposits in a time span of $40 \cdot 30\,\text{ns} \approx 1\,200\,\text{ns}$ before the time of the electro-nuclear event are included in the read-out amplitude and the amplitude at time $t_{\text{eNuc}} + \tau$ is calculated per event. All incoming signals in each pixel in this time span are added to the total amplitude of the calorimeter and if this amplitude exceeds 20 MeV, then the event is vetoed. The energy deposition of approximately 20 MeV in the sensitive material of the calorimeter corresponds to a high-energy $O(640\,\text{MeV})$ particle depositing energy in the ECal, since a majority of the particles energy is lost in the absorber material [5].

To visualize the digitization process a simple example is presented in figure 6.21. A single pixel has two energy deposits separated by 10 ns: the first energy deposit is at 40 ns and deposits 0.9 MeV and the second event deposits 2.7 MeV at time 50 ns. The energy deposits are converted to mV via $A_0 = 6.11\,\text{mV} \cdot E_{\text{dep}}/0.09\,\text{MeV}$. For the first event the amplitude at $t_1 + 30\,\text{ns} = 70\,\text{ns}$ is read-out and assigned to that event. The much larger energy deposit in the second event results in a larger assigned amplitude for the first event. For the LOHENGRIN experiment this is a crucial property of the read-out system, because there are constant energy deposits in the ECal from SM QED interactions in the target and in theory only rare high-energy deposits by electro-nuclear secondaries. Therefore the high-energy signal must exceed the amplitude of the constant background to veto such events. Inversely, if there is only a small energy deposit or no energy deposit by an electro-nuclear interaction, it is interesting to know how likely it is that the constant SM QED background events cause a veto.

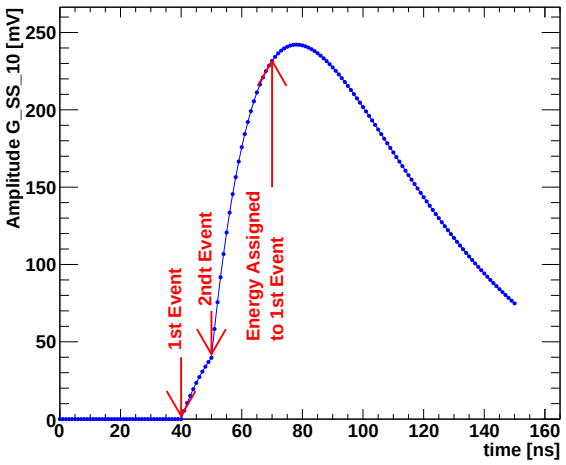

Figure 6.21: Visualized amplitude for a single pixel and two energy deposits at time 40 ns and 50 ns. The amplitude is read-out for the first event. Taken from [54].

Before the digitization algorithm can be applied to the energy deposits in the calorimeter, the electro-nuclear events need to be added to the QED background: A sample of $8 \cdot 10^5$ SM QED events is used [54] and the 17394 electro-nuclear events analysed in the previous sections are sampled into these background processes. The electro-nuclear events all have recoiling electrons in the signal region, so with an energy $25\,\text{MeV} < E_{\text{recoil}} < 75\,\text{MeV}$ and angle $\theta_{\text{recoil}} < 0.2\,\text{rad}$. The following sampling algorithm is applied:

- For 600 ns, QED events are randomly chosen from the sample of 8×10^5 events. The probability for taking one such event is a Poisson distribution with expectation value of 0.2. This results in roughly 60 QED events.
- Then one of the electro-nuclear FLUKA event is placed.
- To account for the falling edge of the digitization of the ECal, an additional 50 ns interval is added with random QED events, which results in roughly 5 events.
- This loop is repeated in 2 ns steps until all electro-nuclear events are sampled.
- In total 1149859 events are generated.

This sampling algorithm is based on the extraction times at ELSA and the long tail of the amplitude spectrum of the digitized energy depositions in the ECal. This way each electro-nuclear event has sufficiently many background signals before and after to study the digitization of the ECal and the impact of the constant background.

The generated file can be read into GEANT4 and the particles are placed into the target, similarly to the previous sections. To take the Gaussian beam profile into account, the particles are again placed at the center of the target $(0, 0, -0.1752)$ and then smeared via a Gaussian with standard deviation of 1 mm in x- and y-direction. The start of each event is then determined by evaluating a Poisson distribution with expectation value 0.2 every 2 ns. The number of events from the sample resulting from the Poisson distribution are started and the particles are propagated through the setup.

Each event is then handled by GEANT4 and all hit times and energy depositions in the HCal and ECal are collected, together with the starting time of each event. The analysis of energy deposits in the ECal is no longer done on event basis, but using the amplitude function given in equation 6.4. For each electro-nuclear event at time t the amplitude $A(t)$ is evaluated, taking energy deposits in the time span $t - 1\,200\,\text{ns}$ into account.

If the amplitude does not exceed the 20 MeV threshold, the HCal is checked in addition for any significant energy deposits in the event. Since it is assumed that there is no constant background in the HCal, it would be sufficient to veto events with any energy deposits in the HCal. Therefore energy deposits in the HCal are collected on event by event basis and if the energy deposits exceed a certain value, e.g. 10 MeV, then the HCal can veto the event. If either the ECal or the HCal trigger, the event is vetoed. Any events left afterwards contribute to the irreducible background with the current detector setup. It is important to note that the instantaneous read-out of the HCal is only an approximation and the actual read-out of the HCal is not yet fully developed or realized. In future studies the need for a similar digitization model as explained above needs to be investigated and developed.

The collected hits in the ECal and HCal for the sampled electro-nuclear and SM QED data is given in figure 6.22. As expected, the ECal has a distinct spot in the center, caused by photons emerging from SM bremsstrahlung in the target [5]. The ECal is designed to contain the whole electromagnetic shower initiated by high-energy particles. However, it is clearly visible from the many hits in the center of the HCal, that showers leak from the ECal into the HCal, which shows that the ECal is currently not thick enough. This type of leakage is easily fixed by building a thicker ECal with additional layers. In figure 6.23 the layer in the ECal and position z in the HCal are given for each energy deposit by secondary and tertiary particles. Since the longitudinal shower profile is cut-off at the end for both calorimeters, leakages into the HCal are to be expected. To test the reduction of the leakage into the center of the HCal by the SM QED processes, the simulation of the detector setup was repeated for different ECal thicknesses. In figure 6.24 the hit collections in the HCal for a 20 and 50 layer ECal are given. The ECal is therefore 20.7 cm and 51.75 cm long for the 20 and 50 layers respectively. It is visible by the loss of statistics that the number of hits in the HCal can be reduced drastically by adding layers to the ECal. Whether or not this is realisable and how the ECal will be built is not set at this point. In a future technical study of the calorimeters this could be investigated further and extensions of the calorimeters might be taken into account. Additionally a digitization procedure for the HCal might have to be developed to not veto events due to leakages from the ECal. Since the HCal hits are evaluated on event basis at this point, leakage effects from SM QED processes are not considered when using the HCal as a veto.

The strip of hits on the left side of the ECal in the HCal is caused by positrons from the SM QED sample. They are created through pair production of photons in the target and are deflected towards the negative x axis by the magnetic field. The corresponding electron is not visible due to the slit in the HCal and they would be absorbed by the shadow of the much larger beam of electrons regardless.

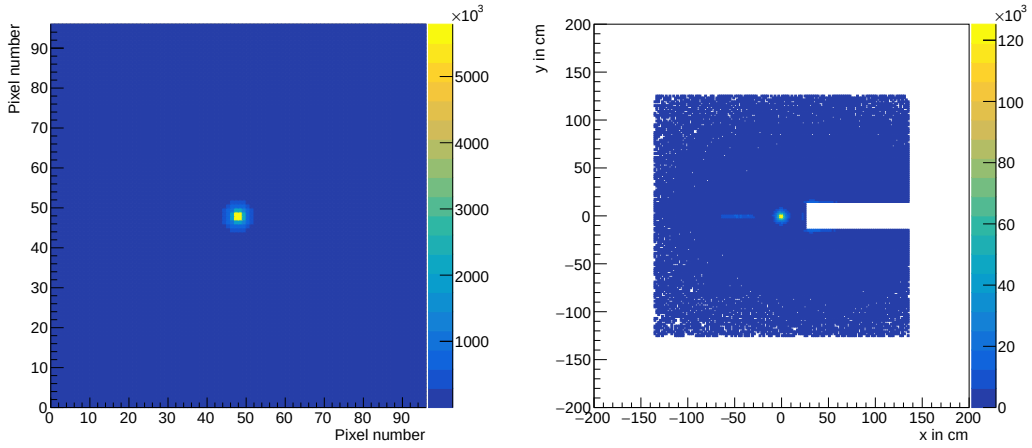

Figure 6.22: Hit collections in the pixels of the ECal (left) and positions in the HCal (right) for the sampled electro-nuclear and SM QED data in the GEANT4 geometry.

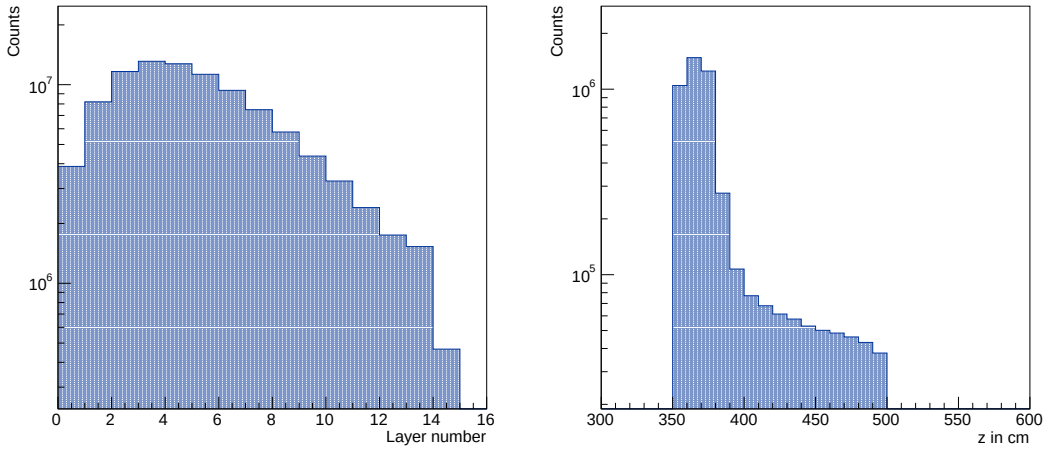

Figure 6.23: Collected hit layer in the ECal (left) and position in z HCal (right) for the sampled electro-nuclear and SM QED data in the GEANT4 geometry.

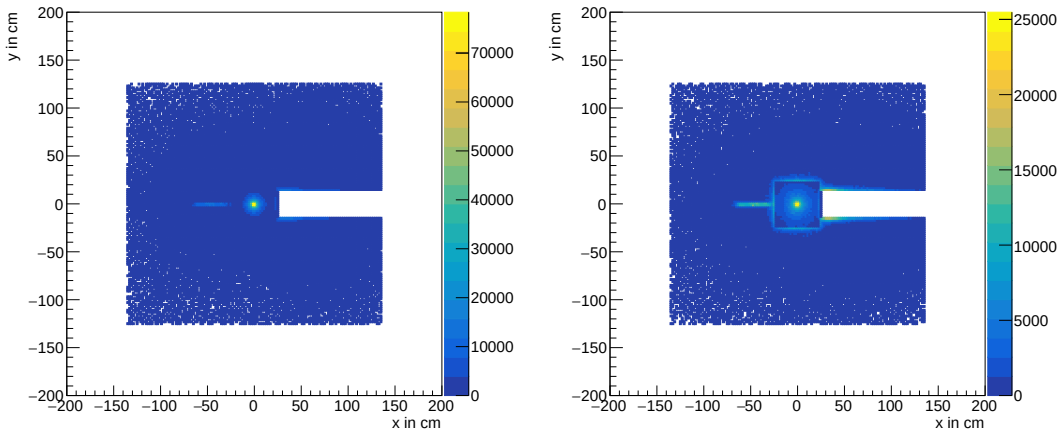

Figure 6.24: Hit collections in the HCal for a 20 layer ECal (left) and a 50 layer ECal (right), using the sampled data in the GEANT4 geometry.

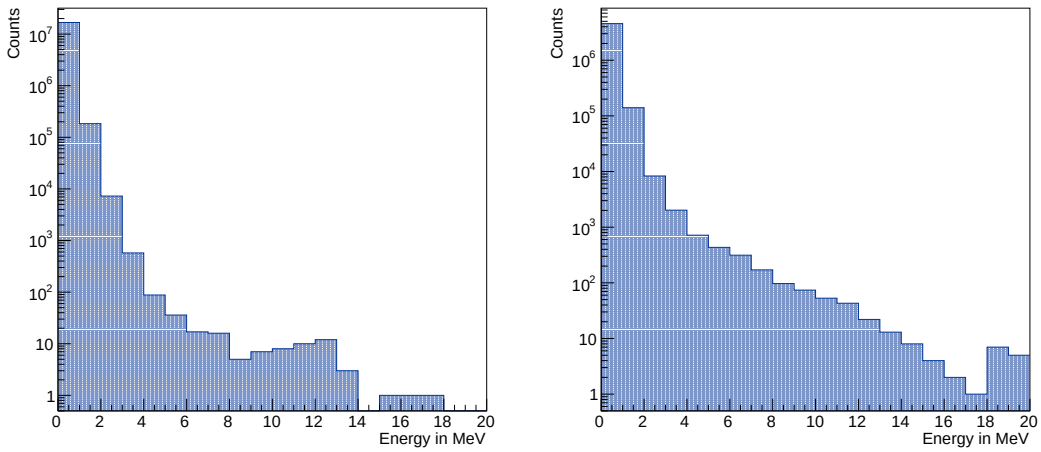

Figure 6.25: Energy deposits in the ECal (left) and HCal (right) for the sampled electro-nuclear and SM QED data in the GEANT4 geometry.

Most important for this analysis are the energy deposits in the calorimeters, which are given in figure 6.25. The distributions look similar to the energy distributions of the previous sections, though slightly shifted towards larger energies. As expected, most energy deposits in the calorimeters are below 20 MeV. These energy deposits are read into the digitization algorithm for the ECal and the number of events exceeding the threshold amplitude are recorded. In the previous sections only approximately 30 % of the electro-nuclear events could be vetoed and for the digitisation algorithm a similar number of vetoed events is expected. Though some of the electro-nuclear events might be vetoed due to the energy deposits of the SM QED background previously to the time of the event.

In figure 6.26 the calculated amplitudes for all electro-nuclear events with the digitization algorithm described above can be viewed. As expected from the previous sections, most of the electro-nuclear events have small energy deposits. In table 6.6 the number of vetoed events by the two calorimeters and the total amount of vetoed events is presented for different energy thresholds in the HCal. As explained above, the ECal threshold is set to 20 MeV, which corresponds to, e.g. a high-energy photon that deposits energy.

As expected, the varying threshold in the HCal changes the number of vetoed events. For smaller thresholds more events can be vetoed by the HCal, compared to a larger threshold. With a minimal threshold of 1 MeV the HCal vetoes 3947 electro-nuclear events, which is in accordance with the previous section, where the ECal and HCal combined vetoed 4959 events for this threshold. This similar result is to be expected, since the HCal is evaluated on event basis in both cases.

Due to the constant background from SM QED interactions in the ECal, it is expected that some of the electro-nuclear events are vetoed, because the energy deposits of the SM QED background in addition to the energy deposits by electro-nuclear events exceed the 20 MeV [54]. The simulation of the sampled data in the GEANT4 detector setup resulted in 6068 out of 17394 events - so 35 % - to be vetoed by the ECal, even though the previous sections have shown that only minimal energy is deposited in the ECal. This pile-up effect is to be expected and the amount of vetoed events correspond to the expectations [54].

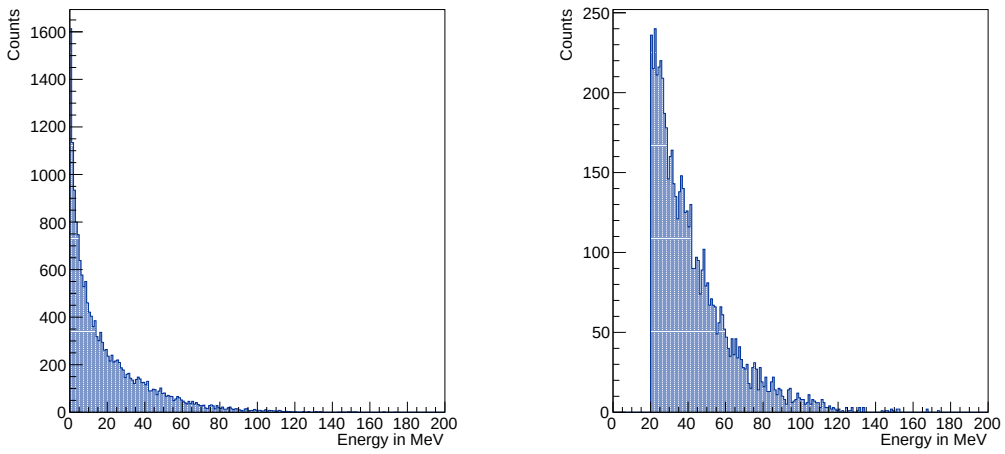

Figure 6.26: The amplitude calculated with the digitization algorithm at the time of each electro-nuclear event in the sample (left) and events that pass the minimum cut of 20 MeV (right).

Table 6.6: Number of vetoed events by the ECal, HCal and in total for the sampled data in the GEANT4 geometry and digitised energy deposits in the ECal. Different thresholds for the HCal are applied.

HCal Energy deposited	ECal vetoed	HCal vetoed	Total
100 MeV	6068	272	6239
50 MeV	6068	905	6646
10 MeV	6068	2490	7693
1 MeV	6068	3947	8640

6.7 Summary

In this chapter the electro-nuclear secondary particles from the FLUKA event generator were placed and propagated in a simplified detector setup of the LOHENGRIN experiment and the detector response and veto strategy analysed. A simplified detector setup including the magnet, magnetic field and the electromagnetic and hadronic calorimeters was implemented and tested in the GEANT4 simulation framework. From the energy deposits in the calorimeters only a 32 % background rejection of electro-nuclear FLUKA events with a signal-like electron could be reached, confirming the results of the event selection applied in the previous chapter. Additionally it was presented that only a small fraction 0.002 of secondary FLUKA particles deposit energy in the HCal and even less 0.0008 deposit energy in the ECal. Thus detecting and efficiently rejecting electro-nuclear hadronic backgrounds with the current veto strategy is not possible. This lead to a total of $1.9 \cdot 10^6$ hadronic background events in the signal region of the LOHENGRIN experiment, leading to the insensitivity to detect dark photons with the current detector setup.

An alternative veto strategy has been tested with a silicon calorimeter around the magnet. A thin silicon calorimeter does not have the ability to sufficiently veto hadronic backgrounds, though a thicker calorimeter and a thinner magnet provide a more viable option. This could be investigated in more detail in a full simulation of the detector setup. However, the rearranging of the full detector setup seems like the more promising option. This could be realised using a shorter magnet or placing the target further downstream in the magnet, such that the calorimeters cover a larger angle.

In the last section the electro-nuclear FLUKA events were sampled into the constant SM QED background expected at the LOHENGRIN experiment to study the veto efficiency of the ECal. A digitization algorithm was applied to the energy deposits in each pixel in the ECal and the number of vetoed events discussed. Since the ECal has the constant energy deposits from the SM QED processes in addition to potential energy deposits from electro-nuclear interactions, it is expected that some of the electro-nuclear events are vetoed due to the constant background. The reason is that the energy deposits by SM QED processes before the time of the electro-nuclear events also contribute to the total amplitude during the digitization process, causing the amplitude to exceed the set 20 MeV cut and thus vetoing the event. This could be reproduced with the simulations with the ECal vetoing about 35 % of the electro-nuclear events, which corresponds to the expected amount [54]. Since the electro-nuclear events deposited only minimal energy in the ECal, this study should be repeated in a future simulation of the detector setup to determine the energy threshold to high precision, such that high-energy particles from electro-nuclear interactions are vetoed efficiently and the SM QED background stays below the threshold.

CHAPTER 7

Conclusion and Outlook

In this thesis the LOHENGRIN experiment has been introduced as a future experiment at the ELSA accelerator at the university of Bonn. It aims to probe the Light Dark Matter sector with the fundamental process of dark bremsstrahlung. The hadronic backgrounds produced via electro-nuclear interactions are one important factor for the sensitivity of the experiment and were therefore investigated.

In first tests of electro-nuclear interactions in the simulation framework GEANT4, two bugs have been found in the source code, causing a violation of momentum conservation. While these could be fixed, an additional issue with the kinematics of electro-nuclear interactions in the LOHENGRIN signal region was found: at momentum transfers above 94 % of the incident electron to the virtual photon, the electro-nuclear simulation in GEANT4 does not reliably simulate the kinematics.

FLUKA was investigated as an alternative event generator for the LOHENGRIN experiment. Electro-nuclear interactions were studied in more detail and resulted in electro-nuclear secondaries being dominated by low-energy photons and hadrons that are isotropically distributed. There are only few high-energy secondary particles per electro-nuclear interaction, and even the high-energy secondaries obtain large angles and are not exclusively radiated in forward direction. In addition the target material was investigated using FLUKA regarding its impact on the distributions of electro-nuclear secondary particles. For the fermionic ^{183}W isotope, no systematic difference to the target made up of the bosonic isotope ^{184}W could be found. Impurities in the target of up to 5 % also do not significantly alter the result. Additionally photo-nuclear interactions were compared to electro-nuclear interactions and it was confirmed that the secondary distributions are similar. As expected, there are substantially more secondary hadrons and photons for photo-nuclear interactions compared to electro-nuclear interactions at the same energies of the incident photon and electron. Finally in this chapter, an event selection was applied to the MC truth data in FLUKA. Different selection criteria resulted in $O(10^3 - 10^6)$ hadronic background events in the signal region for $4 \cdot 10^{14}$ e.o.t. for LOHENGRIN.

However, only MC truth data has been analysed and investigated to this point and particle transportation and detector responses have not been taken into account. Thus a detector simulation containing the hadronic and electromagnetic calorimeter, the magnet and magnetic field has been implemented in GEANT4 and the secondary particles from the FLUKA simulation placed at the position of the target. From an analysis of energy deposits in the calorimeters on an event by event basis, again only 5526 out of 17394 electro-nuclear events with signal-like electrons could be vetoed. Extrapolating this to the actual number of electrons on target, it leaves $1.9 \cdot 10^6$ hadronic background events from electro-nuclear interactions in the signal region. Therefore the current veto strategy does not efficiently reject hadronic

backgrounds and must be adapted in the future to maintain sensitivity to dark matter models.

While electro-nuclear interactions pose a larger challenge to the current veto strategy than assumed [5] and the experiment will not be able to detect dark photons with the current detector setup, there are modifications to the detector setup that can possibly restore the sensitivity of the experiment. One idea would be to further investigate the impact of an additional veto calorimeter around the magnet. Another alternative is moving the target to the back of the magnet and thus obtain an enlarged angular coverage of the calorimeters or installing additional sensitive layers inside the magnet bulk. The tracking planes are also a substantial part of the detector setup and add a veto layer, by rejecting any event with more than one charged track in either the initial or final state. They have not been implemented or considered in this thesis and thus it is expected that the hadronic backgrounds from electro-nuclear interactions can be reduced substantially with the tracking planes.

In a future study with the full detector setup, electro-nuclear backgrounds and other backgrounds, such as neutrino or photo-nuclear backgrounds produced in other detector materials, can be investigated and the results of this thesis hopefully can be verified. Additional detector investigations, such as the digitization for the calorimeters needs to be studied and calibrated and studies of leakages of particle showers into the HCal and the likelihood to veto events due to leakages could be conducted.

It would also be very interesting to put these simulations to the test experimentally and measure hadronic backgrounds. This is planned to take place in phase two of the LOHENGRIN experiment. In the first phase extensive background tests without a hadronic calorimeter are to be done. This way the impact of virtual Compton scattering (VCS) and the SM QED backgrounds can be better understood and calibrated. Then, in phase two the hadronic calorimeter is added to the setup to probe the hadronic backgrounds. And lastly in phase three a physics run with $4 \cdot 10^{14}$ e.o.t. and the full detector setup will be conducted. [5] Though until then the detector setup needs to be adapted to efficiently reject electro- - and possibly - photo-nuclear backgrounds.

While this thesis was not able to fully answer the fundamental question:

What are we and the universe around us made of? ,

it could contribute to the design and study of hadronic backgrounds produced via electro-nuclear interactions at the LOHENGRIN experiment, which in turn one day might be able to probe the light dark matter sector for physics beyond the Standard Model and get physicists around the world one step closer to the complete answer.

APPENDIX A

Appendix

A.1 Implementing an Enhancement factor in GEANT4

To obtain more statistics an enhancement factor (EF) is implemented into the Geant4 simulation using the custom physics list explained in section 4.4. This simply multiplies the cross section for electro-nuclear interactions by a user-defined factor. The idea is to save computation time and concentrate on the processes of interest. In figures A.1 to A.5 the results for a GEANT4 simulation with and without the enhancement factor are compared. Since the overall distributions are the same, the enhancement factor can be used to obtain more statistics more efficiently.

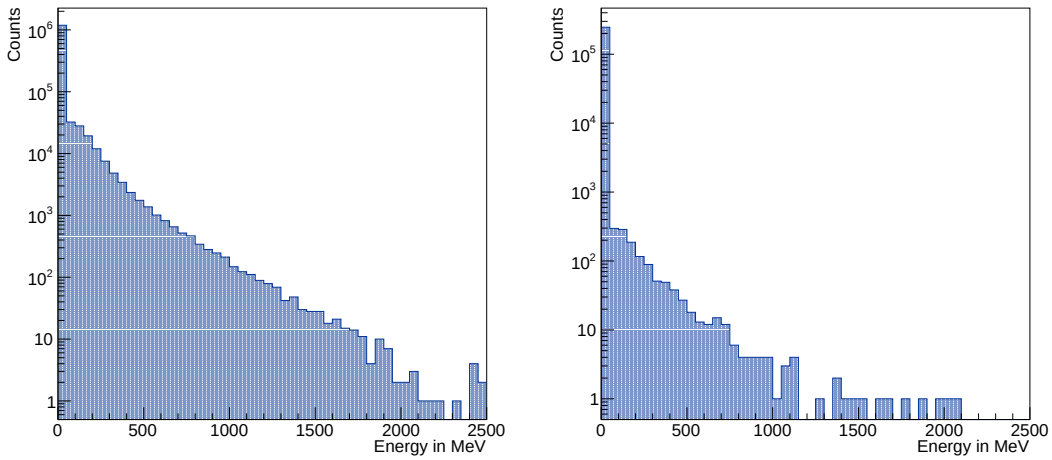

Figure A.1: Secondary photon energy of electro-nuclear interactions for 100 runs of $5 \cdot 10^5$ e.o.t. and $EF_{EN} = 10^4$ (left) and 1000 runs of $5 \cdot 10^6$ e.o.t. and $EF_{EN} = 1$ (right).

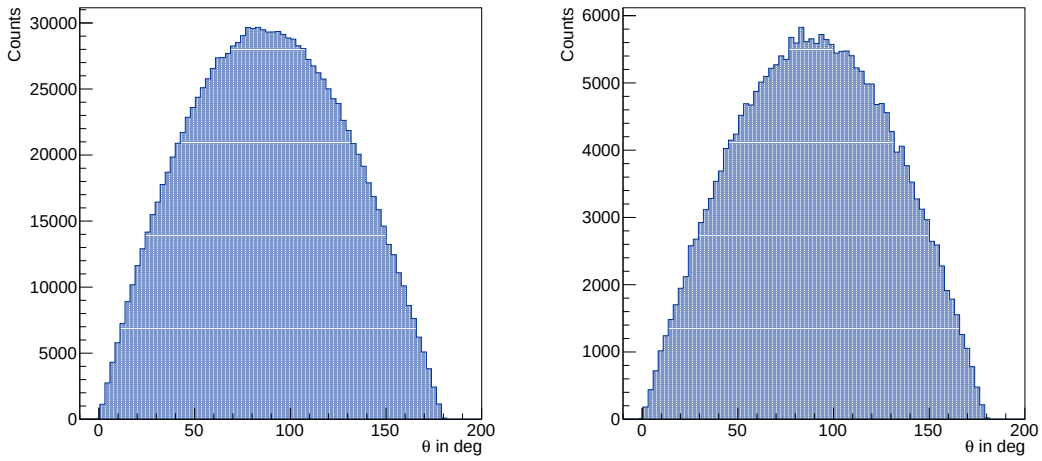

Figure A.2: Secondary photon angle θ of electro-nuclear interactions for 100 runs of $5 \cdot 10^5$ e.o.t. and $EF_{EN} = 10^4$ (left) and 1000 runs of $5 \cdot 10^6$ e.o.t. and $EF_{EN} = 1$ (right).

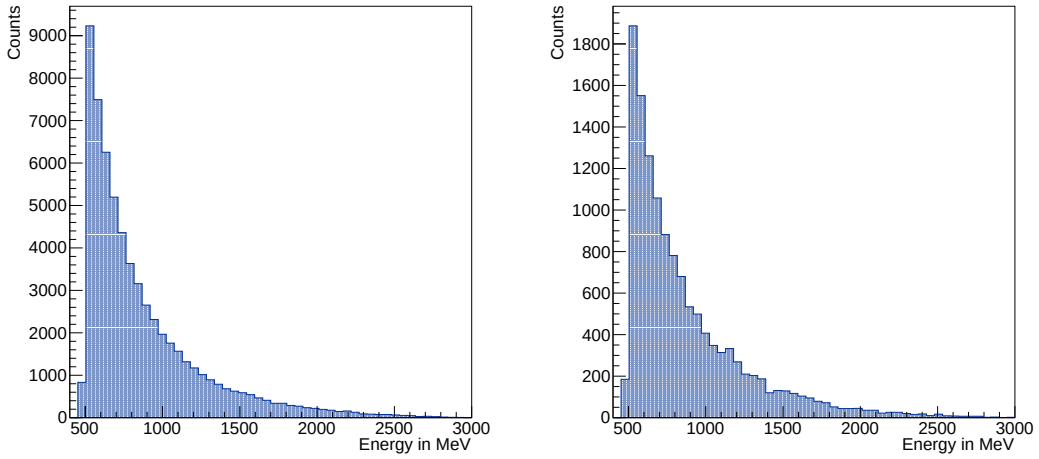

Figure A.3: Secondary hadron energy of electro-nuclear interactions for 100 runs of $5 \cdot 10^5$ e.o.t. and $EF_{EN} = 10^4$ (left) and 1000 runs of $5 \cdot 10^6$ e.o.t. and $EF_{EN} = 1$ (right). Only hadrons with more than 500 MeV are selected.

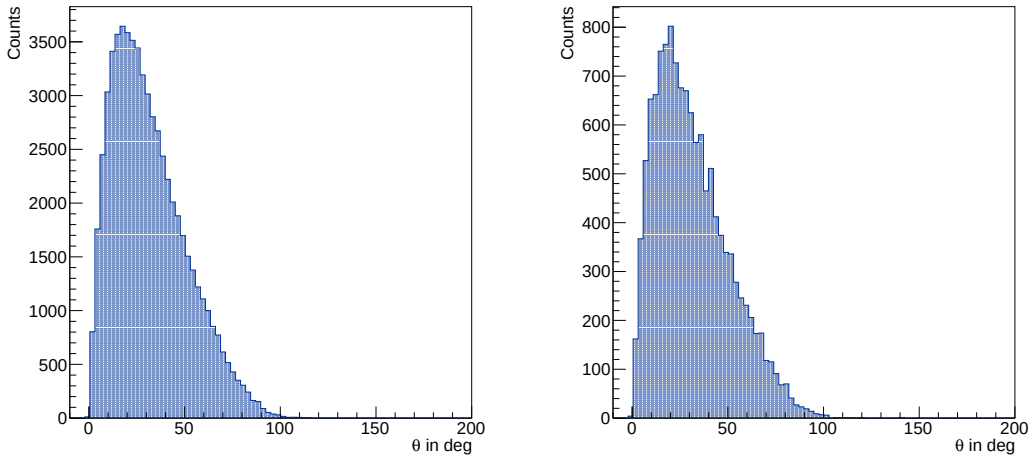

Figure A.4: Secondary hadron energy of electro-nuclear interactions for 100 runs of $5 \cdot 10^5$ e.o.t. and $EF_{EN} = 10^4$ (left) and 1000 runs of $5 \cdot 10^6$ e.o.t. and $EF_{EN} = 1$ (right). Only hadrons with more than 500 MeV are selected.

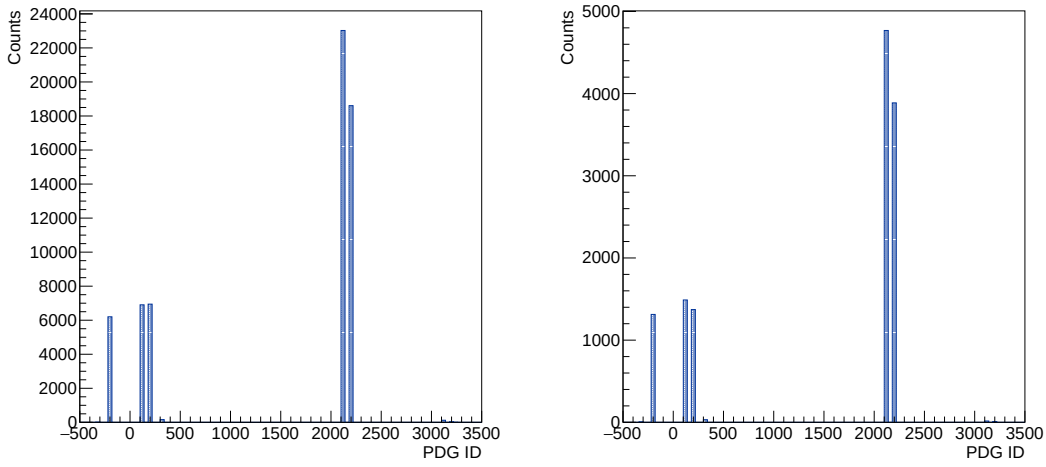

Figure A.5: Secondary hadron PDG particle numbers of electro-nuclear interactions for 100 runs of $5 \cdot 10^5$ e.o.t. and $EF_{EN} = 10^4$ (left) and 1000 runs of $5 \cdot 10^6$ e.o.t. and $EF_{EN} = 1$ (right).

A.2 4-Momentum Conservation in FLUKA

To double check that FLUKA conserves energy and momentum, the total momentum and energy of electro-nuclear secondaries per event subtracted from the electron momentum and energy before the electro-nuclear interaction is provided in a histogram. In figure A.6 the momentum conservation in p_x, p_y and p_z is given. The precision in p_x is 10^{-15}, p_y is 10^{-14} and p_z is 10^{-13}, which corresponds to floating point precision. For energy conservation the histogram is given in figure A.7 and also corresponds to zero with a precision of 10^{-11}.

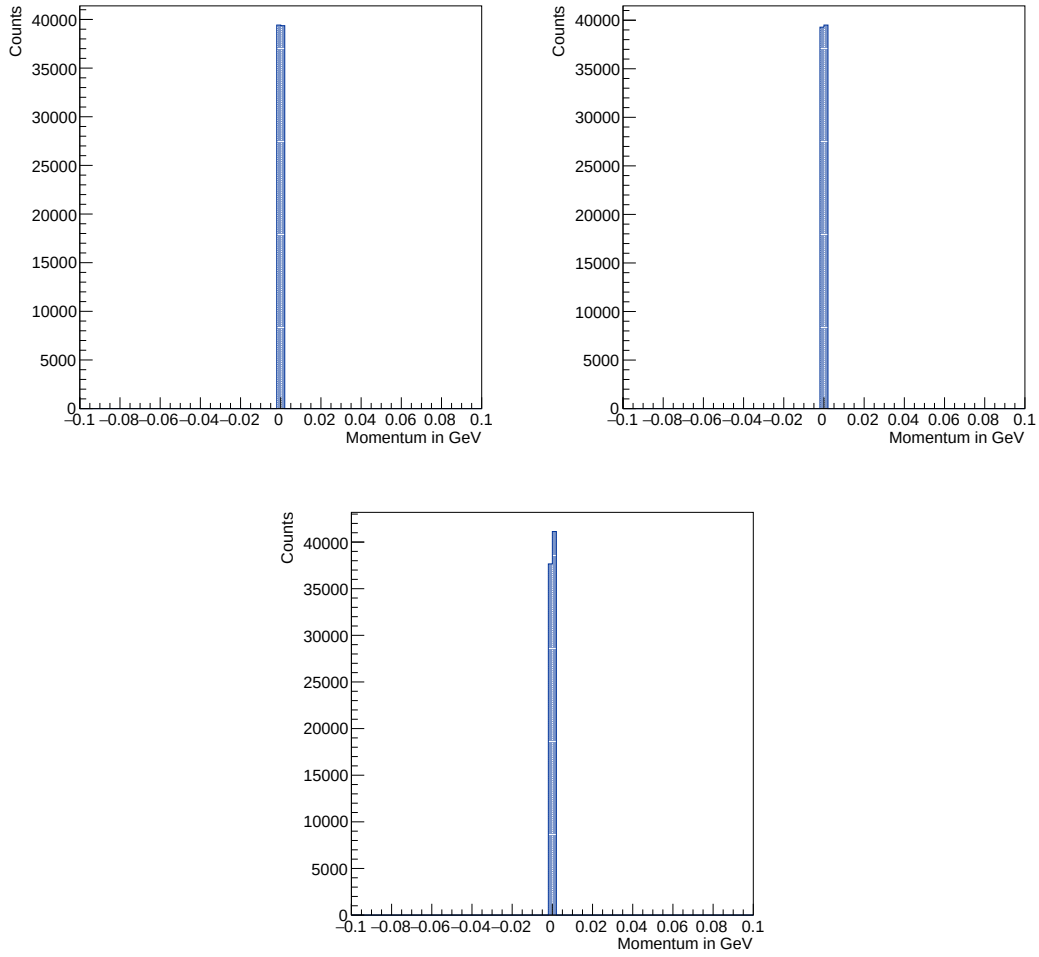

Figure A.6: Momentum conservation for p_x, p_y and p_z for a FLUKA simulation with $2.5 \cdot 10^9$ electrons on target.

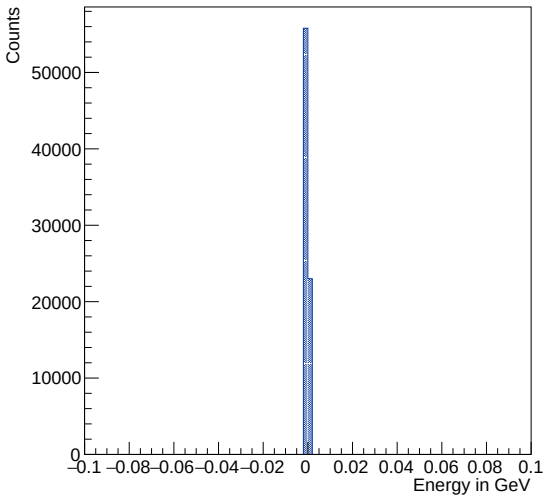

Figure A.7: Energy conservation for a FLUKA simulation with $2.5 \cdot 10^9$ electrons on target.

A.3 Electro- vs. Photo-nuclear interactions in FLUKA

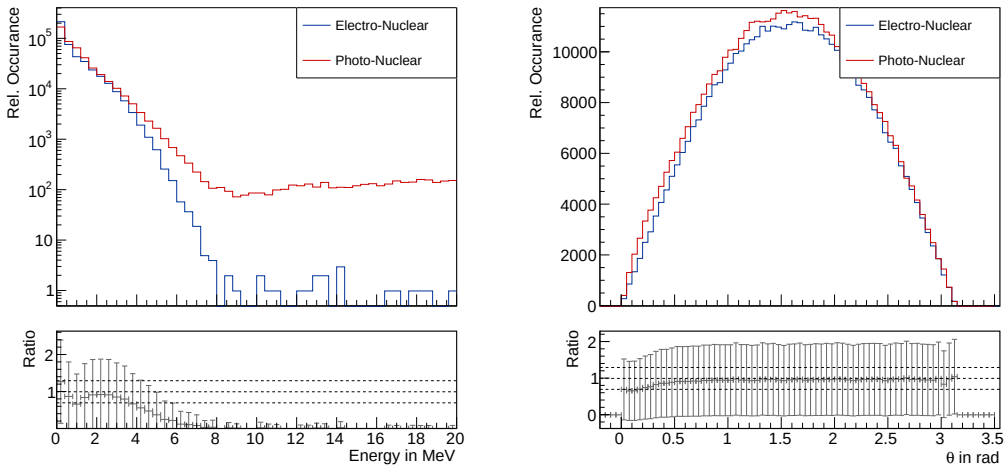

Figure A.8: Energy (left) and θ (right) of secondary photons for a FLUKA simulation with $2.5 \cdot 10^9$ e.o.t. comparing electro-nuclear processes and photo-nuclear processes.

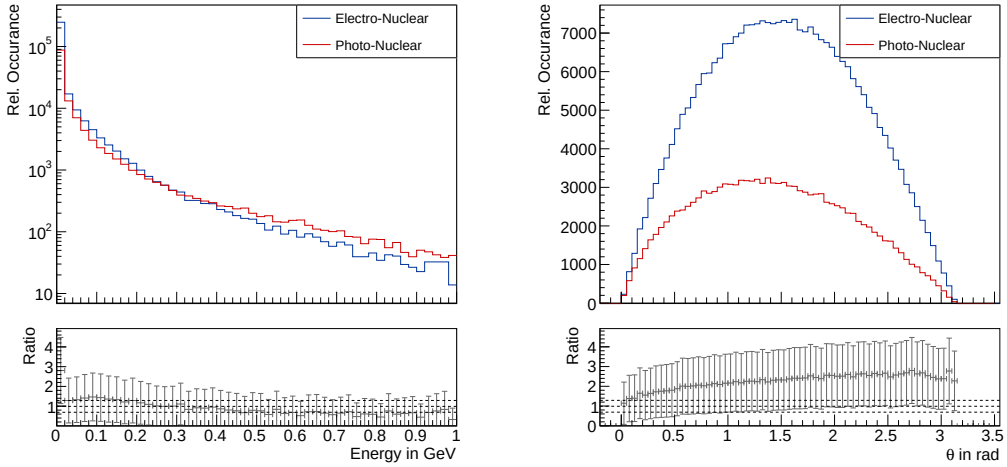

Figure A.9: Energy (left) and θ (right) of secondary hadrons for a FLUKA simulation with $2.5 \cdot 10^9$ e.o.t. comparing electro-nuclear processes and photo-nuclear processes.

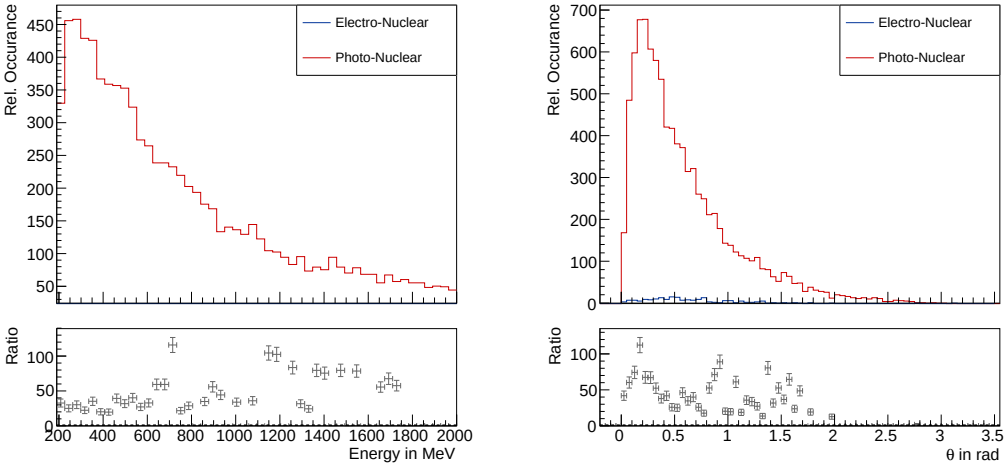

Figure A.10: Energy (left) and θ (right) of secondary photons with applied energy cut for a FLUKA simulation with $2.5 \cdot 10^9$ e.o.t. comparing electro-nuclear processes and photo-nuclear processes.

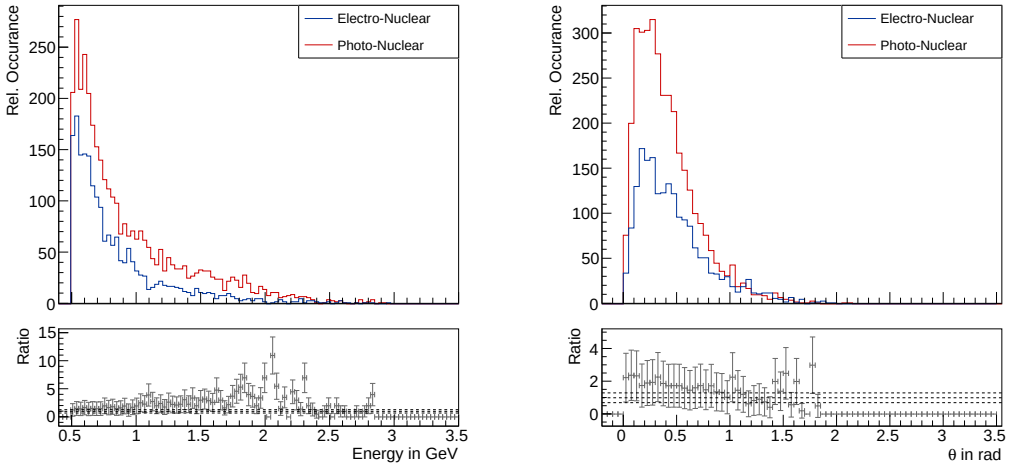

Figure A.11: Energy (left) and θ (right) of secondary hadrons with applied energy cut for a FLUKA simulation with $2.5 \cdot 10^9$ e.o.t. comparing electro-nuclear processes and photo-nuclear processes.

A.4 Event Selection in FLUKA

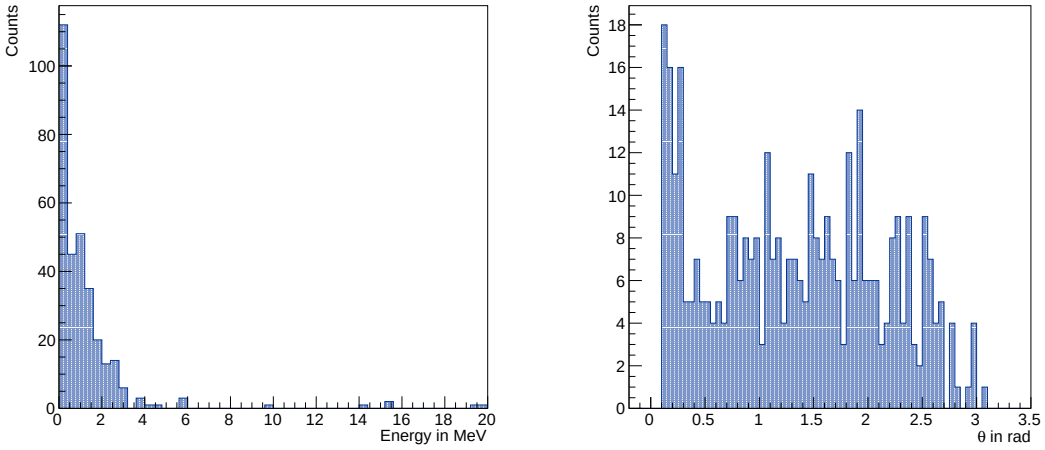

Figure A.12: Secondary photon energies and θ for a FLUKA run with $2.5 \cdot 10^{12}$ e.o.t. and applied event selection (2).

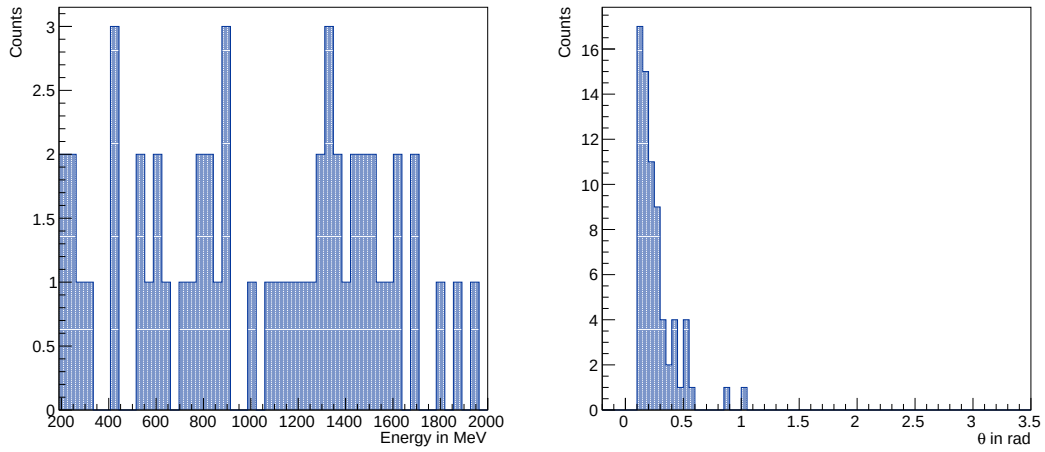

Figure A.13: Secondary photon energies above 200 MeV and corresponding angles θ for a FLUKA run with $2.5 \cdot 10^{12}$ e.o.t. and applied event selection (2).

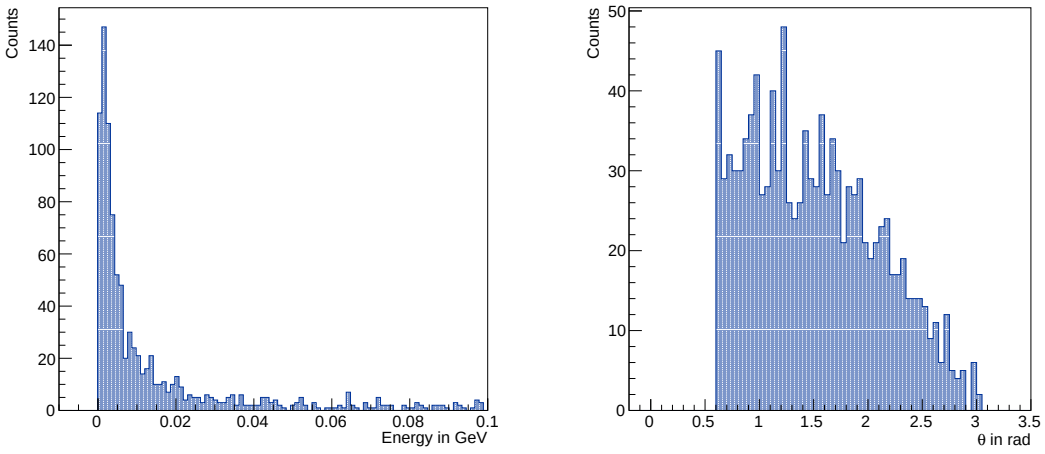

Figure A.14: Secondary hadron energies and θ for a FLUKA run with $2.5 \cdot 10^{12}$ e.o.t. and applied event selection (2).

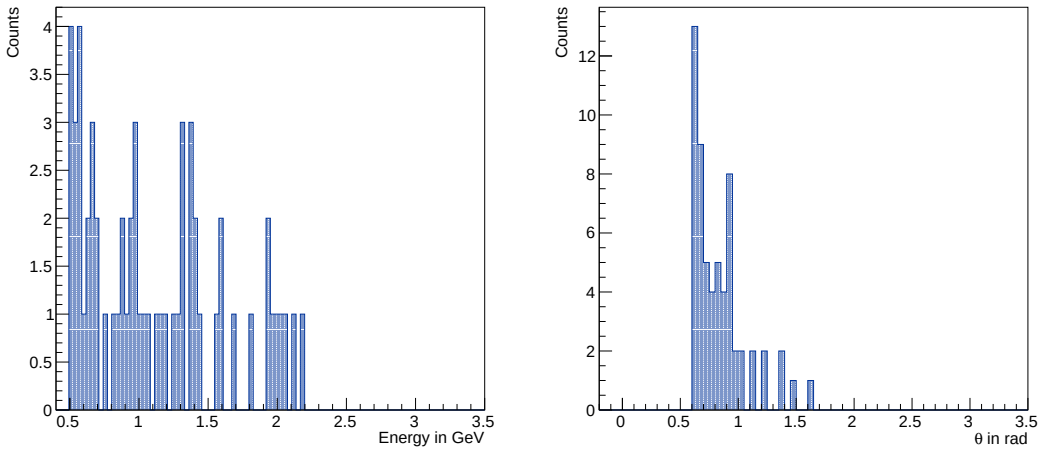

Figure A.15: Secondary hadron energies above 500 MeV and corresponding angles θ for a FLUKA run with $2.5 \cdot 10^{12}$ e.o.t. and applied event selection (2).

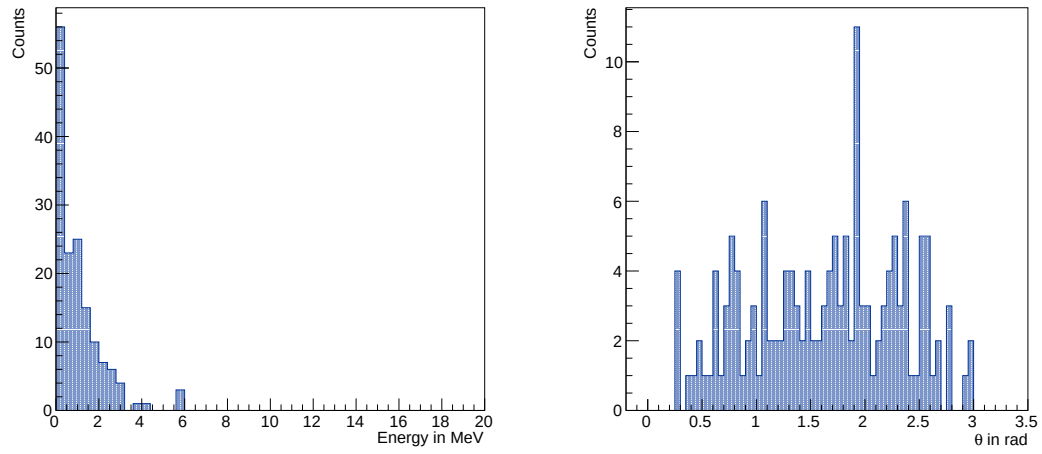

Figure A.16: Secondary photon energies and θ for a FLUKA run with $2.5 \cdot 10^{12}$ e.o.t. and applied event selection (3).

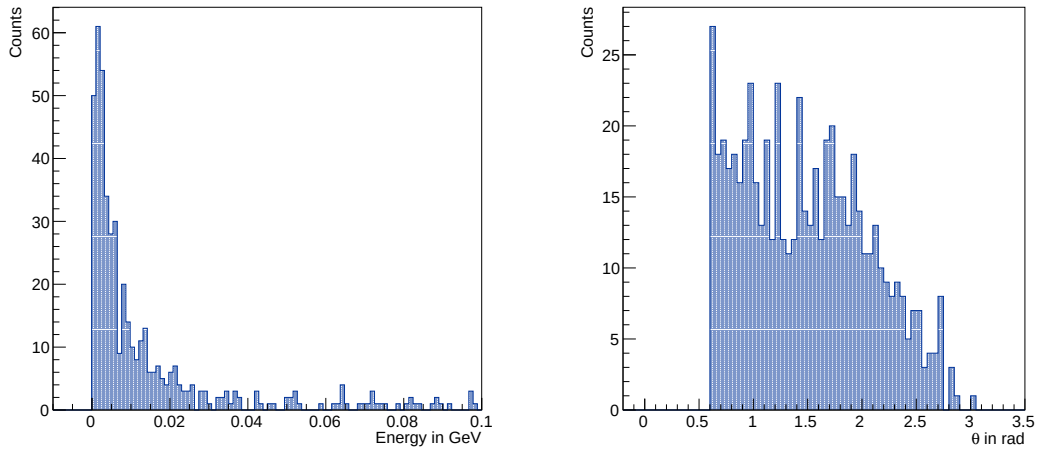

Figure A.17: Secondary hadron energies and θ for a FLUKA run with $2.5 \cdot 10^{12}$ e.o.t. and applied event selection (3).

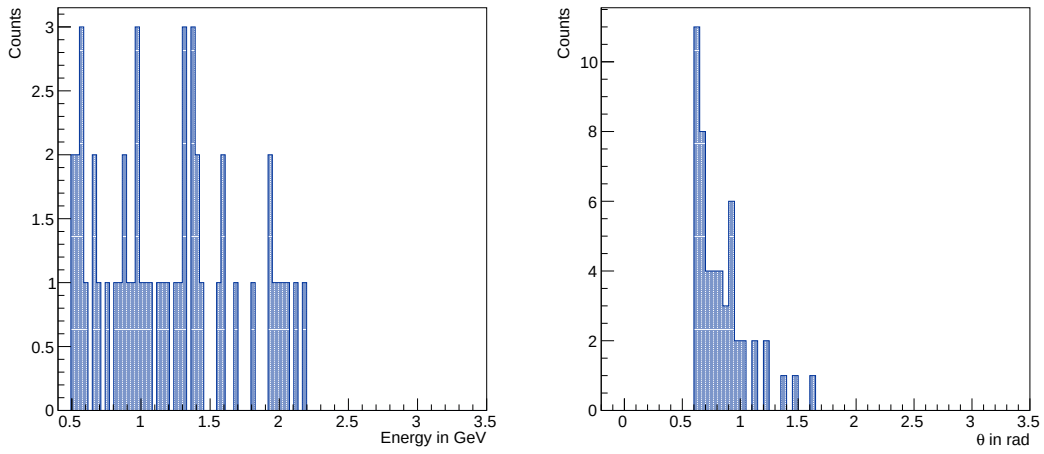

Figure A.18: Secondary hadron energies above 500 MeV and corresponding angles θ for a FLUKA run with $2.5 \cdot 10^{12}$ e.o.t. and applied event selection (3).

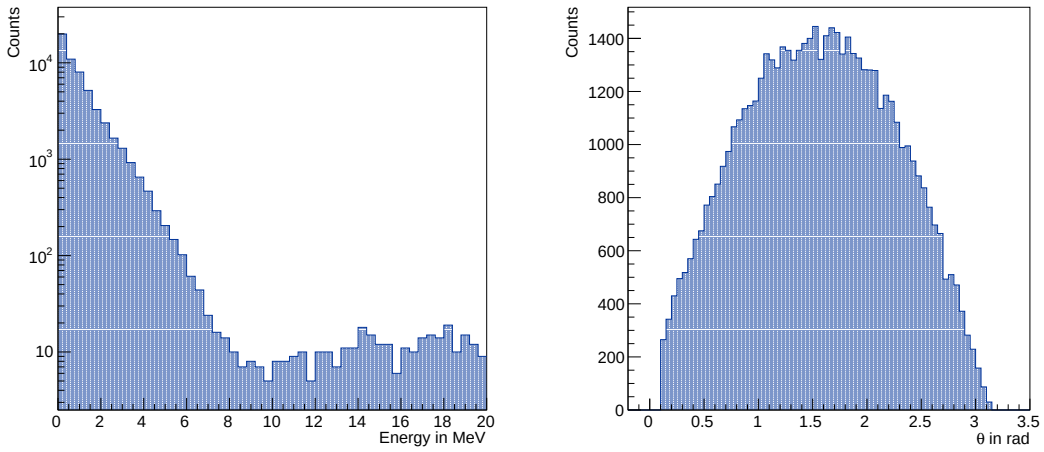

Figure A.19: Secondary photon energies and θ for a FLUKA run with $2.5 \cdot 10^{12}$ e.o.t. and applied event selection (4).

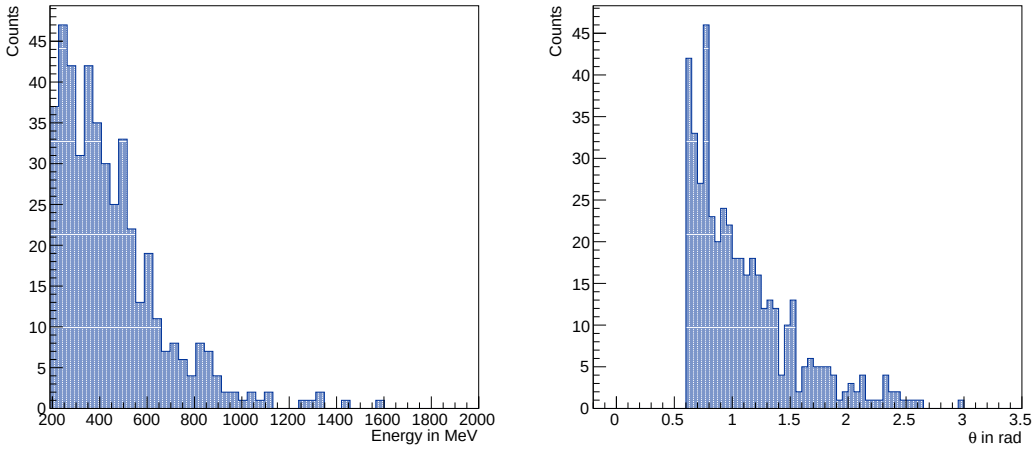

Figure A.20: Secondary photon energies above 200 MeV and corresponding angles θ for a FLUKA run with $2.5 \cdot 10^{12}$ e.o.t. and applied event selection (4).

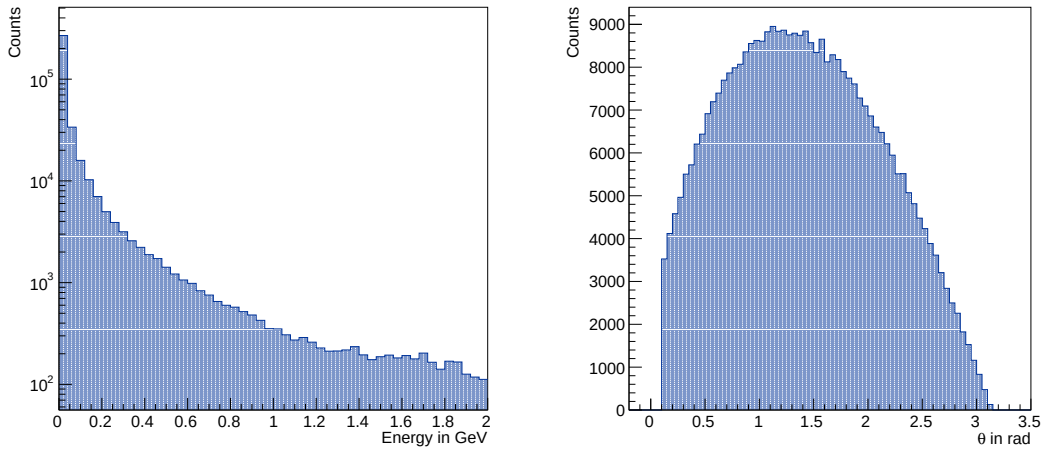

Figure A.21: Secondary hadron energies and θ for a FLUKA run with $2.5 \cdot 10^{12}$ e.o.t. and applied event selection (4).

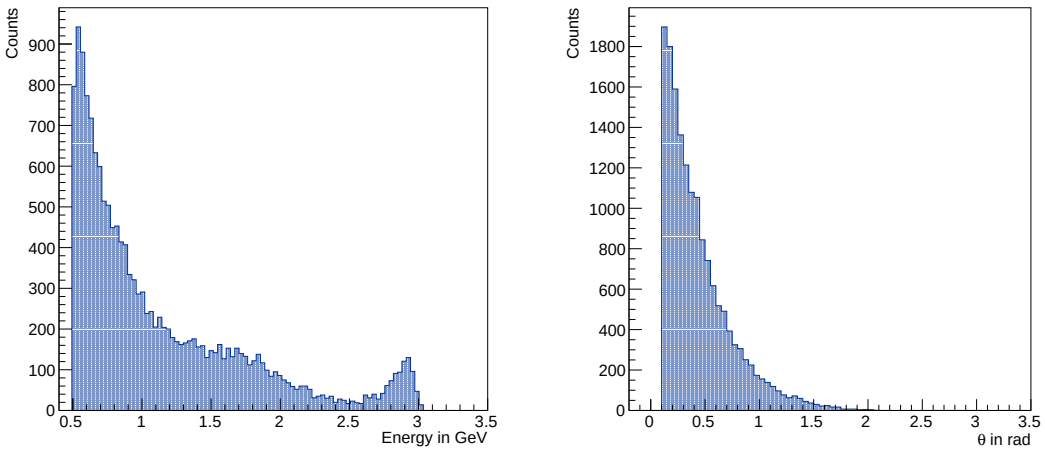

Figure A.22: Secondary hadron energies above 500 MeV and corresponding angles θ for a FLUKA run with $2.5 \cdot 10^{12}$ e.o.t. and applied event selection (4).

A.5 Electro-nuclear FLUKA data in GEANT4 geometry

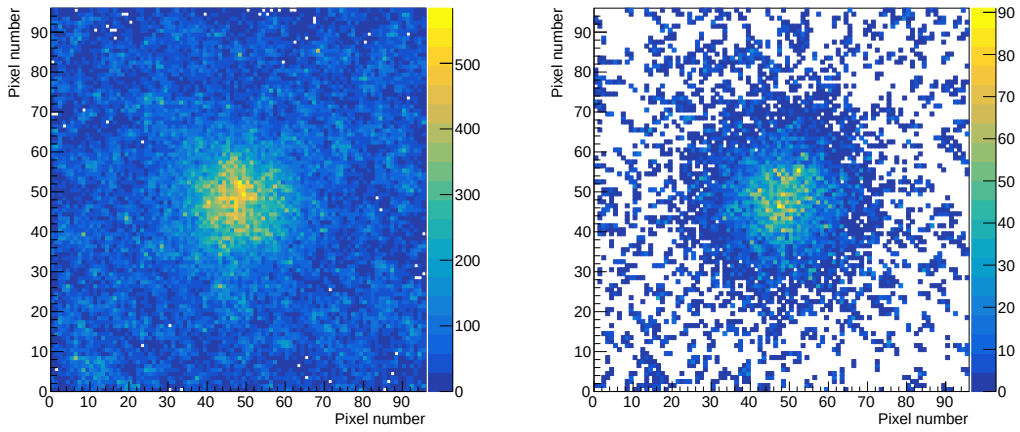

Figure A.23: Hit collections in the pixels of the ECal for all energy deposits (left) and only secondary FLUKA particles (right) without the bulk of the iron magnet.

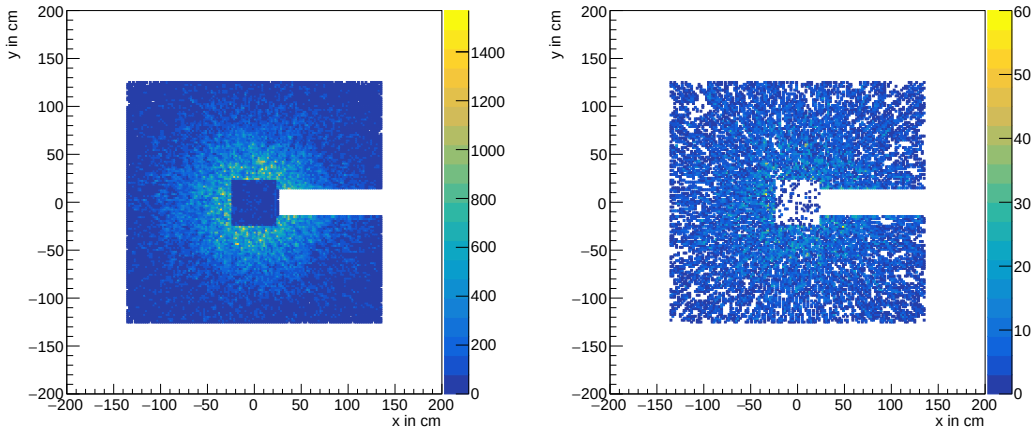

Figure A.24: Energy deposits in the HCal for all particles (left) and only secondary FLUKA particles (right) without the bulk of the iron magnet.

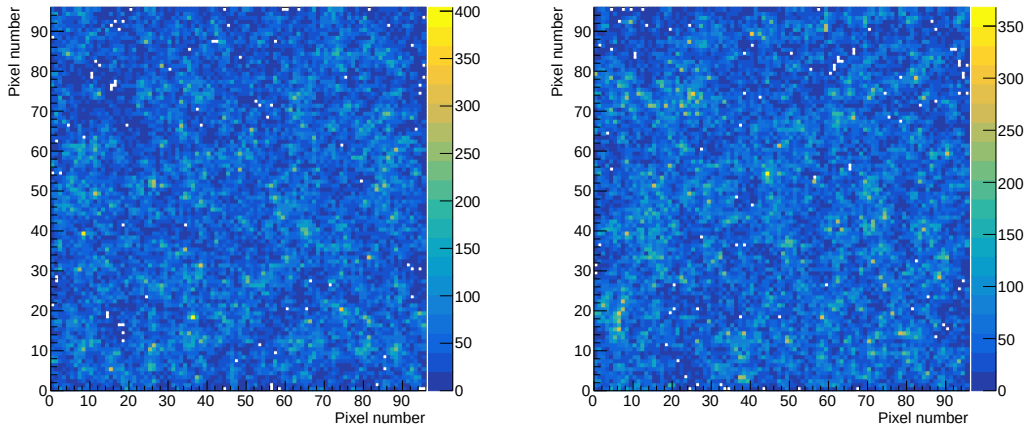

Figure A.25: Hit collections in the pixels of the ECal for all energy deposits with vacuum (left) and air (right) for the 17394 FLUKA events in the GEANT4 geometry.

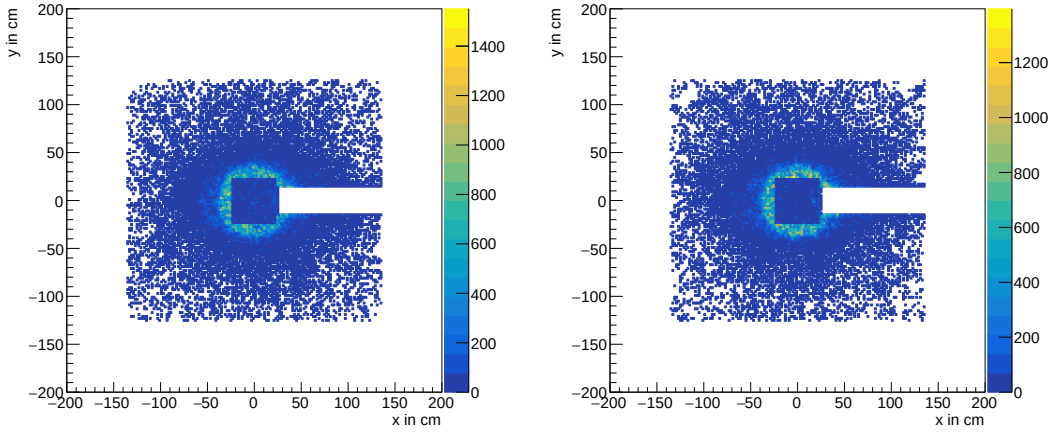

Figure A.26: Energy deposits in the HCal for all particles with vacuum (left) and air (right) for the 17394 FLUKA events in the GEANT4 geometry.

Bibliography

[1] NASA Universe Web Team, *What Can We Learn from the Universe's Baby Picture?*, Accessed: 2025-05-14, 2018, URL: https://science.nasa.gov/universe/what-can-we-learn-from-the-universes-baby-picture/ (cit. on p. 1).

[2] F. Zwicky, *Die Rotverschiebung von extragalaktischen Nebeln*, German, Helvetica Physica Acta **6** (1933) 110, URL: https://www.e-periodica.ch/digbib/view?pid=hpa-001%3A1933%3A6%3A%3A648 (cit. on pp. 1, 6).

[3] M. S. Turner, *Dark energy and the new cosmology*, arXiv preprint astro-ph/0108103 (2001), URL: https://arxiv.org/abs/astro-ph/0108103 (cit. on pp. 1, 6).

[4] J. Wambsganss, *Gravitational Lensing in Astronomy*, Living Reviews in Relativity **1** (1998), ISSN: 1433-8351, URL: http://dx.doi.org/10.12942/lrr-1998-12 (cit. on pp. 1, 6).

[5] P. Bechtle et al., *A Proposal for the Lohengrin Experiment to Search for Dark Sector Particles at the ELSA Accelerator*, 2025, arXiv: 2410.10956 [hep-ex], URL: https://arxiv.org/abs/2410.10956 (cit. on pp. 1, 8, 9, 12–28, 61, 73, 99, 101, 107).

[6] A. Salam and J. C. Ward, *Weak and electromagnetic interactions*, Il Nuovo Cimento (1955-1965) **11** (1959) 568 (cit. on p. 3).

[7] S. L. Glashow, *The renormalizability of vector meson interactions*, Nuclear Physics **10** (1959) 107, ISSN: 0029-5582, URL: https://www.sciencedirect.com/science/article/pii/0029558259901968 (cit. on p. 3).

[8] S. Weinberg, *A model of leptons*, Physical review letters **19** (1967) 1264 (cit. on p. 3).

[9] B. Povh, K. Rith, C. Scholz and F. Zetsche, *Teilchen und Kerne: Eine Einführung in die physikalischen Konzepte*, 2004, ISBN: 978-3-540-21065-8 (cit. on pp. 3, 37).

[10] M. Thomson, *Modern Particle Physics*, eng, 1st ed., New York: Cambridge University Press, 2013, ISBN: 1107034264 (cit. on pp. 3–5).

[11] P. W. Higgs, *Broken Symmetries and the Masses of Gauge Bosons*, Phys. Rev. Lett. **13** (16 1964) 508, URL: https://link.aps.org/doi/10.1103/PhysRevLett.13.508 (cit. on p. 4).

[12] C. Burgard and D. Galbraith, *TeXample: Standard model of physics*, https://texample.net/model-physics/, [Online; accessed 20-January-2025], 2012 (cit. on p. 5).

[13] M. D. Schwartz, *Quantum Field Theory and the Standard Model*, eng, 1st ed., Cambridge: Cambridge University Press, 2013, ISBN: 9781107034730 (cit. on pp. 4, 5).

[14] F. Kuypers, *Klassische Mechanik*, ger, 10. Auflage., Weinheim: John Wiley & Sons, Incorporated, 2016, ISBN: 9783527339600 (cit. on p. 4).

[15] ATLAS Collaboration, *Measurement of the top quark-pair production cross section with ATLAS in pp collisions at* $\sqrt{s}$ = 7 *TeV*, Eur. Phys. J. C **71** (2011) 1577, arXiv: 1012.1792 (cit. on p. 5).

[16] S. Chatrchyan et al., *Observation of a new boson at a mass of 125 GeV with the CMS experiment at the LHC*, Physics Letters B **716** (2012) 30, ISSN: 0370-2693, URL: http://dx.doi.org/10.1016/j.physletb.2012.08.021 (cit. on p. 5).

[17] G. 't Hooft and M. J. G. Veltman, *One loop divergencies in the theory of gravitation*, Ann. Inst. H. Poincare A Phys. Theor. **20** (1974) 69 (cit. on p. 6).

[18] S. Weinberg, "ULTRAVIOLET DIVERGENCES IN QUANTUM THEORIES OF GRAVITATION", *General Relativity: An Einstein Centenary Survey*, 1980 790 (cit. on p. 6).

[19] Y. Fukuda et al., *Evidence for Oscillation of Atmospheric Neutrinos*, Phys. Rev. Lett. **81** (8 1998) 1562, URL: https://link.aps.org/doi/10.1103/PhysRevLett.81.1562 (cit. on p. 6).

[20] S. van den Bergh, *The Early History of Dark Matter*, Publications of the Astronomical Society of the Pacific **111** (1999) 657, ISSN: 1538-3873, URL: http://dx.doi.org/10.1086/316369 (cit. on p. 6).

[21] S. W. Hawking, *Black holes in general relativity*, Communications in Mathematical Physics **25** (1972) 152 (cit. on p. 6).

[22] S. Banerjee et al., *Massive Compact Halo Objects from the relics of the cosmic quark-hadron transition*, Monthly Notices of the Royal Astronomical Society **340** (2003) 284, URL: https://arxiv.org/abs/astro-ph/0211560 (cit. on p. 6).

[23] H. Mo, F. v. d. Bosch and S. White, *Galaxy formation and evolution*, eng, Cambridge [u.a: Cambridge Univ. Press, 2010, ISBN: 9780521857932 (cit. on pp. 6, 7).

[24] D. Clowe, A. Gonzalez and M. Markevitch, *Weak-Lensing Mass Reconstruction of the Interacting Cluster 1E 0657–558: Direct Evidence for the Existence of Dark Matter**, The Astrophysical Journal **604** (2004) 596, URL: https://dx.doi.org/10.1086/381970 (cit. on p. 6).

[25] D. Clowe et al., *A Direct Empirical Proof of the Existence of Dark Matter**, The Astrophysical Journal **648** (2006) L109, URL: https://dx.doi.org/10.1086/508162 (cit. on p. 6).

[26] P. Collaboration et al., *Planck 2015 results. XIII. Cosmological parameters*, Astronomy & Astrophysics **594** (2016) A13, URL: https://arxiv.org/abs/1502.01589 (cit. on p. 6).

[27] Planck Collaboration et al., *Planck 2018 results - V. CMB power spectra and likelihoods*, A&A **641** (2020) A5, URL: https://doi.org/10.1051/0004-6361/201936386 (cit. on p. 6).

[28] G. F. Smoot, "COBE observations and results", *Conference on 3K cosmology*, ASCE, 1999 1, URL: http://dx.doi.org/10.1063/1.59326 (cit. on p. 6).

[29] D. N. Spergel et al., *Wilkinson Microwave Anisotropy Probe (WMAP) Three Year Results: Implications for Cosmology*, Astrophysical Journal Supplement Series **170** (2007) 377, URL: https://arxiv.org/abs/astro-ph/0603449 (cit. on p. 6).

[30] B. W. Lee and S. Weinberg, *Cosmological Lower Bound on Heavy Neutrino Masses*, Phys. Rev. Lett. **39** (1977) 165, ed. by M. A. Srednicki (cit. on pp. 7, 8).

[31] S. Dodelson, *Modern Cosmology*, Academic Press, Elsevier Science, 2003 (cit. on p. 8).

[32] G. Steigman and M. S. Turner, *Cosmological constraints on the properties of weakly interacting massive particles*, Nuclear Physics B **253** (1985) 375, ISSN: 0550-3213, URL: https://www.sciencedirect.com/science/article/pii/0550321385905371 (cit. on p. 8).

[33] J. Angle et al., *First Results from the XENON10 Dark Matter Experiment at the Gran Sasso National Laboratory*, Physical Review Letters **100** (2008), ISSN: 1079-7114, URL: http://dx.doi.org/10.1103/PhysRevLett.100.021303 (cit. on p. 8).

[34] A. Abdukerim, Z. Bo, W. Chen et al., *PandaX-xT—A deep underground multi-ten-tonne liquid xenon observatory*, Science China Physics, Mechanics & Astronomy **68** (2025), URL: https://doi.org/10.1007/s11433-024-2539-y (cit. on p. 8).

[35] C. Collaboration, *Dark sector searches with the CMS experiment*, 2024, arXiv: 2405.13778 [hep-ex], URL: https://arxiv.org/abs/2405.13778 (cit. on p. 8).

[36] D. Hooper and L. Goodenough, *Dark matter annihilation in the Galactic Center as seen by the Fermi Gamma Ray Space Telescope*, Physics Letters B **697** (2011) 412, ISSN: 0370-2693, URL: http://dx.doi.org/10.1016/j.physletb.2011.02.029 (cit. on p. 8).

[37] C. Tönnis, *Search for secluded dark matter with 6 years of IceCube data*, 2021, arXiv: 2107.10778 [astro-ph.HE], URL: https://arxiv.org/abs/2107.10778 (cit. on p. 8).

[38] J. Alexander et al., *Dark Sectors 2016 Workshop: Community Report*, 2016, arXiv: 1608.08632 [hep-ph], URL: https://arxiv.org/abs/1608.08632 (cit. on pp. 8–11).

[39] T. Åkesson et al., *Light Dark Matter eXperiment (LDMX)*, 2018, arXiv: 1808.05219 [hep-ex], URL: https://arxiv.org/abs/1808.05219 (cit. on pp. 9–11, 29).

[40] M. S. Madhavacheril, N. Sehgal and T. R. Slatyer,
Current dark matter annihilation constraints from CMB and low-redshift data,
Phys. Rev. D **89** (10 2014) 103508,
URL: https://link.aps.org/doi/10.1103/PhysRevD.89.103508 (cit. on p. 9).

[41] J. Chen et al., *DarkSHINE Baseline Design Report: Physics Prospects and Detector Technologies*, 2024, arXiv: 2411.09345 [physics.ins-det],
URL: https://arxiv.org/abs/2411.09345 (cit. on p. 9).

[42] M. Cristinziani, *The SHiP experiment at CERN*, 2020,
arXiv: 2009.06003 [physics.ins-det], URL: https://arxiv.org/abs/2009.06003
(cit. on p. 9).

[43] P. Crivelli, *Status and prospects of the NA64 experiment at the CERN SPS*, 2023,
arXiv: 2301.09905 [hep-ex], URL: https://arxiv.org/abs/2301.09905 (cit. on p. 9).

[44] W. Hillert, *The Bonn Electron Stretcher Accelerator ELSA: Past and future*,
The European Physical Journal A - Hadrons and Nuclei **28** (2006) 139,
URL: https://api.semanticscholar.org/CorpusID:122235406 (cit. on p. 13).

[45] ELSA-group, *ELSA/ACCELERATOR: Setup of the Accelerator*,
[Online; accessed 24-January-2025], 2025,
URL: https://www.pi.uni-bonn.de/elsa/en/accelerator/setup (cit. on p. 13).

[46] ELSA-group, *ELSA/ACCELERATOR/FACILITY MAP: Electron Stretcher Accelerator (ELSA)*,
[Online; accessed 24-January-2025], 2025,
URL: https://www.pi.uni-bonn.de/elsa/en/accelerator/facility-map
(cit. on p. 14).

[47] Material Properties, *Tungsten – Protons – Neutrons – Electrons – Electron Configuration*,
Accessed: 2025-05-08, 2021, URL: https://material-properties.org/tungsten-protons-neutrons-electrons-electron-configuration/ (cit. on p. 15).

[48] R. Workman et al., *Review of Particle Physics*, Prog. Theor. Exp. Phys. **2022** (2022) 083C01,
URL: https://pdg.lbl.gov/2022/reviews/rpp2022-rev-passage-particles-matter.pdf (cit. on pp. 15, 82, 83).

[49] Wikipedia contributors, *Spherical coordinate system — Wikipedia, The Free Encyclopedia*,
[Online; accessed 22-January-2025], 2025, URL: https://en.wikipedia.org/w/index.php?title=Spherical_coordinate_system&oldid=1267888900 (cit. on p. 20).

[50] P. P. D. Group, *Atomic and nuclear properties of tungsten (W)*,
https://pdg.lbl.gov/2014/AtomicNuclearProperties/HTML/tungsten_W.html,
[Online; accessed 22-January-2025] (cit. on p. 20).

[51] J.-E. Heinrichs, *PhD thesis to be published in 2025*. 2025 (cit. on p. 24).

[52] E. Fermi, *Über die Theorie des Stoßes zwischen Atomen und elektrisch geladenen Teilchen*,
Zeitschrift für Physik **29** (1924) 315, Cited by: 374,
URL: https://www.scopus.com/inward/record.uri?eid=2-s2.0-33748667694&doi=10.1007%2fBF03184853&partnerID=40&md5=69002d2ba86fe166650f5b53272e8d61
(cit. on p. 24).

[53] I. Pomeranchuk and I. Shumushkevich,
On processes in the interaction of -quanta with unstable particles, Nuclear Physics **23** (1961) 452, ISSN: 0029-5582,
URL: https://www.sciencedirect.com/science/article/pii/0029558261902723
(cit. on p. 25).

[54] M. Hamer, *Private communication*, 2025 (cit. on pp. 28, 31–35, 99, 100, 104, 105).

[55] S. Agostinelli et al., *Geant4—a simulation toolkit*,
Nuclear Instruments and Methods in Physics Research Section A: Accelerators, Spectrometers, Detectors and Associated Equipment **506** (2003) 250 (cit. on pp. 29, 78).

[56] J. Allison et al., *Geant4 developments and applications*,
IEEE Transactions on Nuclear Science **53** (2006) 270 (cit. on pp. 29, 78).

[57] Geant4 collaboration, *Geant4 - Overview*, [Online; accessed 23-January-2025], 2025,
URL: https://www.geant4.org/about/ (cit. on p. 29).

[58] J. Allison et al., *Recent developments in Geant4*,
Nuclear Instruments and Methods in Physics Research Section A: Accelerators, Spectrometers, Detectors and Associated Equipment **835** (2016) 186, ISSN: 0168-9002,
URL: https://www.sciencedirect.com/science/article/pii/S0168900216306957
(cit. on pp. 30, 31).

[59] D. Wright and M. Kelsey, *The Geant4 Bertini Cascade*,
Nuclear Instruments and Methods in Physics Research Section A: Accelerators, Spectrometers, Detectors and Associated Equipment **804** (2015) 175, ISSN: 0168-9002,
URL: https://www.sciencedirect.com/science/article/pii/S0168900215011134
(cit. on pp. 30, 31).

[60] J. P. Wellisch, M. Kossov and P. Degtyarenko, *Electro and gamma nuclear physics in Geant4*, 2003, arXiv: nucl-th/0306012 [nucl-th],
URL: https://arxiv.org/abs/nucl-th/0306012 (cit. on p. 30).

[61] Geant4 Collaboration, *Geant4 User's Guide for Application Developers*,
Version 11.2, Revision 8.0, CERN, 2023, URL: https://geant4.web.cern.ch/documentation/pipelines/master/bfad_html/ForApplicationDevelopers/
(cit. on pp. 31, 38).

[62] Geant4 Collaboration, *G4ElectroNuclearCrossSection Class Reference*, https://apc.u-paris.fr/~franco/g4doxy4.11/html/classG4ElectroNuclearCrossSection.html,
Accessed: 2025-05-06 (cit. on p. 36).

[63] F. Cerutti, *Private communication*, Forum communication, July 2024, 2025
(cit. on pp. 37, 48, 55).

[64] L. S. Klipphahn, *Electro-nuclear simulation in FLUKA model*, https://fluka-forum.web.cern.ch/t/electro-nuclear-simulation-in-fluka-model/6849,
Accessed: 2025-05-07, 2024 (cit. on pp. 37, 55).

[65] S. Navas et al., *Review of particle physics*, Phys. Rev. D **110** (2024) 030001 (cit. on p. 37).

[66] T. T. Böhlen et al.,
The FLUKA Code: Developments and Challenges for High Energy and Medical Applications,
Nuclear Data Sheets **120** (2014) 211 (cit. on p. 48).

[67] A. Ferrari, P. R. Sala, A. Fassò and J. Ranft, *FLUKA: a multi-particle transport code*,
tech. rep. CERN-2005-10, INFN/TC_05/11, SLAC-R-773,
CERN-2005-10, INFN/TC_05/11, SLAC-R-773: CERN, 2005,
URL: https://cds.cern.ch/record/898301 (cit. on p. 48).

[68] A. Fassò, A. Ferrari and P. R. Sala,
Photonuclear Reactions in FLUKA: Cross Sections and Interaction Models,
AIP Conference Proceedings **769** (2005) 1303 (cit. on p. 48).

[69] Cerutti, Francesco et al.,
Nuclear model developments in FLUKA for present and future applications,
EPJ Web Conf. **146** (2017) 12005,
URL: https://doi.org/10.1051/epjconf/201714612005 (cit. on pp. 48, 49).

[70] L. S. Klipphahn, *Electro-nuclear interactions in FLUKA*, https://fluka-forum.web.cern.ch/t/electro-nuclear-interactions-in-fluka/6294,
Accessed: 2025-05-02, 2024 (cit. on pp. 48, 55).

[71] FLUKA collaboration, Beginners FLUKA course, *EM interactions*, Accessed: 2025-05-08, 2015,
URL: https://indico.cern.ch/event/442634/contributions/1096521/attachments/1186022/1719465/13_EM_Interactions_2015.pdf (cit. on pp. 48, 50).

[72] E. Wolynec, V. A. Serrao and M. N. Martins, *Nuclear size effects in virtual photon spectra*,
Journal of Physics G: Nuclear Physics **13** (1987) 515,
URL: https://dx.doi.org/10.1088/0305-4616/13/4/015 (cit. on p. 49).

[73] FLUKA Collaboration, *FLUKA User Manual*, Accessed: 2025-04-24, 2023,
URL: http://www.fluka.org/content/manuals/FM.pdf (cit. on pp. 50, 69).

[74] A. Ferrari et al., *FLUKA: A Multi-Particle Transport Code*, tech. rep.,
SLAC National Accelerator Lab., Menlo Park, CA (United States), 2005,
URL: https://www.osti.gov/biblio/877507 (cit. on p. 51).

[75] Particle Data Group, K. Nakamura et al., *Review of Particle Physics*, J. Phys. G **37** (2010) 075021,
URL: http://pdg.lbl.gov (cit. on pp. 51, 75).

[76] Plansee SE, *Tungsten Sputtering Targets*,
https://www.plansee.com/en/products/tungsten-sputtering-targets.html,
Accessed: 2025-04-25, 2025 (cit. on p. 65).

[77] Thomas Jefferson National Accelerator Facility, *Isotopes of the Element Nickel*,
https://education.jlab.org/itselemental/iso028.html, Accessed: 2025-05-02
(cit. on p. 65).

[78] Wikipedia contributors, *Isotopes of nickel*,
https://en.wikipedia.org/wiki/Isotopes_of_nickel, Accessed: 2025-05-02, n.d.
(Cit. on p. 65).

[79] H. Kolanoski and N. Wermes, *Teilchendetektoren*, 2016, ISBN: 978-3-662-45349-0 (cit. on p. 80).

[80] H. Krieger, "Wechselwirkungen von Neutronenstrahlung",
Grundlagen der Strahlungsphysik und des Strahlenschutzes,
Berlin, Heidelberg: Springer Berlin Heidelberg, 2019 237, ISBN: 978-3-662-60584-4,
URL: https://doi.org/10.1007/978-3-662-60584-4_8 (cit. on p. 82).

[81] P. P. D. Group, *Atomic and nuclear properties of iron (Fe)*,
https://pdg.lbl.gov/2020/AtomicNuclearProperties/HTML/iron_Fe.html,
[Online; accessed 28-April-2025] (cit. on p. 82).

[82] Wikipedia contributors, *Gaussian function — Wikipedia, The Free Encyclopedia*,
[Online; accessed 13-May-2025], 2025, URL: https://en.wikipedia.org/w/index.php?title=Gaussian_function&oldid=1283951381
(cit. on p. 84).

[83] Weeroc, *SKIROC2A User Guide*, Accessed: 2025-05-15, Weeroc, 2016,
URL: https://www.weeroc.com/~documents/products/skiroc-2a/skiroc2-user-guide/?layout=file (cit. on p. 99).

List of Figures

List of Tables

Acknowledgements

First and foremost I want to thank Prof. Dr. Klaus Desch for giving me the opportunity to write my Master thesis in his working group! This past year has again shown me how much fun physics and research is and I thank Klaus, Philip Bechtle and the whole group for the wonderful working atmosphere. Of course I also thank Prof. Dr. Matthias Schott for agreeing to be the second corrector of my thesis.

Many thanks also to Matthias Hamer and Jan Heinrichs for being very patient and helpful mentors in this time. I have thoroughly enjoyed learning from and with you! And of course I also thank Jan and Matthias for proofreading my thesis and their valuable feedback.
I also want to thank my friend Alex, who has accompanied me throughout the physics studies! Thanks for the support and many lunch breaks we spent together updating each other on life - and our projects.

Since intelligence is inherited from the mother ;) I want to thank my mom for providing me with the genes needed to make it this far in my physics journey. All jokes aside, I of course thank also my dad for always believing in me and the rest of my family for the endless support in life! You are the best!
At last I thank my partner in crime Thilo, for being there for me always and making life outside of the office most wonderful and fun!